UNIVERSITÄT ZU LÜBECK

From the Institute of Biomedical Optics
of the University of Lübeck

Director: Prof. Dr. Robert Huber

Advances in femtosecond laser refractive eye surgery: Analysis of mechanisms, and new tools for precise and gentle corneal dissection.

Dissertation
for Fulfillment of Requirements
for the Doctoral Degree
of the University of Lübeck

- from the Department of Natural Sciences

Submitted by

Sebastian Freidank

from Brandenburg an der Havel (Germany)

Lübeck, 2025

First Referee:	Prof. Dr. Alfred Vogel
Second Referee:	Prof. Dr. Christian Hübner
Date of oral examination:	15.12.2025
Approved for printing:	Lübeck, 18.12.2025

Contents

Zusammenfassung

Das Aufkommen zuverlässiger Kurzpulslaser in den 1980er und 1990er Jahren ermöglichte die refraktive Laserchirurgie zur Refraktionskorrektur ohne Brille. Bei der laserunterstützten in-situ-Keratomileusis (LASIK) wurde mit einem Argonfluorid-Excimer-Laser bei einer Wellenlänge von 193 nm das zentrale Hornhautstroma abgetragen, das vorher durch Schneiden eines sogenannten „Flaps“ mit einem mechanischen Mikrokeratom freigelegt worden war. Später wurde das mechanische Keratom durch einen Femtosekundenlaser ersetzt, der durch das Applizieren eines Rasters aus Nahinfrarot-Laserpulsen bei einer Wellenlänge von 1030 nm mit geringer Energie und hoher Wiederholrate eine Hornhautdissektion erzeugen kann. Auf diese Weise können Flaps mit flachem Bett und vertikalem Seitenschnitt erzeugt werden, die eine präzise Repositionierung nach der Operation ermöglichen. Zusätzlich wird es möglich, eine wellenfrontgeführte Ablation zur Korrektur von Aberrationen höherer Ordnung bei Myopie oder Hyperopie durchzuführen. In den 2010er Jahren wurde die Small Incision Lenticule Extraction (SmILE) eingeführt, bei der ein Lentikel mit Femtosekundenlaserpulsen aus dem zentralen Stroma herauspräpariert und durch einen kleinen Seitenschnitt entfernt wird. Diese Technik erfordert nur ein Lasersystem und eine präzise Scanoptik und ist Dank des sehr kleinen Seitenschnittes mit weniger durchtrennten Hornhautnerven und biomechanischer Schwächung der Hornhaut verbunden als die LASIK.

In dieser Arbeit werden die Mechanismen der Hornhautdissektion analysiert und neue Dissektionskonzepte zur Verbesserung der Präzision, Wirksamkeit und Gewebsschonung der refraktiven Chirurgie sowohl bei LASIK als auch bei SmILE vorgestellt. Die Dissektion beruht auf einer Abfolge von laserinduzierter Plasmabildung, Stoßwellenemission und Kavitationsblasendynamik. Die Pulswiederholfrequenz sowie die Energie und der Abstand zwischen den Pulsen beeinflussen die Interaktion zwischen den Ereignissen nachfolgender Laserpulse und damit die Schnittdynamik. Die Grundlagen der Plasmabildung und ihre Abhängigkeit von der Dauer des Laserpulses, der Wellenlänge, dem Fokussierungswinkel und der Fokusform werden in dieser Arbeit mit Hilfe allgemeiner Gleichungen für Photo- und Lawinen-Ionisation, thermische Ionisation und Rekombination beschrieben. Die laserinduzierte Blasenbildung und ihr Zusammenspiel mit der Stoßwellenemission wird mit einem erweiterten Gilmore-Modell der Kavitationsblasendynamik beschrieben. Diese Analyse und frühere Experimente zeigen, dass UVA Sub-Nanosekunden-Laserpulse mit stabiler zeitlicher Form und einer Wellenlänge um 350 nm das Potenzial haben, präzisere Schnitte mit kompakteren Geräten zu erzeugen als herkömmliche Nah-IR-Femtosekunden-Lasersysteme. Darüber hinaus kann die Einführung einer Phasenplatte den Gaußschen Laserstrahl mit länglichem Fokus in einen Vortexstrahl mit einem ringförmigen Fokus ähnlicher Länge umwandeln. Eine solche Fokusformung verspricht eine Verbesserung der Dissektionseffizienz bei Schnitten parallel zur Hornhautoberfläche, was mechanische Nebeneffekte reduzieren und die Präzision erhöhen sollte.

Die Dynamik der Hornhautdissektion durch 330 fs, 1030 nm-Laserpulse wurde mittels stroboskopischer Fotografie mit Submikrometer-Auflösung, Hochgeschwindigkeitsfotografie mit bis zu 50 Mio. Bildern/s und Videografie bei 1 kHz untersucht. Die Größe der Kavitationsblasen wurde von stroboskopischen Aufnahmen durch digitale Bildauswertung bestimmt. Die Morphologie der Schnitte wurde histologisch untersucht und ihre Qualität mittels Rasterelektronenmikroskopie bewertet. Die Hochgeschwindigkeitsfotografie ergab, dass sich das Plasma durch mehrere Hornhautlamellen erstreckt und seine rasche Ausdehnung zu unregelmäßig geformten lobulären Kavitationsblasen führt. Die benachbarten Kavitäten aufeinanderfolgender Laserpulsen treffen wegen der lobulären Blasenform

nicht immer aufeinander, was zu Gewebebrücken führt, die das Ablösen des Flaps bzw. die Lentikelextraktion behindern. Der Schneideprozess kann als Summe einzelner Aufspaltungsereignisse beschrieben werden, die von der Pulsenergie und den Abständen benachbarter Laserfoki abhängen. Er hat jedoch auch eine dynamische Komponente, die der Rissausbreitung beim Bruch von Festkörpern ähnelt. Der Einfluss der dynamischen Komponente hängt von der Pulswiederholrate ab.

Die Verwendung eines Vortex-Strahls wurde sowohl mit IR- als auch mit UV-Wellenlängen untersucht, und es wurde festgestellt, dass er generell die Effizienz und Qualität der Präparation verbessert. Rasterelektronenmikroskopie zeigte, dass mit dem Vortexstrahl erzeugte Schnitte deutlich glatter sind als mit einem Gaußstrahl. Die während der Plasmaexpansion von einem Ringfokus ausgehende Kräfteverteilung im Gewebe erleichtert die Gewebespaltung in Schnittrichtung parallel zur Hornhautoberfläche und minimiert so die Zahl von Gewebebrücken. Daher ist die zur Dissektion erforderliche volumetrische Energiedichte im Fokusvolumen bei einem Vortex-Strahl geringer als bei einem Gauß-Strahl, was den Plasmadruck reduziert und so mechanische Nebenwirkungen verringert. Die geringere Plasmaenergiedichte führt auch zu einer verminderten Gasbildung durch den von freien Elektronen herrührenden Zerfall von Biomolekülen. Dies ist von Vorteil, da langlebige Gasblasen die automatische Identifikation der Pupillenposition bei klinischen Eingriffen beeinträchtigen. Außerdem verringert die blasenbedingte Verzerrung der Hornhautmorphologie die Genauigkeit des oberen Lentikelschnitts bei SmILE. Insgesamt ist die Dissektion mit einem Vortex-Strahl daher präziser und schonender als mit einem Gauß-Strahl.

Experimente mit UV-Femtosekundenpulsen bei 343 nm Wellenlänge und UV-Subnanosekundenpulsen bei 355 nm Wellenlänge zeigten, dass die Präzision der Hornhautschnitte durch eine Verringerung der Laserwellenlänge noch weiter verbessert werden könnte. Dennoch kommt diese Technik für eine klinische Anwendung nicht in Frage, denn obwohl das Schädigungspotenzial der untersuchten UVA-Wellenlängen vier Größenordnungen unter dem Spitzenwert bei 260 nm liegt und obwohl in früheren Tierversuchen keine Hornhautschäden beobachtet wurden, liegt die zum Flap Schneiden erforderliche Strahlenexposition über der maximal zulässigen Dosis.

Die Pulsdauerabhängigkeit der zum Flapschneiden erforderlichen Laserpulsenergie wurde für IR-Pulse mit einer Dauer zwischen 480 fs und 8 ps und für UV-Pulse mit einer Dauer zwischen 1 ps und 400 ps untersucht. Dabei wurde eine starke Abhängigkeit von der Pulsdauer festgestellt – sowohl die applizierte als auch die absorbierte Laserenergie steigt bei längeren Pulsen. Das weist daraufhin, dass sich die Energieeffizienz des Schneideprozesses mit Verlängerung der Pulsdauer vermindert. Für $\tau_L > 10$ ps nehmen der Grad von Druck- und Trägheitseinschluss der Energiedeponierung mit zunehmender Pulsdauer ab, was den Plasmaspitzendruck verringert und die Bildung einer Stoßfront verzögert oder sogar verhindert. Die verringerte Schneidenergie für $\tau_L < 3$ ps rührt von einer Zunahme der Plasmaenergiedichte bei abnehmender Pulsdauer her. Die Ergebnisse dieser Arbeit bestätigen die hohe Eignung von Pulsdauern im unteren Femtosekundenbereich bis hinunter zu etwa 150 fs, die in modernen klinischen Lasersystemen verwendet werden.

Die Verbesserung der Dissektion durch die Verwendung eines Vortexstrahls anstelle eines Gaußstrahls ist das Ergebnis dieser Arbeit mit der größten klinischen Relevanz und dem größten Potenzial für LASIK und SmILE. Es konnte bereits gezeigt werden, dass eine Vortex Phasenplatte einfach in das Strahlführungssystem bestehender klinischer Geräte implementiert werden kann und mit dem Fokus-Scanning kompatibel ist. Der nächste Schritt ist die Durchführung einer klinischen Studie.

Summary

The advent of reliable short-pulsed lasers in the 1980s and 1990s made it possible to perform refractive laser surgery that offers correction without glasses. In laser-assisted in situ keratomileusis (LASIK), argon fluoride excimer laser ablation at 193 nm wavelength was employed to ablate central corneal stroma that had been exposed by cutting a flap using a mechanical microkeratome. Later, the mechanical keratome was replaced by a femtosecond (fs) laser that can produce a corneal dissection through applying a grid of near-IR laser pulses at ≈ 1030 nm with small energy at high repetition rate. This way, flaps with flat bed and side cut can be produced that enable precise repositioning of the flap after surgery. It enables to perform wave front-guided ablation for correction of higher-order aberrations besides myopia or hyperopia. In the 2010s, small incision lenticule extraction (SmILE) was introduced, in which a lenticule is dissected out of the central stroma using only fs laser pulses and removed through a small side cut. This technique requires only one laser and optical delivery system and involves less dissection of corneal nerves and biomechanical weakening of the cornea than LASIK.

The thesis analyses the mechanisms of corneal dissection and explores novel dissection concepts for improving precision, efficacy and gentleness of refractive surgery both in LASIK and SmILE. Dissection relies on a sequence of laser-induced plasma formation, shock wave emission, and cavitation bubble dynamics. Pulse repetition rate, energy and spot separation influence the interaction of events from subsequent laser pulses and, thus, the cutting dynamics. The fundamentals of plasma formation and its dependence on laser pulse duration, wavelength, focusing angle and focus shape are described using generic equations for photo- and avalanche ionization, thermal ionization, and recombination. Laser-induced bubble formation and its interplay with shock wave emission is described using an extended Gilmore model of cavitation bubble dynamics. This analysis and previous experiments show that UVA sub-nanosecond laser pulses with stable temporal shape and a wavelength around 350 nm offer the potential of creating more precise cuts with more compact devices than conventional near-IR fs laser systems. Furthermore, the introduction of a helical phase plate can transform the Gaussian laser beam with elongated focus into a vortex beam with a ring shaped focus of similar length. Such focus shaping promises to improve the dissection efficacy in direction parallel to the corneal surface, which should reduce mechanical side effects and increase precision.

The dynamics of corneal dissection by 330 fs, 1030 nm laser pulses was investigated using stroboscopic photography with sub-micrometer spatial resolution, high-speed photography with up to 50 million frames/s and videography at 1 kHz. The cavitation bubble size was determined from stroboscopic photographs through digital image evaluation. The morphology of the cuts was investigated histologically, and the quality of the cuts evaluated through scanning electron microscopy. It turned out that the plasma extends through several corneal lamellae and its rapid expansion leads to irregularly shaped lobular cavitation bubbles. Lobes from neighboring bubbles do not always meet, which leads to tissue bridges hindering flap lifting and lenticule extraction. The cutting process is largely an addition of individual disruption/cleavage effects, which depend mainly on pulse energy and spot separation. However, it has also a dynamic component resembling crack propagation during fracture in solids, which implicates a dependence on pulse repetition rate.

The use of a vortex beam was explored for IR and UV wavelengths and found to improve dissection efficiency and quality. Scanning electron microscopy showed that the cuts are smoother than with a Gaussian beam. The force distribution during the plasma expansion from a ring focus facilitates tissue cleavage in the cutting direction parallel to the corneal surface and minimizes tissue bridges. Therefore, the volumetric energy density in the focal volume required for dissection is smaller with a vortex beam than with a Gaussian beam, which reduces plasma pressure and mechanical side effects. The smaller plasma energy density results also in less gas generation through free-electron-mediated molecular disintegration. This is advantageous because long-lived gas bubbles impair pupil tracking during clinical procedures and distort the corneal morphology during dissection of the upper lenticule cut in SmILE. Altogether, dissection using a vortex beam is more precise and gentler than with a Gaussian beam.

Experiments with fs pulses at 343 nm wavelength and sub-ns pulses at 355 nm showed that the precision of corneal dissection could be further improved by reducing the laser wavelength. However, although the damage potential of the investigated UVA wavelengths lies four orders of magnitude below the peak value around 260 nm and although no corneal damage has been observed in previous animal experiments, the radiant exposure required for flap cutting lies above the permissible dose.

The pulse duration dependence of laser pulse energy required for dissection with easy flap lifting was investigated for IR pulses between 480 fs and 8 ps duration and UV pulses between 1 ps and 400 ps duration. A strong pulse duration dependence is found even for the absorbed laser energy needed for flap cutting, which indicates that the efficiency of the cutting process drops. For durations $\tau_L > 10$ ps, stress and inertial confinement of energy deposition decrease, which reduces the plasma peak pressure and delays or even inhibits the formation of a shock front. For $\tau_L < 3$ ps, the reduced cutting energy is related to an increase of plasma energy density with decreasing pulse duration. These findings confirm the high suitability of pulse durations in the lower fs range down to about 150 fs, which are used in state-of the art clinical laser systems.

The improvement of dissection through use of a vortex beam instead of a Gaussian beam is the finding of this thesis with greatest clinical relevance and potential for LASIK and SmILE. It has already been demonstrated that a helical phase plate can be easily implemented into the beam delivery system of existing clinical devices and is compatible with focus scanning. The next step is the conduction of a clinical study.

1. Introduction

Refractive errors, especially myopia, are an increasing problem in modern societies, where outdoor activities are ever more replaced by indoor activities, reading, cell phone use, and computer work. Refractive errors can be corrected by glasses but a correction without glasses is often preferred for cosmetic and functional reasons (a strongly myopic person wearing glasses cannot even orientate when the glasses are not on, or lost). The advent of reliable short-pulsed lasers in the 1980s and 1990s made it possible to perform refractive laser surgery that offers correction without glasses.

Initially, argon fluoride (ArF) excimer laser ablation was employed to ablate central corneal stroma that had been exposed by cutting a flap using a mechanical microkeratome. This procedure is called Laser-assisted in situ keratomileusis (LASIK) [1, 2] and relies on the small ablation depth of nanosecond (ns) UV laser pulses at 193 nm wavelength [3]. Later, the mechanical keratome was replaced by a femtosecond laser that can produce a corneal dissection through applying a grid of laser pulses with small energy at high repetition rate [4]. Although expensive, this laser knife has the advantage that flaps with flat bed and vertical or oblique side cut can be produced that enable precise repositioning of the flap after surgery. This makes wave front-guided ablation possible, where higher-order aberrations are corrected besides the basic myopia or hyperopia [5]. At this stage, refractive laser surgery required two lasers (excimer and fs laser) combined with advanced optical delivery systems, which makes it very costly. Therefore, a new technique was introduced in which a lenticule is dissected out of the central stroma using only fs laser pulses and then removed through a small side cut [6]. Small incision lenticule extraction (SmILE) requires only one laser and optical delivery system and involves less dissection of corneal nerves and biomechanical weakening of the cornea than LASIK. Therefore, it is becoming ever more popular.

Although millions of people have already been treated with the above techniques, many open questions remain and there is still potential for improving precision, efficacy and gentleness of refractive surgery. This requires a profound understanding of the mechanisms of dissection and of the origin of side effects and the exploration of novel concepts going beyond established dissection techniques. These concepts aim at improving both LASIK and SmILE.

Laser dissection in transparent tissue relies on energy deposition by nonlinear absorption through plasma formation (optical breakdown) at the laser focus [3, 7-9]. The laser-induced plasma features a high volumetric energy density going along with high pressure in the range of hundreds of MPa and a high temperature of several thousand Kelvin [10]. Thus, plasma expansion results in shock wave emission and the formation of a cavitation bubble that locally disrupts the corneal tissue. The fundamentals of refractive laser surgery and the theoretical foundations of plasma formation and laser-induced cavitation and the parameter dependence of laser-induced effects are described in ***section 2***.

The choice of application parameters such as laser pulse duration, wavelength, beam quality, pulse energy, pulse repetition rate, focusing angle and spot separation relies on technical possibilities but their optimization requires a mechanistic understanding of the dissection process. A deeper understanding is still lacking because of the high speed and small extent of the microsurgical processes. In ***section 3***, these processes are investigated by stroboscopic

photography of IR fs laser cutting with sub-micrometer spatial resolution and by ultra-high-speed photography with up to 50 million frames/s [11]. Long image sequences of the dissection process are taken by high-speed videography at 1 kHz. The energy dependence of the size of laser-induced intrastromal cavitation bubbles is determined by stroboscopic photography with digital image evaluation, and the morphology of the cuts is investigated histologically.

The elongated shape of the laser plasma oriented perpendicular to the desired cutting direction is disadvantageous. Results from section 3 reveal that the plasma extends through several corneal lamellae, and its rapid expansion leads to irregularly shaped lobular cavitation bubbles. When lobes from neighboring bubbles do not meet, tissue bridges remain that impair flap lifting and lenticule extraction. Dissection can be improved by focus shaping with a helical phase plate transforming a Gaussian into a vortex beam [12, 13]. Vortex beams are also propagation invariant but feature a ring focus with larger diameter than and same length as a Gaussian beam. This facilitates tissue cleavage in cutting direction. ***Section 4*** describes experiments on corneal dissection with a vortex beam in comparison with the performance of a Gaussian beam. Electron microscopic analysis of the flap beds demonstrate that dissection using a vortex beam produces smoother cuts. Transmission measurements during dissection are used to assess the volumetric energy density in the focal volume. If they are smaller with a vortex beam than with a Gaussian beam that will go along with reduced mechanical side effects.

Refractive laser surgery is usually performed with near-infrared (IR) wavelengths because commercial fs lasers emit at wavelengths around 1040 nm and visible wavelengths would dazzle the patient. We discovered previously that single-longitudinal-mode (slm) sub-ns laser pulses at 355 nm wavelength can produce nanoeffects as fine and adjustable in size as fs laser effects [14, 15]. UV-A laser pulses at 355 nm promise a much higher cutting precision than achievable with IR wavelengths, are not visible to the patient, and have a strongly reduced photodamage potential compared to the peak around 260 nm. Moreover, laser systems delivering slm UV-A pulses are more compact and less costly than fs laser systems. Therefore, corneal dissection with UV-A laser pulses is investigated for Gaussian and vortex laser beams. The experiments and their results are described and discussed in ***section 5***.

Section 5 also addresses the influence of laser pulse duration on cutting energy, which is relevant for potential side effects. The pulse duration dependence is explored for UV and near-IR wavelengths, using various laser systems. A strong pulse duration dependence of absorbed laser energy required for easy flap lifting is observed for both wavelength regimes. This observation is remarkable because it implicates that less mechanical work is required for dissection, when shorter pulses are used. Potential reasons for this trend will be discussed based on the theoretical foundations laid in section 2.

Section 6 presents safety considerations for refractive surgery with UV-A laser pulses. Even though the photodamage potential of the investigated UV-A wavelengths lies four orders of magnitude below the peak value [16], the pulse energies required for flap cutting must lie below the maximum permissible exposure value [17]. We will see that this is a critical hurdle for the new approach. Hence, the improvement of dissection through use of a vortex beam instead of a Gaussian beam is the finding of this thesis with greatest clinical relevance. In ***section 7***, the next steps required for a clinical implementation of the vortex beam approach are discussed together with perspectives for its realization.

2. Fundamentals

2.1. Refractive media of the eye

Cornea and lens are the refractive media of the eye, as shown in Fig. 2.1. The refractive power of the cornea (39 dpt) is larger than that of the lens (20 dpt) because of the large refractive index jump between air and cornea. The refractive power of the lens is relatively small in spite of its strongly curved shape since its refractive index is only slightly larger than that of the surrounding aqueous and vitreous humor.

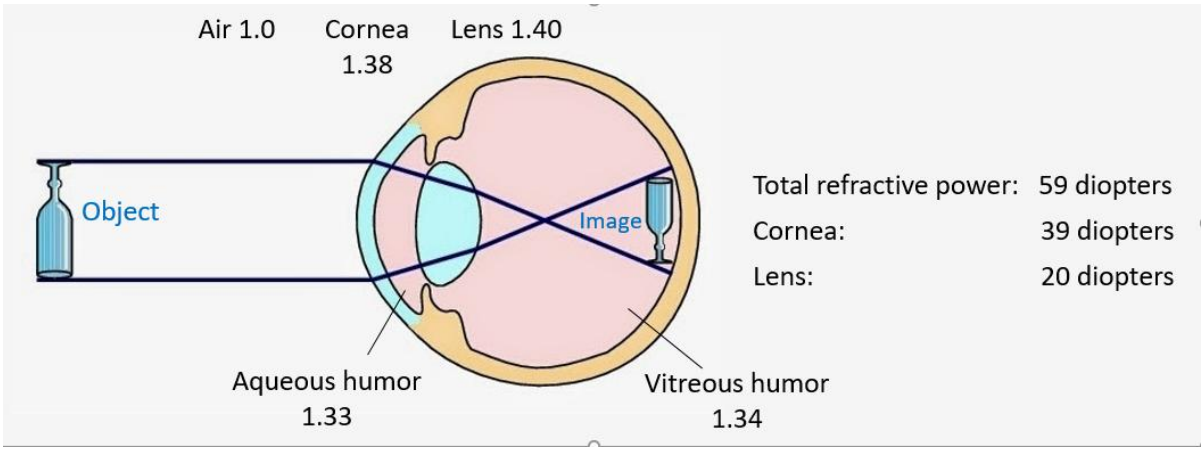

Fig. 2.1 Schematic of the eye with refractive indices of the transparent ocular media, their refractive powers, and a sketch of image formation. Drawing from: http://rodsncones.blogspot.com/2014/05/physiology-image-formation.html, data from https://www.mediworks.biz/en/news/41.

Since the refractive index jump at the air-cornea interface is largest, this interface is well suited to alter the refractive power by changing the curvature of the corneal surface through refractive laser surgery. For correction of myopia, the curvature of the corneal must be flattened in order to reduce the refractive power and shift the image to the retina [18]. This is equivalent to wearing glasses with concave lenses. By contrast, for correction of hyperopia, the curvature in the central region must be steepened, which can be achieved by material removal in a ring around the center within the optical zone defined by the pupil of the eye [19].

In this context, one must consider the layered structure of the cornea (Fig. 2.2) and the different metabolic and regeneration properties of the individual layers [20]. The epithelium covering the outer surface of the cornea heals and reconstitutes its generic shape after injuries. The stroma is mechanically stable and retains its shape after mechanical or laser-mediated reshaping, if no thermal injuries are involved in the reshaping process [21, 22]. Therefore, refractive surgery cannot be performed on the corneal epithelium but must address the corneal stroma. Material removal can be achieved by laser ablation of superficial stromal tissue, or by dissection and extraction of a lenticule from the inner stroma, as described in section 2.2.

Descement's membrane is the basement membrane of the endothelium, and the endothelium controls the metabolism and hydration of the corneal stroma. Appropriate water content is essential for the transparency of the cornea. It requires continuous removal of water from the stroma by active pumping by the endothelial cells, which are connected by tight junctions to seal the interface between aqueous humor and stroma. Injury of the endothelium results in corneal haze if cells do not manage to cover and reseal the injury [22, 23].

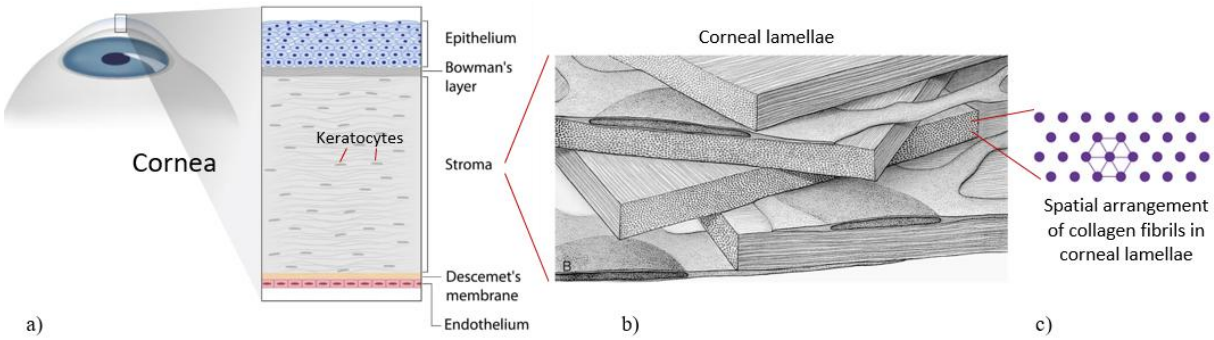

Fig. 2.2 Schematic. ***(a)*** From anterior to posterior, the five layers that compose the cornea are epithelium, Bowman's layer, stroma, Descemet's membrane, and endothelium. The anterior surface of the cornea is covered by the tear film, and the posterior surface borders the aqueous-filled anterior chamber. Source: [20]. ***(b)*** Enlarged view of the *corneal stroma.* It is composed of orderly, dense, fibrous connective tissue containing collagen fibrils within an aqueous ground substance, which form many 2-3 µm thick *lamellae*. Collagen fibrils within a lamella are parallel to one another and run the full length of cornea. Successive lamellae run across cornea at an angle to one another. Some fibroblast cells (keratocytes) are seen between the lamellae. *Keratocytes* are thin and flat with long processes that contact fibroblast processes of other cells lying in same plane. They are responsible for producing new collagen in regular metabolism and after injuries. ***(c)*** *Regular spatial arrangement of corneal collagen fibrils*. Each of the fibrils is separated from the others by an equal distance. Benedek has explained the transparency of cornea on the basis of this equidistant separation, which leads to a homogeneous distribution of average refractive index on the spatial scale of the wavelength of visible light [23]. Mucoproteins, glycoproteins, and other components of ground substance are responsible for maintaining proper position of fibrils. Distortion of the regular order during collagen production after injuries leads to corneal haze. Thermal damage in pulsed laser ablation is one type of injury that results in haze.

2.2. Laser refractive eye surgery

Laser-assisted in situ keratomileusis (LASIK) is a well-established surgical technique to correct refractive errors like hyperopia, myopia or astigmatism in the human eye, with more than 18 million operations worldwide performed to date [24-27]. Keratomileusis was introduced in the 1990s by the pioneering work of Peyman, Pallikaris, and Burrato [1, 2, 28, 29]. In LASIK, the curvature of the central part of the cornea is reduced by precise excimer laser ablation to correct for myopia (shortsightedness), as shown in Fig. 2.3(a). The thinning of the central cornea needed for myopic correction is 9 µm per diopter in the center for an optical zone with 5 mm diameter, and progressively less towards the periphery of the zone [18]. Larger optical zones increase the thickness of ablated material but do not reduce the requirements on shape accuracy and surface quality within the optical zone. The necessary precision is in LASIK provided by Argon-Fluoride (ArF) excimer laser ablation at 193 nm wavelength, where the optical penetration depth is ≈ 0.3 µm, and the thermal damage zone is only ≈100 nm thin [30]. Damage of the remaining tissue is avoided partly by the short duration of the ArF laser pulses (20 ns) that prevents thermal diffusion out of the layer into which the laser energy is deposited, and partly by a mixture of photochemical and thermal ablation mechanisms. Photochemical disintegration of collagen fibrils by the UV photons is combined with vaporization of tissue water, which drives the ejection of the fibrillar fragments [3]. The combination enables smooth and gentle ablation.

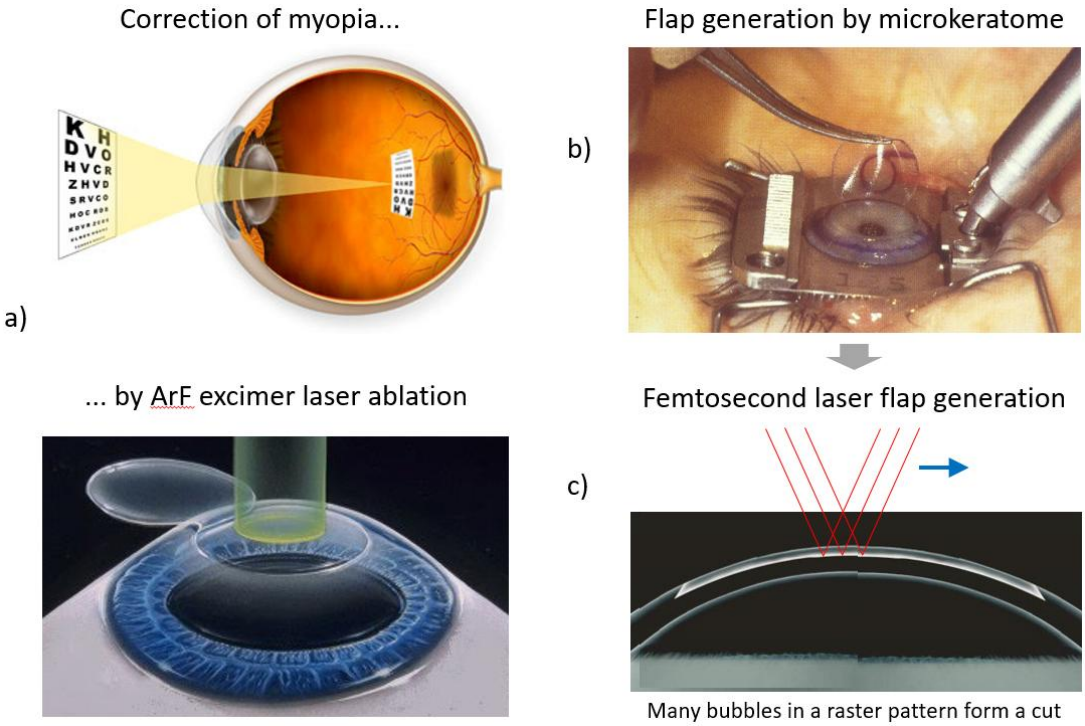

Fig. 2.3 LASIK with flap cutting by microkeratome and fs laser. (a) Basic principle of myopia correction by ArF excimer laser ablation. b) Flap dissection with a microkeratome, c) Femtosecond laser flap dissection. Source: N. Linz & A. Vogel, Lecture "Plasmavermittelte Chirurgie am Beispiel refraktiver Hornhautchirurgie", Kurs MIW Master, Biomedizinische Optik, Univ. Lübeck.

Ablation must occur in the central collagenous layer of the cornea, the corneal stroma, because the outer layer, the epithelium, would re-grow within a few days and close the laser injury such that the refractive distortion recurs. For intrastromal ablation, an incision is made in the upper corneal layer to create a tissue flap with a hinge on one side to keep the flap connected to the cornea. Initially, flap dissection was performed using a microkeratome (Fig. 2.3b). In the late 1990s, Juhasz and Lubatschowski introduced ultrashort laser pulses for intrastromal flap dissection instead of a microkeratome [4, 31] (Fig. 2.3c).

Femtosecond laser corneal refractive surgery

Femtosecond (fs) laser refractive corneal surgery of shortsightedness (myopia) and far-sightedness (hyperopia) has been introduced in the late 1990s [4, 31]. In fs laser in-situ keratomileusis (LASIK), fs laser pulses are tightly focused in a raster pattern into the corneal stroma at numerical apertures between 0.2 and 0.5 to create a corneal dissection. This way, a circular flap with ≥ 5 mm diameter is created by producing a cut parallel to the corneal surface in about 100 µm depth followed by a side cut from the flap bed to the surface. Similar to the procedure with a microkeratome, a hinge is left one side. The flap is lifted, and the refractive correction is then performed by reshaping the intrastromal surface via excimer laser ablation. After surgery, the flap is repositioned, and covered for some time by a therapeutic contact lens until it adheres again to the stromal bed.

When the flap is cut with a microkeratome, it can laterally move after folding back and epithelial cells can invade the gap between flap and stromal bed, which is a source of complications [32]. The laser procedure with side cuts avoids such complications and facilitates

precise relocation into the original position. This is a prerequisite for wavefront-guided excimer laser ablation where the shape of the wavefront after passage of cornea and lens is determined before surgery and the cornea is then reshaped to correct higher-order aberrations together with the basic myopic or hyperopic [5]. Moreover, the cut for the flap bed should be performed at a certain depth because injuries of Bowmans layer (the uppermost stromal layer next to the epithelium) may result in corneal haze [33].

The need for flap cutting at a certain depth together with the thinning of the corneal stroma by the excimer laser ablation for refractive correction imply a weakening of the mechanical stability of the cornea [24]. In 2010, small incision lenticule extraction (SmILE) was introduced into the clinic in which two intrastromal incisions produce a lenticule that is removed through a 2- 4 mm long incision on one side [6, 34] (Fig. 2.4). The concept of lenticule dissection in conjunction with its removal after flap opening had been introduced earlier by Juhasz et al. and Lubatschowski et al. [4, 31] – the novelty of the SmILE concept was lenticule removal through a small incision. The lenticule is ≈ 20 µm high at its rim to provide the necessary thickness and mechanical stability of the lenticule that enables to remove it easily with forceps. SmILE compromises the corneal stability less than LASIK because it avoids the 100 µm high circular flap side cut required in LASIK. This reduces the "dry eye" syndrome frequently observed after LASIK, which originates from a dissection of corneal nerves that interrupts the feedback circle controlling the tear flow [35]. Corneal nerves run horizontally from the nasal towards the temporal side of the cornea. The nerves are interrupted by the circular flap side cut but not by the small incision for lenticule removal that is usually located at the upper side of the excised

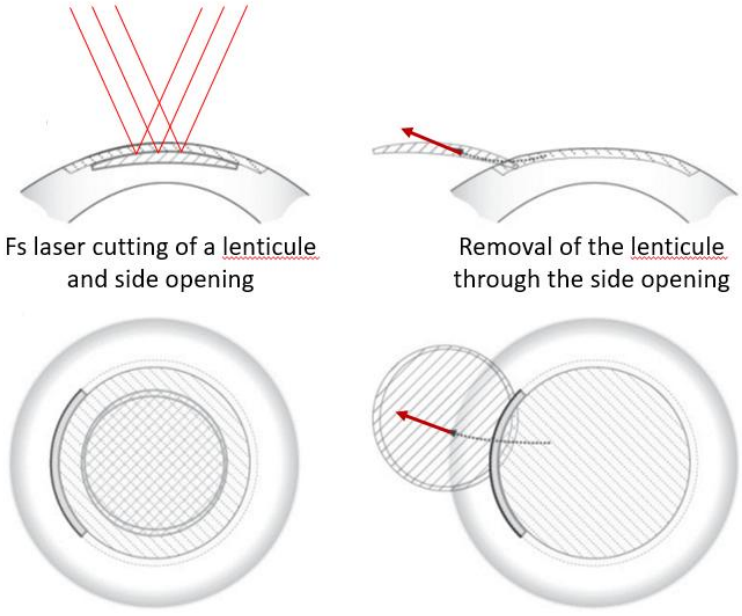

Fig. 2.4 Basic principle of the small incision lenticule extraction (SmILE) procedure. Source [36].

lenticule where it does not cross nerve fibers. SmILE can be performed completely with the femtosecond laser system, whereas in LASIK two complex systems are needed. This reduces treatment time and costs.

Both LASIK and SmILE work best for correction of myopia, which involves a flattening of the corneal curvature. Hyperopic corrections require a steepening of the central cornea, In LASIK or SmILE, this is achieved by creating a ring-like indentation around the center via excimer laser ablation or through an appropriate shape of the extracted lenticule. However, epithelial regrowth tends to fill the indentation, which compromises the stability of the refractive correction [37]. Therefore, filler techniques are now under investigation in which a biocompatible filler material is injected into a laser-generated corneal pocket to steepen the curvature of the central cornea [38-40].

In all commercially available refractive laser systems, ultrashort infrared (IR) laser pulses are employed for dissection [41]. IR wavelengths do not dazzle the patient and cause minimum heating of the retina because melanin absorption in the retinal pigment epithelium decreases strongly with increasing wavelength (it drops from ≈ 50% at 500 nm to less than 3% above 1000 nm [3, 42]). Model simulations predicted a peak retinal temperature rise of ≤ 0.6 K for all investigated clinical laser systems [43].

Femtosecond laser assisted cataract surgery

In recent years, the spectrum of refractive laser surgeries has been expanded by femtosecond laser assisted cataract surgery (FLACS) [44-46]. State of the art cataract surgery involves creating a small incision in the cornea, a circular tear (capsulorhexis) in the anterior lens capsule, and emulsification of the turbid lens. Then an artificial intraocular lens (IOL) is implanted into the remaining capsular bag. The first three steps can be performed by FLACS laser systems. Lasers can perform step-like corneal incisions, which facilitate sealing of the cut by intraocular pressure after surgery and IOL implantation. This sutureless technique reduces the risk of postoperative astigmatism. Moreover, lasers can perform a precise and well-centered incision of the anterior lens capsule, which is otherwise one of the most difficult tasks in cataract surgery. Well-centered capsulotomies with predictable diameter are a prerequisite for the implantation of toric IOLs for astigmatic correction and multifocal IOLs that enable to focus at near and far distances (with a trade-off of reduced contrast visibility) [47]. Finally, the shock waves and cavitation bubbles arising from laser-induced plasma formation can also be employed for lens fragmentation. Since plasma-mediated lens fragmentation does not work well in strongly scattering lenses, FLACS has promoted a trend towards early cataract surgery on clear lenses, often in conjunction with the implantation of multifocal intraocular lenses for presbyopia correction.

The above laser-surgical procedures require guidance by optical coherence tomography (OCT) or another 3-D imaging technique and the capability of the delivery optics to provide good focus quality at different depths [44]. Overall, the design of FLACS systems is more challenging than the design of LASIK or SmILE systems and relies on the experience gathered in these areas. However, laser tissue interactions are similar as in corneal surgery.

In this thesis, I shall focus attention on corneal refractive surgery because it is still the most wide spread refractive laser surgical procedure and involves high challenges on precision that can be optimally met by using advanced laser micro- and nanostructuring techniques, which will be presented in chapters 3-5.

Modes of corneal dissection

Two modes of corneal dissection are used in clinical practice. In the most commonly used "cleavage mode", laser pulses are applied in a raster pattern with several micrometer spot separation. To achieve a homogeneous cut, the laser pulse energy must be large enough to produce disruptive effects (shock waves and cavitation bubbles) that can cleave the corneal lamella between the individual laser spots. In the cleavage mode, scanning usually covers the entire surgical field and the NA is moderate. The maximum possible pulse repetition frequency (PRF) is determined by the possible scan speed in conjunction with the desired spot separation. In present clinical systems, the spot separation is 2-6 µm, and the PRF 150-500 kHz [41].

One manufacturer uses an alternative approach in which laser pulses of lower energy are applied at large NA and a much higher PRF in the MHz range such that the individual laser spots overlap [41]. Therefore, each location in the dissection plane is hit by several laser pulses. Here, cutting does not rely on the disruptive action of laser-induced plasma expansion but rather on free-electron-mediated disintegration of biomolecules in the collagen fibers, as described in [9]. High-rep-rate, low-energy dissection has been extensively covered in two recent review papers [48, 49], and I will focus further attention on the cleavage mode.

Challenges for precision and predictability

The thinning of the cornea needed for myopic correction is 9 µm per diopter in the center for an optical zone with 5 mm diameter, and progressively less towards the periphery of the zone [18]. Larger optical zones increase the thickness of ablated material but do not reduce the requirements on shape accuracy and surface quality within the optical zone. The necessary precision is in LASIK provided by Argon-Fluoride (ArF) excimer laser ablation at a wavelength of 193 nm, where the optical penetration depth is ≈ 0.3 µm, and the thermal damage zone is only ≈100 nm thin [30].

Precise and smooth femtosecond laser dissection requires a minimization of the spatial extent of individual laser effects. The numerical aperture (NA) of the focusing beam must be as large as possible to minimize the focus length. Optics design for achieving this goal is challenging because the field of view must have ≈ 10 mm diameter. Therefore, NAs in clinical instruments are usually fairly small, between 0.2 and 0.35. A value of NA ≈ 0.5 can only be achieved when the optics is moved during treatment and the field of view is covered by stitching tiles [48].

SmILE imposes particular challenges on cutting precision since the predictability of refractive correction relies completely on the precision of lenticule cutting. This precision is compromised by long plasmas generated at small NAs and by high pulse energies producing large cavitation bubbles (see section 2.2). Large bubbles created during cutting of the lower lenticule face distort the overlying corneal stroma and compromise the cutting precision of the upper face.

Altogether, optimum surgical and refractive outcome relies on precise, gentle and – if possible – bubble free corneal dissection. Novel strategies for improved flap and lenticule cutting rely on a profound understanding of the mechanisms underlying laser dissection.

Theoretical foundations for such understanding are laid in section 2.2 on laser-induced plasma formation and section 2.3 on the resulting cavitation bubble dynamics, and novel dissection approaches are introduced in section 2.4.

2.3. Optical breakdown

The first step in corneal laser dissection is plasma formation in the corneal stroma ('optical breakdown'), followed by shock wave emission and bubble formation. Corneal stroma is an aqueous medium interspersed with biomolecules. In the following theoretical description of plasma formation, the role of biomolecules is neglected and the focus is laid on the description of plasma formation in water at different laser pulse durations τ_L, wavelengths λ_L and pulse energies E_L. Water is treated as homogeneous large-bandgap medium. The mechanisms underlying nonlinear energy deposition in the (τ_L, λ_L, E_L) parameter space are very complex – even for focusing at large *NA*, where nonlinear beam propagation plays little role. Therefore, the overview of the expected breakdown behavior is based on generic equations and heuristic arguments that provide a framework for the interpretation of the measurement results in sections 3 to 5 A similar approach has been taken in Ref. [15].

Pathways of nonlinear energy deposition and thermalization

The general sequence of nonlinear energy deposition in large-bandgap dielectrics at high irradiance is depicted in Fig. 2.5. Plasma formation is initiated by strong-field ionization (SI) via multiphoton ionization (MPI) or tunneling across the band gap between valence band (VB) and conduction band (CB). Seed electron generation is followed by avalanche ionization (AI) that consists of a sequence of inverse bremsstrahlung absorption (IBA) events of single laser photons through which the kinetic energy of the CB electrons is raised until it suffices to free another VB electron by impact ionization. Conservation of energy and momentum during IBA requires that the photon interacts with the electron during a collision with a heavy particle (atom or ion). Moreover, it requires a kinetic energy of the impacting electron ≥ (3/2) $\tilde{\Delta}$ [7, 50, 51], where $\tilde{\Delta}$ is the ionization potential of the dielectric. This potential is given by the sum of band gap energy E_{gap} and the oscillation (quiver) energy E_{osc} of CB electrons in the strong electromagnetic field [7, 52]. Avalanche ionization initiated by strong-field ionization is the backbone of nonlinear energy deposition into large band gap materials such as water [7, 51, 53, 54].

The energy deposited into the electronic system is thermalized via collisional electron-phonon coupling and electron-hole recombination. The resulting volumetric energy density U is given by the time-integrated product of CB electron density, ρ_c, and the average energy ε_{avg} carried by CB electrons, where ε_{avg} is the sum of $\tilde{\Delta}$ and the average kinetic energy of the electrons, $\varepsilon_{kin.avg}$. For fs breakdown, only one set of free electrons is produced during the laser pulse, and their energy is thermalized afterwards [7-9]. Here, U is simply the product ($\rho_c \times \varepsilon_{avg}$) but for ns breakdown, it can be much larger. When a sufficiently high thermodynamic temperature, T_{equil}, of the breakdown region is reached, VB electrons can be lifted into the CB via thermal ionization. For sufficiently long pulse durations, recombination and thermal ionization create feedback loops through which the CB-electron density, ρ_c, and T_{equil} act back on the energy deposition process. The feedback strength is given by the dependence of

avalanche-ionization and recombination rates on free electron density, and by the temperature dependence of thermal ionization. In the following, we will see how the different time constants of primary energy deposition processes and feedback loops result in different features of the breakdown dynamics depending on laser pulse duration and wavelength.

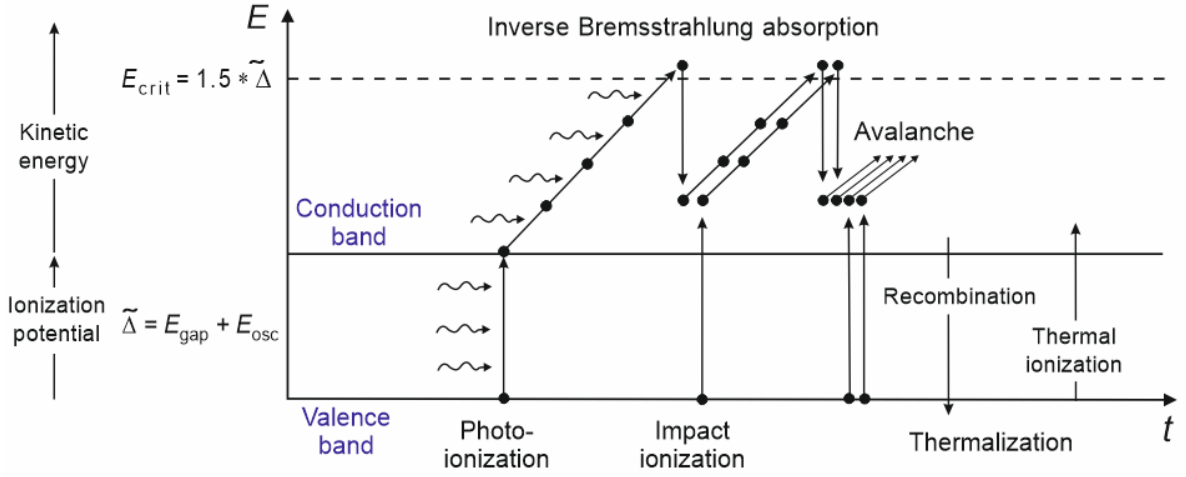

Fig. 2.5 Pathways of nonlinear energy deposition and thermalization during optical breakdown in large-bandgap dielectrics. (a) Visualization of the pathways within the band structure of the dielectric, (b) Visualization with feedback loops between the individual mechanisms. The energy flow from the laser light into the electronic system of the dielectric is followed by thermalization and the hydrodynamic response of the medium. These pathways include feedback loops through which the free-electron density ρ_c and temperature T_{equil} produced by nonlinear absorption act back on energy deposition and ionization. When the thermodynamics temperature of the medium is sufficiently high, nonlinear absorption is complemented by thermal ionization. Recombination, thermalization, and thermal ionization play no role during fs breakdown but become increasingly important for longer pulse durations.

Strong-field ionization provides seed electrons quasi-instantaneously. Seed electron generation by MPI dominates from UV to near-IR and at low irradiance values, whereas tunneling becomes relevant at longer wavelengths [9, 54-58]. The irradiance dependence of strong-field ionization becomes complicated, when tunneling gets involved but when multiphoton ionization dominates, it is simply proportional to I^k, where k is the order of the multiphoton process [52, 59].

For bubble formation at $\tau_L \geq 100$ fs, most electrons are produced by *avalanche ionization* [7, 51]. This process is subject to time constraints because impact ionization can occur only after conduction band (CB) electrons have gained sufficient energy through inverse brems-strahlung absorption. Free electrons can absorb photons only during collisions with heavy particles, which occur in intervals of ≈ 1 fs [7, 8, 58, 59]. Since several subsequent absorption processes are needed to collect sufficient energy for impact ionization, the feedback of free-electron density on the avalanche ionization rate has a time-lag [56, 59]. Nevertheless, it occurs on fs time scale, and this feedback loop thus plays a significant role already in fs breakdown. The energy distribution of CB electrons is initially nonstationary and its evolution during this time has to be described by a multi-rate equation [51, 56, 60]. However, for sufficiently long pulse durations the energy distribution evolves asymptotically into a stationary distribution, whereby the transition time depends on bandgap, wavelength, and irradiance. For water, it

amounts to ≈ 100 fs [7, 60]. Once the stationary regime has been reached, avalanche ionization is proportional to the CB electron density and approximately proportional to I [7, 59, 61].

The time scale for *recombination* is longer than the time constant relevant for avalanche ionization. In water, recombination proceeds mainly as non-radiative interaction of CB electrons with $H_3O^+_{aq}$ ions and as electron attachment to neutral OH fragments [7, 62, 63]. At irradiance values leading to optical breakdown, cross recombination processes between electrons and holes from independent ionization events dominate [64]. Under these circumstances, recombination is proportional to the square of free-carrier density because two types of free-carriers are involved in each event [59, 65]. The recombination time ranges from < 1ps to several ps, depending on ρ_c [7]. Therefore, recombination will influence the breakdown dynamics only in ps and ns breakdown.

Thermalization of the absorbed laser energy involves energy transfer from free electrons to heavy particles occurring through elastic and inelastic collisions [66, 67] as well as through recombination followed by energy dissipation via vibrational relaxation [68-70]. Thermalization through inelastic collisions with vibrational excitation of water molecules occurs on a time scale below 1 ps and dominates for low-density plasmas such as the electron cascade produced by ionizing radiation [71-74]. Plasma life times < 1ps were reported for fs plasmas with low electron densities of 3 x 10^{18} cm^{-3} [75], which is two orders below the bubble threshold [7]. Here, CB electrons interact with intact water molecules and are then solvated in traps below the CB [76]. By contrast, in high-density plasmas well above the breakdown threshold, water molecules are largely dissociated and the band structure is disturbed [77, 78]. In this regime, electron collisions are mainly elastic, and longer thermalization times, τ_{therm}, in the order of 20-30 ps have been observed [79, 80]. Here, thermalization proceeds mainly via electron-hole combination, and the recombination rate was determined by analyzing the decay of plasma scattering [79, 80] and luminescence [65].

Heating of the focal volume during the laser pulse causes a gradual change of the electronic energy distribution from Fermi-Dirac statistics towards a Boltzmann distribution [81, 82]. The change of the energy distribution can significantly contribute to the CB electron density, when high temperatures are reached and the high-energy tail of the Boltzmann distribution reaches into the CB. We denote this temperature-related process as "*thermal ionization*." Since it refers to the electron density distribution in thermal equilibrium between electron and heavy particle populations, it differs significantly from strong-field and avalanche ionization, which create a thermal imbalance by depositing energy into the electronic system. As long as the band structure is still intact, the temperature-related density of electrons in the conduction band, ρ_{therm}, can be assessed using the theory of electric conductivity of semiconductors [81, 82]. When the band structure is dissolved at high temperatures, the ionization degree is described by the Saha equation [83, 84]. Both approaches predict a proportionality $\rho_{therm} \propto exp(-E_{gap}/2k_BT)$, where E_{gap} is the band gap energy, and k_B the Boltzmann constant [81-84]. The exponential increase of ρ_{therm} with T suggests a rapid onset of thermal ionization beyond a critical temperature T_{cr}, which will become relevant at times $t > \tau_{therm}$.

Electron and heat diffusion out of the focal volume as well as a reduction of ρ_c by hydrodynamic plasma expansion become important only for pulses of several ns or longer [9, 85], and will be neglected in the following.

The above considerations reveal that essentially four interaction mechanisms with different dependencies on I, ρ_c and T acting on different time scales govern the evolution of CB electron density. These are strong-field ionization, avalanche ionization, recombination, and thermal ionization. A simplified overview of their characteristic features is given by the following set of generic equations:

$$\left(\frac{d\rho_c}{dt}\right)_{MPI} = \eta_{MPI}\, I^k , \tag{2.1}$$

$$\left(\frac{d\rho_c}{dt}\right)_{AI} = \eta_{AI}\, \rho_c\, I , \tag{2.2}$$

$$\left(\frac{d\rho_c}{dt}\right)_{rec} = -\eta_{rec} \times \rho_c^2 , \tag{2.3}$$

$$\rho_{c,therm} \propto e^{-E_{gap}/2k_BT} . \tag{2.4}$$

For the sake of simplicity, we consider in Eq. (2.1) only MPI as representative for strong-field ionization. The relative strength of MPI and AI depends on the laser wavelength. While the MPI rate decreases with increasing λ due to the larger number of photons required for crossing the bandgap, the AI rate increases due to the larger cross section for inverse bremsstrahlung absorption [7, 59, 86]. The relative strength of recombination and thermal ionization compared to MPI and AI depends on the laser pulse duration. Recombination comes into play for pulse durations longer than the thermalization time of CB electrons, and thermal ionization plays a role when recombination and collisional dissipation have lasted long enough to heat the focus to temperatures ≥ 3000 K [87]. It can be seen from Fig 1 that recombination and thermal ionization counteract each other – while recombination inhibits the ionization process for long laser pulses, it is enhanced by thermal ionization. A consideration of their interplay reveals interesting features that have been overlooked in the past.

We assume a simple band gap without energy levels between valence and conduction band. The actual band structure is more complex in water, where an intermediate state at the energy level of solvated electrons facilitates plasma initiation [7, 53, 60]. Furthermore, we assume a constant band gap during plasma formation although the band structure deteriorates once high electron densities and temperatures are reached in the focal volume, and the rate constants for all ionization processes change. While consideration of details is required to explore the shades of optical breakdown dynamics, the simple form of Eqs. (2.1) – (2.4) helps in obtaining a qualitative understanding of the great picture arising from the complex interplay between the mechanisms governing nonlinear energy deposition. This way, it enables to characterize and anticipate general scenarios for the irradiance and energy dependence of the breakdown behavior in the (τ_L, λ_L) parameter space. Two scenarios are well known from previous research in other groups, and a third one was discovered during experimental investigations at the Institute of Biomedical Optics [14, 15].

Breakdown scenarios from precisely tunable energy deposition to "big bang"

Scenario 1: Continuous tunability such as observed in fs breakdown. At ultrashort pulse durations, the breakdown dynamics is governed solely by strong-field and avalanche ionization. Recombination and thermalization can be neglected since they occur on a ps time scale after the laser pulse. Strong-field-created seed electrons are abundant but the value of ρ_c at the end of the laser pulse depends mainly on the avalanche ionization rate, as discussed in the previous section. Since the avalanche ionization rate is limited by time constraints, ρ_c increases gradually with growing irradiance [Eq. (2.2)]. Therefore, the onset of breakdown is smooth, and the amount of deposited energy – and the bubble size - can be continuously tuned by varying E_L.

Scenario 2: "Big bang" such as observed in IR ns breakdown. With increasing laser pulse duration ever more doubling sequences of the ionization avalanche can occur during a pulse. Therefore, the irradiance threshold for bubble formation could largely decrease for long pulses if seed electrons for avalanche ionization were readily available. However, seed electron generation by multiphoton ionization requires a minimum irradiance. This hurdle is particularly large for long wavelengths, where high-order multiphoton processes are required for crossing the bandgap. Thus, for IR ns pulses seed electron generation is the critical hurdle for the occurrence of breakdown. Once this hurdle is overcome, the ionization avalanche proceeds very fast. In conjunction with thermal ionization, it can largely overshoot the threshold condition and produce bright plasma luminescence and a large bubble already at the onset of breakdown. In this "big bang" scenario, tunability of energy deposition is restricted to the high-density plasma regime.

Scenario 3: Stepwise tunability in ps and ns breakdown. At short wavelengths, multiphoton ionization always provides sufficient seed electrons for AI, even at nanosecond pulse durations. However, although the ionization avalanche has an easy start, it is considerably slower than in IR breakdown because the avalanche ionization rate is smaller for shorter wavelengths as it is approximately proportional to λ^2 [7]. The slow ionization avalanche will thus be inhibited by recombination because the recombination rate is proportional to ρ_c^2 [Eq. (2.3)], while the avalanche ionization rate exhibits a linear dependence on ρ_c [Eq. (2.2)]. In the lower irradiance range near threshold, the growth of the free electron density is limited and a dynamic equilibrium between avalanche ionization and recombination evolves in which laser energy is continuously deposited into the electronic system and thermalized simultaneously. The focal temperature reached at the end of the laser pulse depends on the equilibrium level of ρ_c, which is determined by the focal irradiance. The above description implies that ns pulses at UV wavelengths and possibly also at short visible (VIS) wavelengths fulfill essential prerequisites for precisely tunable energy deposition and the creation of nano- and micro effects – a feature, which traditionally has been ascribed to ultrashort laser pulses and scenario 1.

With increasing irradiance (or E_L), the ionization avalanche produces an ever higher free electron density before it is inhibited by recombination. Thus, the focal temperature reached at the end of the pulse increases gradually as long as recombination can hold the ionization process. Beyond a critical temperature, the breakdown dynamics will change dramatically due to the exponential dependence of thermal ionization on temperature [Eq. (2.4)]. Together with avalanche ionization, thermal ionization now overcomes the inhibiting action of recombination, and ρ_c can suddenly shoot up to very high levels. Consequently, brightly luminescent plasma

with high energy density is formed. The existence of a second breakdown threshold at the upper end of the nano/micro regime is a key difference to scenario 1 with continuous tunability. Thus, scenario 3 is an intermediate between the other better-known scenarios, sharing features of scenario 1 at low irradiance and of scenario 2 at high irradiance. The abrupt transition between the tunable low- and high-density plasma regimes must go along with a sudden, stepwise increase of the vaporized liquid volume, plasma pressure and bubble size.

The existence of the three scenarios for optical breakdown in water has been demonstrated experimentally by recording the maximum bubble radius as a function of laser pulse energy for different pulse durations, wavelengths, and mode of laser operation (mode-locked operation for fs pulses, multi-longitudinal mode and single-longitudinal mode operation for ns pulses) [15]. The results are shown in Fig. 2.6.

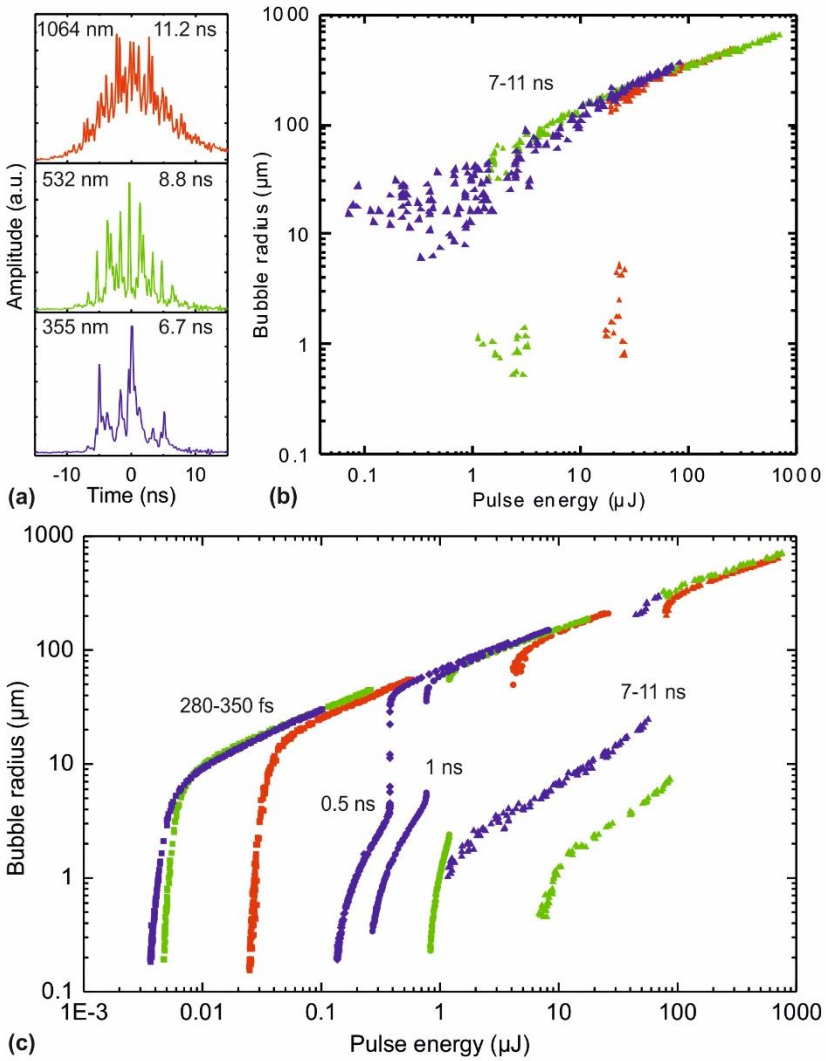

Fig. 2.6 Maximum cavitation bubble radius as a function of laser pulse energy for different pulse durations, wavelengths, and laser modes; *NA* = 0.8. The colors denote the wavelengths: blue = 347 nm for fs pulses, and 355 nm for ns pulses; green = 520 nm and 532 nm, respectively, red = 1040 nm and 1064 nm. Examples for pulse shapes of longitudinally multimode laser pulses of 7-11 ns duration are given in (a), and the $R_{max}(E_L)$ data for these irradiation conditions are presented in (b). All ns data in (c) were obtained using longitudinally single mode (Gaussian) laser pulses. The fs data refer to mode-locked pulses.

The $R_{max}(E_L)$ dependencies in Fig. 2.6 reflect the three scenarios described above. In fs breakdown, R_{max} increases continuously with E_L from 200 nm to large bubble sizes, initially with steep and later with smaller slope (scenario 1). By contrast, IR ns pulses generate luminescent plasmas and large bubbles with 50 to 200 µm radius already at threshold (scenario 2). In the third scenario, applicable to UV and VIS ns pulses with smooth temporal shape corresponding to single-longitudinal-mode laser operation, the $R_{max}(E_L)$ curves feature an abrupt increase in bubble size that correlates with the onset of bright plasma luminescence. The terms "small-bubble regime" and "BPL regime" are used to distinguish the regions before and after the step. At the bubble threshold, nano-bubbles with a radius as small as 200 nm can be produced, just like in fs breakdown.

Deterministic vs. stochastic breakdown behavior

A remarkable feature of ns breakdown in Fig. 2.2 is the dramatic difference in the breakdown behavior for multi- and single-longitudinal mode operation. This become comprehensible by first looking at fs breakdown. For ultrashort laser pulses, where seed electrons are abundant, breakdown dynamics and bubble threshold show little dependence on impurities as long as pulse duration and energy remain stable. In these regions, the breakdown dynamics is, therefore, “inherently” deterministic. By contrast, when MPI initiation is the critical hurdle for the occurrence of breakdown, the breakdown dynamics depends more sensitively on small variations of the initial conditions. Here, a deterministic behavior can be expected only for highly reproducible laser pulses with smooth temporal profile and good beam quality, and for largely impurity-free media. While the temporal profile of mode-locked laser pulses is fairly stable, many solid state ns lasers are run in longitudinal multimode operation in which the pulse shape exhibits intensity spikes arising from statistical interference of the longitudinal modes that affect the multiphoton excitation rate [Eq. (2.1)]. Pulse-to-pulse fluctuations of the spiking behavior with intensity peaks of varying height at different times during the pulse introduce strong fluctuations in seed electron generation that result in a stochastic breakdown behavior.

Impurities can also influence the seed electron generation - either by localized heating of tiny particles followed by thermionic electron emission or by providing intermediate energy levels in the water band gap that facilitate multiphoton excitation. Contaminations of low concentration in a nominally ‘pure’ medium differ from biomolecules in aqueous biological media that provide numerous centers of reduced excitation energy at high concentration [88-90]. Both thermionic emission of seed electrons and/or reduced excitation energy for MPI at impurities in biological tissues can lower I_{th} in IR ps and ns breakdown [91, 92]. By contrast, in UV breakdown, seed electrons are readily available, and significant changes of I_{th} can here only arise when the impurity concentration is so high that it significantly widens the MPI-channel [7], or when the seed electrons become available at fluctuating times during a laser pulse exhibiting spikes.

The probability of hitting upon particulate impurities is much larger for small *NA*s because the focal volume V increases rapidly with decreasing *NA*: $V \propto 1/NA^4$. For sufficiently large *NA*, plasmas are compact and smaller than the average distance between impurities [93]. Therefore, impurities will hardly matter, and deterministic behavior is possible not just for ultrashort laser pulses but also for ns breakdown by laser pulses with smooth temporal shape.

Consequences for corneal dissection

The results for 0.5 ns and 1 ns pulse duration were obtained with compact diode-pumped master-oscillator-amplifier (MOPA) laser systems. Hence, the tunable energy deposition and creation of nanoeffects in the low-energy part of scenario 3 opens interesting perspectives for the use of compact diode-pumped solid state lasers in applications for which to date bulkier and more expensive fs lasers are employed. The possibility to perform corneal dissection at 355 nm with such a laser system is explored in section 5 of the thesis.

2.4. Laser-induced bubble formation

Corneal laser dissection involves vaporization of the tissue within the plasma volume and disruptive tissue cleavage by the shock wave and the cavitation bubble produced during the explosive plasma expansion. A model for laser-induced bubble formation must consider the compressibility of the medium surrounding the plasma to be able to cover both shock wave emission and bubble oscillations. The Gilmore model of cavitation bubble dynamics [94] fulfills this requirement and will be presented below, together with several extensions introduced by Vogel et al (1996), Liang et al (2022), and Liang and Vogel (2025) [10, 95, 96]. The extensions consider the finite duration of the laser pulse producing the bubble and the contribution of the initial particle velocity behind the shock front to the bubble wall velocity. The extended Gilmore model is presented following these papers.

The model considers the compressibility of the liquid surrounding the bubble, viscosity and surface tension. Sound radiation into the liquid from the oscillating bubble is incorporated based on the Kirkwood-Bethe hypothesis [97]. The Gilmore model assumes a constant gas content of the bubble, neglecting evaporation, condensation, gas diffusion through the bubble wall, and heat conduction. For strong oscillations, i.e. strong compression of the contents inside the bubble, the model is augmented by a van der Waals hard-core law to account for a non-compressible volume of the inert gas inside the collapsing bubble [94, 98].

Equations governing the bubble dynamics

To formulate model equations for the bubble oscillator, various parameters of the liquid surrounding the bubble and of the gas and vapor contents inside the bubble need to be specified. For a spherical bubble, the bubble variables describing its size and shape can be condensed to just one, the bubble radius, R, whose variation with time, t, has to be determined, $R(t)$. The model parameters are given in Fig. 2.7. Besides R, these are the equilibrium radius of the bubble at rest, R_n, the external hydrostatic pressure in the liquid, p_∞, and the pressure inside the bubble, p_i, further the polytropic exponent of the gas in the bubble, κ and ρ, μ and σ, the density, the (dynamic) viscosity and the surface tension of the liquid, respectively. The initial bubble pressure is encoded in the ratio R_n/R_0.

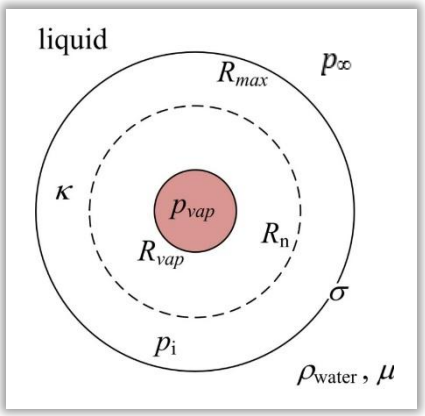

Fig. 2.7 Definition of bubble parameters.

The bubble dynamics is described by the equation

$$\left(1-\frac{U}{C}\right)R\dot{U}+\frac{3}{2}\left(1-\frac{U}{3C}\right)U^2=\left(1+\frac{U}{C}\right)H+\frac{U}{C}\left(1-\frac{U}{C}\right)R\frac{\mathrm{d}H}{\mathrm{d}R}. \tag{2.5}$$

Here, $U=\mathrm{d}R/\mathrm{d}t$ is the bubble wall velocity, an overdot means differentiation with respect to time, C is the speed of sound in the liquid at the bubble wall, and H is the enthalpy difference between the liquid at pressure $p(R)$ at the bubble wall and at hydrostatic pressure

$$H=\int_{p|_{r\to\infty}}^{p|_{r=R}}\frac{\mathrm{d}p(\rho)}{\rho}, \tag{2.6}$$

whereby r is the distance from the bubble centre. The driving force for the bubble motion is the difference between the pressure within the liquid at the bubble wall and at a large distance from the wall (static pressure). Assuming an ideal gas inside the bubble, the pressure P at the bubble wall is given by

$$P=p\Big|_{r=R}=\left(p_\infty+\frac{2\sigma}{R_\mathrm{n}}\right)\left(\frac{R_\mathrm{n}^3-R_\mathrm{vdW}^3}{R^3-R_\mathrm{vdW}^3}\right)^\kappa-\frac{2\sigma}{R}-\frac{4\mu}{R}U, \tag{2.7}$$

where σ denotes the surface tension, μ the dynamic shear viscosity, and κ the ratio of the specific heat at constant pressure and volume (polytropic coefficient) (Fig. 2.3). At the equilibrium radius R_n, the bubble pressure just balances the hydrostatic pressure. The term $R_\mathrm{vdW}^3=(b\,R_\mathrm{n})^3$ describes the size of the van der Waals hard core, with van der Waals coefficient b. The pressure is assumed to be uniform throughout the volume of the bubble. The pressure far away from the bubble is $p\big|_{r\to\infty}=p_\infty$. The equation of state (EOS) of water is approximated by the Tait equation, with B = 314 MPa, and n = 7

$$\frac{p+B}{p_\infty+B}=\left(\frac{\rho}{\rho_\infty}\right)^n, \tag{2.8}$$

which leads to the following relationships for the sound velocity C and enthalpy H at the bubble wall

$$C=\sqrt{c_\infty^2+(n-1)H}, \tag{2.9}$$

$$H = \frac{n(p_\infty + B)}{(n-1)\rho_\infty}\left[\left(\frac{P+B}{p_\infty + B}\right)^{(n-1)/n} - 1\right], \tag{2.10}$$

with c_∞ and ρ_∞ denoting the sound velocity and mass density in the liquid at normal conditions. The term dH/dR in Eq. (3.1) can be derived from Eqs. (2.7) and (2.10) by calculating (dH/dP)×(dP/dR). It reads

$$\frac{\mathrm{d}H}{\mathrm{d}R} = \frac{1}{\rho_0}\left(\frac{p_\infty + B}{P+B}\right)^{\frac{1}{n}} \times \left(-3\kappa R^2\left(p_\infty + \frac{2\sigma}{R_\mathrm{n}}\right)\frac{\left(R_\mathrm{n}{}^3 - R_\mathrm{vdW}^3\right)^\kappa}{\left(R^3 - R_\mathrm{vdW}^3\right)^{\kappa+1}} + \frac{2\sigma}{R^2} + \frac{4\mu U}{R^2}\right). \tag{2.11}$$

Description of laser-induced bubble initiation

Direct modeling of the temporal evolution and spatial distribution of the energy deposition during optical breakdown (section 2.2) is complicated, and the details depend strongly on the laser pulse duration. Therefore, the details of the breakdown process are neglected and only the plasma size at the end of the laser pulse the maximum radius reached by the cavitation bubble as a consequence of plasma expansion are considered. The extent of the plasma marks the volume into which laser energy is deposited, and the size of the expanded cavitation bubble is an indicator for the conversion efficiency of light energy into mechanical energy.

Calculations start with a bubble nucleus with radius R_0, whereby the volume of this nucleus is identified with the photographically determined plasma size in the liquid. At $t = 0$, the nucleus contains liquid water which is then heated by the laser pulse, expands, and forms a bubble when temperature and pressure have dropped below the critical point. For the sake of convenience, one usually denotes the outer border of this nucleus also already as "bubble wall." The energy input during the laser pulse is simulated by raising the value of the equilibrium radius R_n from its small initial value $R_\mathrm{n} = R_0$ at the beginning of the pulse to a much larger final value R_nbd. The underlying assumption is that the absorbed laser energy is proportional to the amount of liquid vaporized by the laser pulse, which in turn is proportional to the equilibrium volume of the laser-induced bubble given by $4/3\ \pi\ R_\mathrm{nbd}{}^3$. This assumption holds when the energy deposited into the plasma is significantly larger than the sum of the energy needed for heating the vaporized liquid volume to the boiling temperature plus the latent heat of vaporization.

The equilibrium radius R_n is a measure of the total gas content of the cavitation bubble and does not distinguish between vapour and non-condensable gas. An increase of the R_n value beyond R_0 implies that the pressure inside the bubble rises and that the bubble starts to expand. The R_nbd value for which the calculation yields the same oscillation time T_osc1 or maximum radius R_max1 as found experimentally is determined iteratively.

While energy deposition by ultrashort laser pulses can be regarded as quasi-instantaneous, the finite duration of the laser pulse must be considered for nanosecond breakdown. The temporal evolution of the laser power P_L during the pulse is modelled by a $\sin^2$ function with duration τ_L (full-width at half-maximum) and total duration $2\tau_\mathrm{L}$

$$P_\mathrm{L} = P_{\mathrm{L}0}\sin^2\left(\frac{\pi}{2\tau_\mathrm{L}}t\right), \qquad 0 \le t \le 2\tau_\mathrm{L}. \tag{2.12}$$

Assuming that the cumulated volume increase of the equilibrium bubble at each time t during the laser pulse is proportional to the laser pulse energy E_L absorbed up to this time, Vogel et al. derived an equation for the temporal development of the equilibrium radius R_n during the laser pulse [10]

$$R_n(t) = \left\{ R_0^3 + \frac{R_{nbd}^3 - R_0^3}{2\tau_L} \left[t - \frac{\tau_L}{\pi} \sin\left(\frac{\pi}{\tau_L} t \right) \right] \right\}^{1/3} . \tag{2.13}$$

Contribution of the particle velocity behind the shock front to the bubble wall velocity

In fs breakdown, energy deposition is isochoric, and the bubble wall does not move during the laser pulse (inertial confinement). Here, a shock front forms right at the plasma boundary during the laser pulse. The initial plasma and bubble pressure P is identical with the shock pressure p_s, and the initial bubble wall velocity equals the initial particle velocity behind the shock front. This results in a "jump-start" of the bubble wall. For longer pulse durations, the bubble wall starts to move already during the laser pulse, which influences the pressure buildup during energy deposition. Here, shock front formation occurs only after the pressure transient has moved a certain distance, which depends on the laser pulse duration as well as on the plasma pressure and size. Nevertheless, the bubble wall also exhibits a rapid start due to the particle velocity in the high-pressure liquid region.

Once a shock front is formed, the particle velocity behind the shock front and the shock speed are connected through the jump conditions at the shock front, and the particle velocity u_p can be experimentally determined by measuring the shock wave velocity u_s. By doing this for different shock wave pressures in water, Rice and Walsh determined the Hugoniot relation [99]

$$u_p = c_1 \left(10^{(u_s - c_\infty)/c_2} - 1 \right), \tag{2.14}$$

where the constants are c_1 = 5190 m/s, c_2 = 25306 m/s and c_∞ denotes the sound velocity, c_∞ = 1483 m/s. With some rearrangements and the conservation of momentum at a shock front, $p_s - p_\infty = u_s\, u_p\, \rho_\infty$, one obtains a relation between particle velocity and pressure [95, 100]:

$$p_s = \rho_\infty u_p \left[c_\infty + c_2 \log_{10}\left(u_p / c_1 + 1 \right) \right] + p_\infty . \tag{2.15}$$

Here ρ_∞ = 998 kg/m^3 is the mass density of water, and p_∞=10^5 Pa is the hydrostatic pressure.

It is assumed that Eq. (2.15), which links the shock pressure to the particle velocity behind the shock front, approximates the relation between pressure and particle velocity also in a more general fashion and can be used to describe the particle velocity at the bubble wall resulting from nonlinear sound propagation at bubble wall pressure P. If the second term in the square bracket of Eq. (2.15) is expressed through its Taylor expansion and only the first term of the expansion is kept, one obtains [95]

$$P = \rho_\infty c_\infty u_p + \frac{\rho_\infty c_2}{\log(10)\, c_1} u_p^2 + p_\infty . \tag{2.16}$$

As shown in [95], resolving this equation for u_p yields

$$u_\mathrm{p} = \frac{\sqrt{\rho_\infty^2 c_\infty^2 + 4\dfrac{\rho_\infty c_2}{\log(10) c_1} P} - \rho_\infty c_\infty}{\dfrac{2\rho_\infty c_2}{\log(10) c_1}}. \tag{2.17}$$

For integrating the rapid start of the bubble wall velocity during the laser pulse into the equation of motion of the Gilmore model, Eq. (2.5), is rewritten such that it describes the evolution of the bubble wall acceleration, and a term for the time derivative of the particle velocity at the bubble wall is added [95, 96].

$$\dot{U} = -\frac{3}{2}\frac{U^2}{R}\frac{C - U/3}{C - U} + \frac{H}{R}\frac{C + U}{C - U} + \frac{U}{C}\frac{\mathrm{d}H}{\mathrm{d}R} + \dot{u}_\mathrm{p} \tag{2.18}$$

The $\dot{u}_\mathrm{p}$ term is obtained through differentiation of Eq. (2.17):

$$\dot{u}_\mathrm{p} = \frac{\dot{P}}{\sqrt{\rho_\infty^2 c_\infty^2 + \dfrac{4\rho_\infty c_2}{\log(10) c_1} P}}. \tag{2.19}$$

The evaluation of Eqs. (2.18 and (2.19) requires expressions for the time-derivative of bubble wall pressure $\dot{P}$. Liang derived the relations

$$\dot{P} = \frac{4 p_\infty R_n(t) + 6\sigma}{R_0^4} R_n^2(t) \dot{R}_n(t). \tag{2.20}$$

for inertially confined fs breakdown [95] and

$$\dot{P} = 4\left(p_\infty + \frac{2\sigma}{R_\mathrm{n}(t)} \right) \frac{R_\mathrm{n}^4(t)}{R(t)^4} \left(\frac{\dot{R}_\mathrm{n}(t)}{R_\mathrm{n}(t)} - \frac{\dot{R}(t)}{R(t)} \right) - \frac{2\sigma \dot{R}_\mathrm{n}(t) R_\mathrm{n}^2(t)}{R^4(t)}, \tag{2.21}$$

for the general case without inertial confinement [96].

Here $R_\mathrm{n}(t)$ is taken from Eq. (2.13), and

$$\dot{R}_\mathrm{n}(t) = \frac{1}{3} R_\mathrm{n}^{-2}(t) \frac{R_{nbd}^3 - R_0^3}{2\tau_\mathrm{L}} \left[1 - \cos\left(\frac{\pi}{\tau_\mathrm{L}} t \right) \right]. \tag{2.22}$$

The expansion kinetics is governed not only by the driving pressure but also by the inertia of the fluid mass that gains kinetic energy during expansion. When the driving pressure ceases, the liquid movement becomes purely inertial. For isochoric energy deposition in fs breakdown (full inertial confinement), the bubble pressure is maximal at the end of the laser pulse and drops continuously afterwards. Here, the transition from pressure-driven to inertia-driven expansion occurs only after the laser pulse, and the particle velocity behind the shock front contributes to the bubble wall acceleration during the entire pulse duration. Thus, Eq. (2.19) becomes

$$\dot{u}_\mathrm{p} = \begin{cases} \dfrac{\dot{P}}{\sqrt{\rho_\infty^2 c_\infty^2 + \dfrac{4\rho_\infty c_2}{\log(10) c_1} P}} & \text{for } 0 \le t \le 2\tau_\mathrm{L}, \\ 0 & \text{otherwise.} \end{cases} \tag{2.23}$$

with $\dot{P}$ from Eq. (2.20).

By contrast, for longer pulses without inertial confinement, the pressure rise during energy deposition and the cessation of bubble wall acceleration with transition to inertia-driven dynamics are interlaced. Initially, $\dot{P}$ is positive but $\dot{P}$ becomes negative already during the laser pulse. Because the pressure-related particle velocity in the liquid ceases to accelerate the bubble wall, when $\dot{P} = 0$, it must be considered only for $\dot{P} \ge 0$. Therefore, Eq. (2.23) becomes

$$\dot{u}_\mathrm{p} = \begin{cases} \dfrac{\dot{P}}{\sqrt{\rho_\infty^2 c_\infty^2 + \dfrac{4\rho_\infty c_2}{\log(10) c_1} P}} & \text{for } 0 \le t \le 2\tau_\mathrm{L} \text{ and } \dot{P} \ge 0, \\ 0 & \text{otherwise.} \end{cases} \tag{2.24}$$

and one must use $\dot{P}$ from Eq. (2.21).

The Liang/Gilmore model presented above enables to track the interlaced processes of energy deposition, shock wave emission and bubble wall acceleration in an elegant way without explicit modeling of the laser-induced phase transition. This is possible because the energy deposition is encoded in $R_\mathrm{n}(t)$, i.e. in the time evolution of a parameter within the framework of the Gilmore model that already assumes a gaseous bubble content.

For a description of the modeling of acoustic or shock wave emission the reader is referred to section 3.3 of Ref. [95].

Influence of tissue properties on the bubble dynamics in corneal dissection

The bubble dynamics in corneal dissection differs from spherical dynamics in water in many aspects:

- Viscoelastic properties of the corneal stroma create deviatoric forces on the bubble and dampen the oscillation. In tissues, such properties depend in a nonlinear fashion on strain and are, furthermore, a function of strain rate [3].
- The stroma with its layered structure consisting of collagen fibrils organized in lamella (Fig. 2.2 in section 2.1) is neither homogeneous nor isotropic.
- Dissection in oblique direction relative to collagen fibrils requires that the pressure within the plasma and during the initial bubble expansion exceeds the rupture threshold of the fibrils
- Dissection is performed with a scanned laser beam leaving a dissected area behind while it enters a non-dissected region, which is on one side bordered by an already dissected area and on the other side by intact stroma. Therefore, dissection may not be a mere addition of individual disruptive laser effects but could exhibit features of laser-driven crack propagation.

Numerical simulation of such complex behavior is still in its infancy. An essential step consists in adding an appropriate term for the deviatoric stress to Eq. (2.7). First attempts in that direction were based on a simple bubble model and a linear stress-strain relationship [101]. Numerical predictions were compared to experimental results on bubble dynamics in a transparent polyacrylamide (PAA) gel and to the shape of measured stress transients in cornea. Fitting results revealed that the elastic and shear modulus strongly increase with increasing strain rate and provided an orientation for the rupture stress of PAA and cornea. However, since the model did not consider the "jump start" of the bubble wall due to the particle velocity behind the plasma-induced shock front, it could not properly portray the disruptiveness of laser effect as a function of pulse energy and pulse duration. Future simulations should be based on the Liang/Gilmore model presented above and consider the nonlinearity of the stress-strain relationship [102, 103].

The present thesis focuses on the experimental exploration on the dissection dynamics. The interpretation of the experimental results will help to provide a solid basis for future modeling efforts.

2.5. Influence of focus shape, wavelength and pulse duration

As explained in section 2.1, optimum surgical and refractive outcome of LASIK and SmILE relies on precise, gentle and – if possible – bubble free corneal dissection. Precise and smooth femtosecond laser dissection requires a minimization of the spatial extent of individual laser effects. SmILE imposes particular challenges on cutting precision since the predictability of refractive correction relies completely on the precision of lenticule cutting. This precision is compromised by long plasmas generated at small numerical apertures (*NA*s) and by high pulse energies producing large cavitation bubbles. Large bubbles created during cutting of the lower lenticule face distort the overlying corneal stroma and compromise the cutting precision of the upper face. The dissection efficacy and precision and the size of the bubbles produced during cutting depend on focusing NA, laser wavelength, focus shape, and laser pulse duration

Plasma length in dependence of focusing NA

The focusing *NA* of the laser beam used for corneal dissection must generally be as large as possible to minimize the focus length. Optics design for achieving this goal is challenging because the field of view must have ≈ 10 mm diameter. Therefore, *NA*s in clinical instruments usually range between 0.2 and 0.35. A value of $NA \approx 0.5$ can be achieved only when the optics is moved during treatment and the field of view is covered by stitching individual tiles [48].

For an overfilled aperture of the focusing objective (top hat irradiance distribution), the diameter of the optical point spread function (PSF) up to the first minimum of the Airy pattern is linked to the focusing *NA* by

$$d_{\mathrm{r}} = 1.22 \frac{\lambda}{NA}, \tag{2.25}$$

and the length of the PSF up to its first minimum in axial direction is

$$d_z = 4\frac{d_z^2}{\lambda} = 5.95\frac{\lambda}{(NA)^2}. \tag{2.26}$$

The plasma length close to the bubble threshold is shorter than the length of the PSF because of the strongly nonlinear relation between free electron density and irradiance. The free-electron density at the end of the laser pulse is approximately proportional to I^k, where k is the number of photons required for multiphoton ionization [9]. This simplifying assumption corresponds to the low-intensity approximation of the Keldysh theory [52] and neglects the additional irradiance dependence of avalanche ionization that usually dominates plasma formation during the second half of a laser pulse. It leads to [9]

$$l_{\text{Plasma}} = \sqrt{k}\, d_z. \tag{2.27}$$

For λ = 1030 nm, the multiphoton order for plasma initiation is $k_{\text{ini}} = 6$, and the multiphoton order for avalanche ionization is $k_{\text{AI}} = 8$. Thus, the plasma length is approximately $\sqrt{6} = 2.45$ times shorter than the focal length if only plasma initiation is considered, and it is $\sqrt{8} = 2.83$ times shorter, if also the multiphoton order for AI is taken into account. The latter approach leads to an estimate for the plasma length of $l_{\text{Plasma}} = 23$ µm for $NA = 0.3$ and to $l_{\text{Plasma}} = 8.2$ µm for $NA = 0.5$. Hence, use of moderate NAs for corneal dissection goes along with long focal lengths and plasmas that are elongated in the direction perpendicular to the cutting direction and extend across several lamellae [Fig. 2.8(a)]. It is obvious that this constellation is suboptimal for smooth, precise, and gentle dissection.

Potential improvements by use of shorter wavelengths and focus shaping

One possible remedy is the use of a shorter laser wavelength at same NA, which reduces both focus diameter and length [Fig 2.8(b)]. The estimated plasma length at bubble threshold at 355 nm is $l_{\text{Plasma}} = 8.0$ µm for $NA = 0.3$ and $l_{\text{Plasma}} = 2.8$ µm for $NA = 0.5$. The smaller plasma length reduces the thickness of the tissue layer affected by the cutting process and provides a higher precision. UV-A wavelengths, like IR wavelengths, are invisible and do not dazzle the patients. Moreover, they enable to use compact, cost-effective lasers instead of larger fs laser systems, as described in section 2.3. However, a major concern is photochemical damage produced by the UV radiation. A wavelength of 355 nm is already far away from the DNA absorption peak around 260 nm, and the biological response per photon at 355 nm in terms of mutagenicity and cell killing is 4 to 5 orders of magnitude below the response at 260 nm (Fig. 2.9) [16]. This encourages to perform experimental investigations of corneal dissection at λ = 355 nm. Nevertheless, laser safety for ocular applications of UV-A wavelengths remains a concern and will be discussed in more detail in section 6.

Another concept for improving cutting precision and efficacy, which can be employed at any laser wavelength, is shaping of the laser focus [12, 13]. Since the focus of a Gaussian beam is strongly elongated, the orientation of the forces acting on the corneal collagen lamellae by the expanding laser plasma is not very effective for producing a cut or cleavage parallel to the corneal surface. A disk-like focus would be much better suited to cleave the corneal lamellae, as illustrated in Fig. 2.8(c).

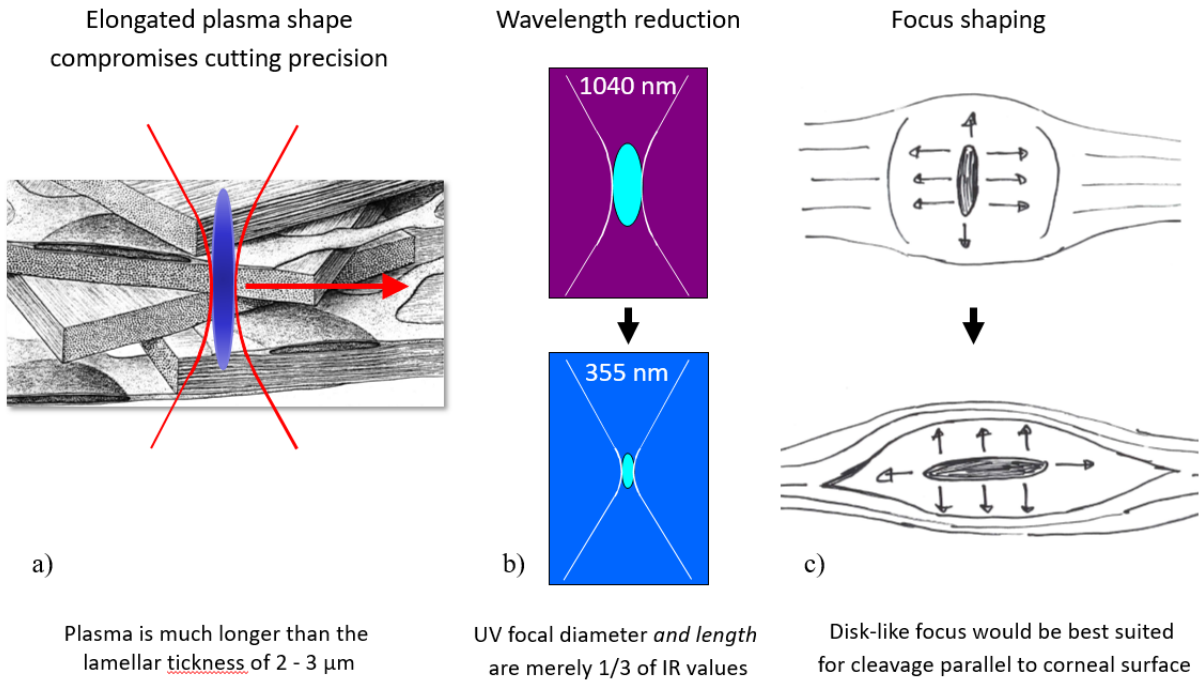

Fig. 2.8 (a) Schematic drawing of plasma orientation and size during corneal dissection in relation to thickness and orientation of the corneal lamella. (b) Comparison of focal length and diameter for IR and UV wavelengths, (b) Schematic drawing of rod- and (idealized) disk-like foci in layered corneal stroma, and of the forces exerted during plasma expansion with both focus shapes.

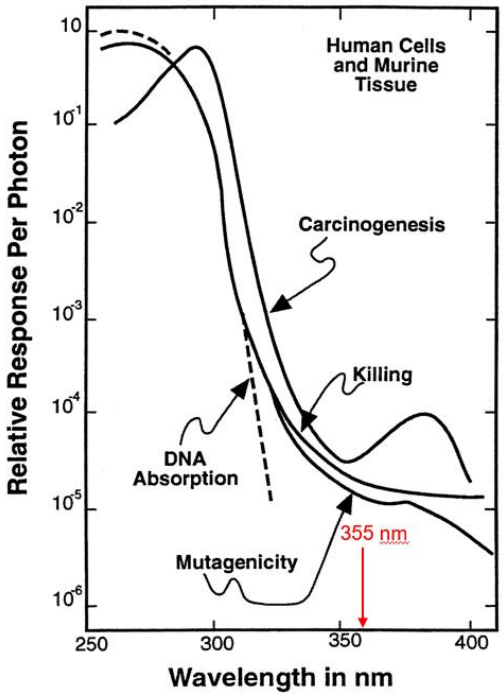

Fig. 2.9 Wavelength dependence of the biological response per photon to UV light [16].

A disk-like focus cannot be achieved optically but the ring-shaped focus produced by optical vortex beams is a step in this direction (Fig. 2.10). It has the same length as the focus of a Gaussian beam focused at same NA but a larger diameter. Thus, vortex beams are promising tools for improving cutting efficacy, which, in turn, minimizes mechanical side effects.

Moreover, the better aspect ratio improves cutting precision. Their use will be explored in section 4.

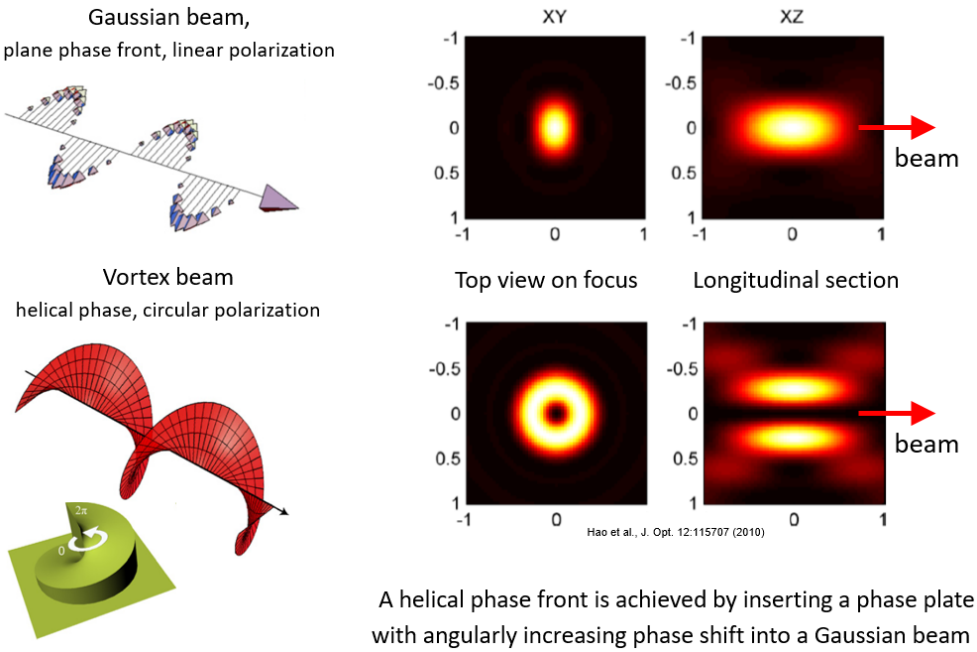

Fig. 2.10 Phase front, polarization, and focus shape of a vortex beam in comparison with a Gaussian beam. A helical phase plate with maximum phase shift $\Delta\varphi = 2\ \pi$ produces a vortex beam of order m = 1, as used in this thesis [104, 105].

Influence of laser pulse duration

The use of UV-A sub-ns laser pulses from a compact diode-pumped master-oscillator-power amplifier (MOPA) laser system instead of IR fs laser pulses raises the question of the pulse duration dependence of corneal dissection. The underlying physics is very complex because many phenomena involved in laser-induced breakdown depend on the laser pulse duration: These phenomena include 1. the energy threshold for optical breakdown, 2. the influence of nonlinear beam propagation on plasma shape [106, 107], 3. plasma absorptivity at threshold, 3. peak pressure, maximum bubble wall velocity, and the ability of the emitted acoustic transient to form a shock front. Variations of these parameters will, together with the viscoelastic properties and the rupture strength of corneal tissue, determine the respective cutting threshold. In section 5 of the thesis, the pulse duration dependence of corneal dissection is investigated for IR and UV laser wavelengths as well as for Gaussian and vortex beams.

3. Dissection Mechanisms with Gaussian Laser pulses

3.1. Motivation and objectives

Precise knowledge about the mechanisms of corneal dissection helps to optimize the cutting process and surgical outcome. Investigations by physicists have mostly focused on the physics of plasma formation and the parameter dependence of optical breakdown thresholds in water and cornea, and the bubble size in water [4, 108]. Biomedical investigations focused on the refractive outcome, surgical complications, and histological and histochemical studies of the tissue effects and the size of the laser-induced damage zone [109, 110]. However, the dynamics of the cutting process itself has hardly been studied because time-resolved studies of plasma formation and bubble dynamics in corneal stroma are very challenging. In the following, we will focus on these dynamical aspects.

Despite more than two decades of experience with LASIK and SmILE, details of the cutting process are still not well known. It remains a challenge to explore the intrastromal dissection mechanisms in order to improve efficiency, precision, and safety of the refractive procedures. As already mentioned in section 2.2, intrastromal cutting is performed with infrared femtosecond laser pulses at wavelengths between 1020 nm and 1060 nm [4, 111] and at numerical apertures (NA) between 0.25 and 0.50. The tight focusing produces very high intensities leading to nonlinear absorption and plasma formation [7, 9, 60]. The dissection mechanism depends mainly on the free electron density in the laser plasma. In the cleavage mode of dissection, fs laser pulses with pulse energies between 0.3 µJ and 1.6 µJ are applied at a repetition rate of hundreds of kHz up to a few MHz and focused in a raster pattern with 3 µm – 6.5 µm spot separation [111]. The high plasma density at the laser focus produces a high temperature and pressure that result in shock wave emission and a rapidly expanding cavitation bubble [9, 41, 112-114]. Intrastromal dissection in the cleavage mode is based on the forces exerted during shock wave emission and bubble expansion that severe and separate the stromal lamellae [4, 41, 115]. In the low-density plasma mode, laser pulses with much smaller pulse energies in the order of approximately 50 nJ are used at high repetition rates >5 MHz with an overlap between consecutive pulses [41, 114]. Due to the lower pulse energies, the free electron density in the plasma is reduced and the temperature increase is too small to generate a cavitation bubble. Dissection in the low-density-plasma mode is largely based on free-electron mediated tissue disintegration, with little disruptive components. The focus of the investigation in the present paper lies on exploring the mechanisms of corneal dissection in the more common cleavage mode.

Laser-induced cavitation in aqueous media has been studied by many researchers [8, 9, 59, 79, 92, 100, 116-118]. Individual laser parameters that influence optical breakdown and cavitation bubble dynamics are pulse duration, wavelength, pulse energy, beam quality, pulse shape, and focusing angle [7, 9, 53, 100, 119]. About 25 years ago, Juhasz et. al. performed the first investigations on laser induced bubble dynamics in cornea [113]. The bubble was imaged by stroboscopic flash photography onto a CCD camera, and the bubble dynamics was recorded by a sequence of single events with increasing time delay between pump and imaging pulses. This way, the dynamics could be tracked over a 1-millisecond time interval, with small time steps of a few nanoseconds in the initial expansion phase and steps in the microsecond range

later. Unfortunately, no view into the bubble was possible because of the collimated laser illumination, and the image quality was compromised by speckles and other coherent image artifacts. The bubbles looked round in cornea as in water - possibly because experiments were performed on bovine eyes that had been stored overnight in cold saline solution. These results have influenced artist's views on the cutting dynamics in LASIK and SmILE that over the last decades always showed round bubbles in the corneal stroma. However, the bubble shape should actually not be spherical considering that bubbles expand within a layered corneal stroma (Figs. 2.2 and 2.8).

In this section, we investigated the bubble dynamics after single laser exposures by ultra-high-speed photography with adaptable time steps. The initial bubble expansion phase is captured at 50 million frames per second and after 8 images the framing rate is reduced to 1 million frames per second to cover a total time window of almost 10 µs. White light illumination at large numerical aperture enables speckle-free imaging with good view into the bubble and on its interactions with the stromal lamellae. To cover a larger time interval of 100 ms, we used a similar approach as Juhasz et. al. and took images of different events with increasing delay time between pump pulse and illumination pulse. Measurements at fixed delay time were employed to explore the energy dependence of maximum bubble size. The bubble size was evaluated by digital image processing. In the section 4, I will show that focus shaping by vortex beams improves the intrastromal cutting quality compared to Gaussian beams [13]. To understand the observed differences in cutting quality and efficiency, the energy dependence of bubble size is investigated both for Gaussian and vortex beams in water and corneal tissue.

Furthermore, it is explored to what extent the interaction of laser-induced bubble expansion with subsequent laser pulses influences cutting in high repetition rate laser systems. The laser pulses are separated both temporally (repetition rate) and spatially (spot separation in a raster pattern) and to date all studies have focused only on one issue.

Tinne et. al. were the first to investigate the interaction mechanisms of cavitation bubbles induced by two laser pulses that were both spatially and temporally separated [120, 121]. However, there is no study yet with regard to multiple pulse interactions and their influence on the cutting dynamics in corneal stroma. In this thesis, high-speed videographic investigations of multiple pulse effects during intrastromal dissection in corneal tissue are presented. For this purpose, a large magnification and numerical aperture is required to image sufficient details but, on the other hand, the interaction of many subsequent laser pulses should be visible within the field of view. With a scanned laser beam, this would require high-resolution imaging of a field of approximately 400 µm size. Because the field of view of a microscope objective with high numerical aperture is usually much smaller, we use a stationary laser beam focused through the microscope objective and rapidly move the corneal specimen with a translation stage. The cutting dynamics and the interplay between consecutive pulses is explored by stroboscopic high-speed videography at 1 kHz, and for a better understanding of the interaction mechanisms, the cuts are inspected histologically.

3.2. Methods

The mechanisms of corneal intrastromal laser dissection were investigated in ex-vivo corneas obtained from fresh (<4 h postmortem) porcine eyes. After enucleation, the eyes were kept in a nutrient solution (Dulbecco´s Modified Eagle´s Medium, low glucose, Sigma-Aldrich, Co.) at 8°C temperature. Immediately before the experiment, the epithelial layer of the cornea was removed with a soft brush, the cornea was excised by a cut close to the corneal limbus, and an 8 mm biopsy punch (KAI Medical, BP-80F) was used to prepare a circular specimen of the cornea. Then, the corneal specimen was transferred into a custom-designed holder with exchangeable cover glasses on the front and back sides that flattened the cornea during the dissection process.

Stroboscopic photography of intrastromal bubble dynamics

A schematic drawing of the experimental setup is shown in Fig. 3.1. This setup is used in a modified version also for high-speed photography and videography. Detailed specifications of the respective components are summarized in a table in each section. For stroboscopic photography, we used a laser system with 1030 nm wavelength and 330 fs pulse duration. The laser has a very high pulse-to-pulse energy stability and a tunable repetition rate between 1 Hz and 80 kHz. The beam quality parameter is specified by the manufacturer to $M^2 = 1.09$.

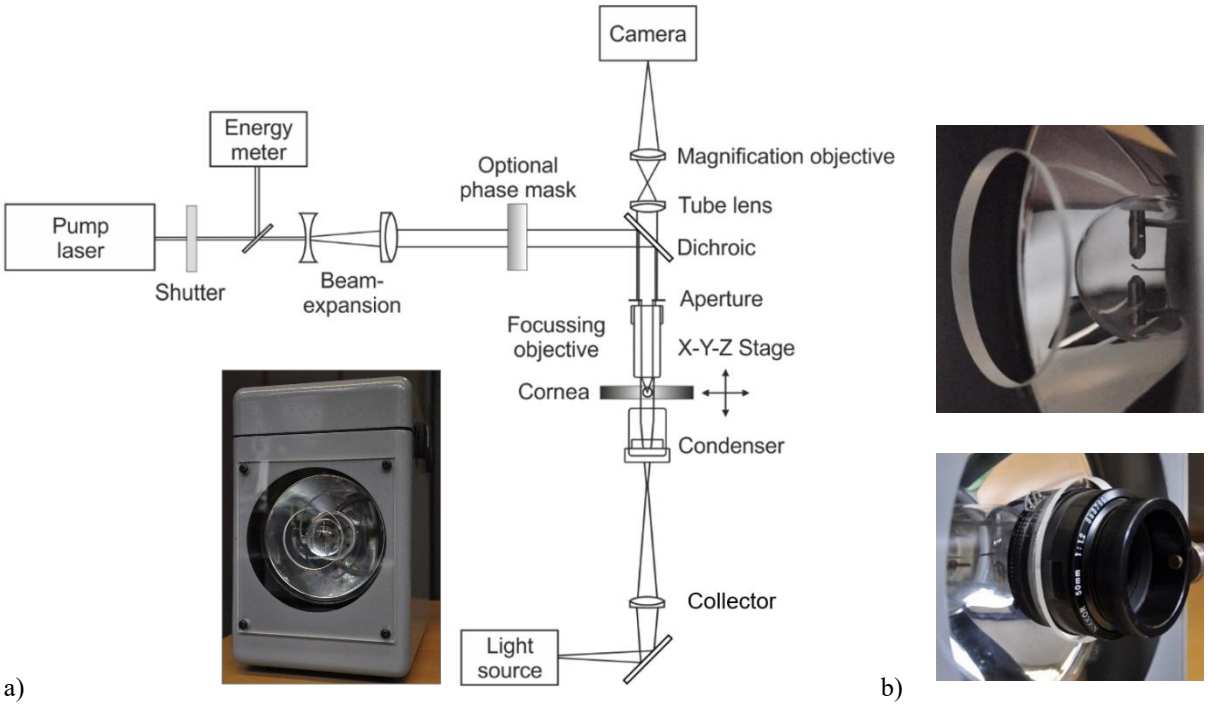

Fig. 3.1. Experimental setup for the investigation of laser induced intrastromal bubble dynamics. Specifications of the components (pump laser, focusing objective, light source, collimator, condenser, magnification objective, and camera) for stroboscopic photography, high-speed photography, and videography are presented in Tables 1 - 3. The photographs in a) and b) show the 200-J flash lamp used for high-speed photography with modifications performed for achieving the high brightness required for taking photographs at large magnification. The area illuminated by the inbuilt collimating mirror is far too large. Therefore, a collimating objective F = 1.2 is used to brightly illuminate the 100 µm x 100 µm area of interest.

Table 3.1. Detailed specifications of the components for stroboscopic photography of intrastromal bubble dynamics.

Pump laser			Objective		Light source		Collimator	Condenser	Magnification objective	Camera
Type	Wavelength	Pulse duration	Type	NA	Type	Pulse duration				
Coherent fs Staccato	1030 nm	330 fs	Zeiss LD Plan Neofluar 63x, 0.75	reduced to 0.38	Nanolite plasma discharge	20 ns	Zeiss Distagon 35 mm 1:1.4	Zeiss Plan Neofluar 20x, 0.5	Nikkor Macro 105 mm 1:2.8	Nikon D5100

It is shown in section 4 that cutting with a vortex beam producing a focus with larger lateral ring shape but same axial length as the focus of the Gaussian beam enables more precise intrastromal dissection in SmILE and LASIK with less mechanical side effects than the commonly used Gaussian beam. To compare the different cutting mechanisms, we here investigate intrastromal bubble dynamics for both Gaussian and Laguerre-Gaussian vortex beams. The vortex beam is produced by a fused-silica spiral phase plate with maximum phase shift $\Delta\varphi = 2\,\pi$ (VL-209-I-Y-A, vortex grade A, HOLO/OR Ltd., Ness Ziona, Israel) that was inserted into the beam path. The phase plate converts the linear polarized Gaussian beam into a helically phased Laguerre-Gaussian vortex beam of order $m = 1$.

Laser pulses were focused through a microscope objective into the corneal specimen. The numerical aperture (NA) of the objective was reduced to NA = 0.38 by an aperture in the rear entrance pupil to mimic focusing conditions in clinical corneal dissection. The pulse energy at the laser focus was measured by deflecting a part of the laser beam on an Ophir PD 10 energy meter. It was pre-calibrated by measuring the pulse energy without microscope objective behind the aperture. The transmittance T of the Zeiss objective at 1030 nm was considered using manufacturer data ($T = 40$ %). Individual cavitation bubbles were produced by single lasers pulses that were selected out of the 10 Hz fs pulse train by a mechanical shutter. The cutting plane was imaged through a combination of the focusing objective and a tube lens (Zeiss tube lens 452960). To achieve higher magnification, the intermediate image was further enlarged with a macro photo objective onto a digital camera (Nikon D5100, 4928 x 3264 pixel), providing a total magnification $M = 110$. The microscope objective (NA = 0.38) together with illumination at NA = 0.5 provides a diffraction-limited resolution of 0.7 µm, which is maintained in the second magnification step. The large total magnification results in significant oversampling at the camera chips such that the diffraction-limited resolution was maintained even with microchannel plates in the imaging path of the camera used for high-speed photography.

First, we investigated intrastromal bubble dynamics by stroboscopic photography of single bubble events at constant laser pulse energy. For illumination, we used the incoherent flash of a “Nanolite” plasma discharge lamp with about 20 ns duration. Because the Nanolite pulses exhibit a timing jitter of up to 500 ns, the actual delay between the pulse producing the cavitation bubble and the illumination pulse was measured for each event. Alternatively, one could use a laser-diode-based light source emitting pulses of 3 – 16 ns duration with less triggering jitter [122, 123]. A homogeneous illumination of the dissection zone was achieved by using a photo objective in front of the flash lamp as collimator and a microscope objective below the corneal specimen as condenser (Köhler illumination). Incoherent illumination at

NA = 0.5 enabled speckle-free imaging with good visualization of the bubble´s structure and of its interaction with the corneal lamellae. To investigate the entire bubble dynamics, the delay between the fs laser pulse and the illuminating flash was adjusted between 10 ns and 100 ms. The corneal specimen was moved after each shot by means of a three-dimensional translation stage in a way that laser pulses were focused at 30 µm spot separation in 150 µm depth. The individual photographs of the laser induced bubble size were analyzed to determine the radius versus time curve R(t) for Gaussian and vortex beams.

Determination of bubble size as a function of pulse energy

Determination of the bubble size as a function of laser pulse energy in corneal tissue is much more difficult than in water, where the maximum bubble radius R_{max} can be determined from the bubble oscillation time T_{osc} [119]. As a reference, we first determined the bubble threshold in water and its dependence of maximum bubble size on pulse energy at NA = 0.4 using a pump-probe-scattering technique described previously [7, 53, 119]. In tissue, the $R_{max}(T_{osc})$ relation is not known and the bubble size has to be obtained by flash photography. Because the bubble size in cornea is strongly influenced by tissue parameters, it varies from shot to shot even when the laser pulse energy remains constant. To account for these statistical variations, we used a high-speed camera (Photron SA-Z) to image a large number of single bubbles at high repetition rate. The Photron camera chip has a large pixel size of 20 µm. With the large magnification factor of M = 110 used for stroboscopic photography in 2.1 and 2.2, one pixel of the Photron chip is equivalent to 180 nm in object space, which corresponds to two times oversampling the diffraction-limited resolution of 0.7 µm. The high-speed camera enabled us to photograph a sequence of 200 single bubble events at 100 frames per second for each laser pulse energy. For this purpose, bubbles were produced at 100 Hz laser pulse repetition rate in 150 µm depth in a raster pattern over a circular dissection area of 5 mm diameter. The foci of the laser pulses were separated by translating the corneal specimen at 3 mm/s in 200 lines within the dissection area. This corresponds to a spot separation of 30 x 20 µm, sufficient to guarantee that individual events do not influence each other. The complete dissection process takes about 264 s, which provides enough time for a stepwise adjustment of laser pulse energy during the procedure from bubble threshold to maximum pulse energy. As we will later see in section 3.1, the bubble in the corneal tissue rapidly expands during the first µs and then the radius decreases very slowly. Because the bubble radius remains approximately constant for a period of ≥ 10 µs after the initial expansion phase, we investigated the dependence of the intrastromal bubble size on laser pulse energy at a fixed time delay of 3.5 µs. The high-speed series were digitally analyzed to determine the bubble size as a function of pulse energy for Gaussian and vortex beams (section 2.6).

Ultra-high-speed photography of bubble dynamics in corneal stroma with up to 50 million frames per second

The experimental setup for the ultra-high-speed photography of bubble dynamics in corneal stroma is similar to the setup shown in Fig. 1, changes are summarized in Table 2. The size of the laser-induced plasma in the cornea was minimized by using 560-ps pulses from a laser with ultraviolet (UV) wavelength (355 nm). The UV wavelength reduces the focal diameter and the focal length by a factor of 3, so that the laser-induced plasma is much more compact. The UV laser system can be controlled externally in single shot mode, and after each laser pulse, the

corneal specimen was moved 50 µm by the translation stage to a fresh position to avoid interaction with previously generated bubbles or corneal tissue that was changed in its optical properties by the laser irradiation. Pulse energies were selected such that bubbles with similar size as in previous experiments with IR fs pulses were produced [113].

Table 3.2. Detailed specifications of the components for ultra-high-speed photography of bubble dynamics in corneal stroma.

Pump laser			Objective		Light source		Collimator	Condenser	Magnification objective	Camera
Type	Wavelength	Pulse duration	Type	NA	Type	Pulse duration				
teem photonics PNV-0001525-140	355 nm	560 ps	Zeiss LD Plan Neofluar 63x, 0.75	0.75	flash lamp	20 - 50 µs	Nikkor 50 mm 1:1.2	Leica NA 0.55	Nikon 28 - 70 mm 1:2.8	Specialized Imaging SIMD16

The ultra-high speed camera (Specialized Imaging SIMD16) enabled us to capture the dynamics and interaction of individual cavitation bubbles with the corneal lamellae at up to 50 million frames per second. The camera has 8 gated high-resolution multichannel plates (MCPs) with a dynamic range of 12 bits on the CCD image sensor (ICX285AL, 1360 x 1024 pixel). The 18-mm high-resolution MCP features a variable gain up to a factor of 10 000. The camera is able to record up to 16 images in two sequences of 8 frames with 20 ns interframing time and 10 ns exposure time. This corresponds to a maximum frame rate of up to 50 million images per second. The image separation can be changed after the first sequence of 8 frames, so that longer observation times can be covered by the second sequence. The magnification factor $M = 140$ was selected such that the maximally expanded intrastromal cavitation bubble largely filled the size of the image sensors. This way, the influence of MCP inherent noise was minimized.

The short exposure time of 10 ns puts high demands on the light source for imaging. We used a plasma discharge lamp with a pulse duration of 20 – 50 µs (sufficient for the illumination of the entire high-speed series) and 200 J pulse energy. The 10-ns exposure time of the individual images is provided by the electronic gate of the MCPs. Köhler illumination by a combination of a photo objective ($F = 1.2$) as collimator and a microscope condenser (Leica, NA 0.55) was used to illuminate the 61 x 45 µm large object field with sufficiently bright light. The diffraction limited resolution for illumination at NA = 0.55 and imaging at NA = 0.75 is < 0.5 µm.

High-speed videography of cutting dynamics

The experimental setup is similar to the setup in Fig. 3.1 with small modifications listed in Table 3. UV laser pulses (355 nm, 560 ps) emitted at 1 kHz were focused in 150 µm depth into the corneal stroma. The numerical aperture of the objective was reduced to NA = 0.38 to mimic focusing conditions used in clinical systems. The corneal specimen was moved by the translational stage at 6 mm/s and a flap of 4 mm diameter was cut with 6 x 6 µm spot separation. The dissection zone was imaged through the focusing objective combined with a tube lens and further magnified by a photo objective onto a high speed video camera (Basler 503k). The total magnification was $M = 110$ and the field of view 133 x 87 µm. The camera had a gate time of 829 µs, and stroboscopic illumination was realized by synchronizing the “Nanolite” plasma

discharge lamp with 20 ns flash duration to the gate opening time. The delay of the flash lamp was adjusted to 2 µs and 24 µs after the laser pulse. At 1 kHz repetition rate, the flash lamp should not emit more than 100 pulses in one sequence to avoid damage due to thermal overload. Therefore, we restricted the length of the video sequences to 60 – 65 images. The laser pulse repetition rate in investigations with stationary laser beam is limited by the possible speed of the translation stage moving the specimen and is, thus, lower than in clinical systems.

Table 3.3. Detailed specifications of the components for high-speed videography of cutting dynamics.

Pump laser			Objective		Light source		Collimator	Condenser	Magnification objective	Camera
Type	Wavelength	Pulse duration	Type	NA	Type	Pulse duration				
teem photonics PNV-0001525-140	355 nm	560 ps	Zeiss LD Plan Neofluar 63x, 0.75	reduced to 0.38	Nanolite plasma discharge	20 ns	Zeiss Distagon 35 mm 1:1.4	Zeiss Plan Neofluar 20x, 0.5	Nikkor Macro 105 mm 1:2.8	Basler 503 k

Histology of corneal specimens

Histology was performed on corneal specimens dissected with pulse energies (0.7 µJ to 1.2 µJ) and spot separations (4 µm to 6 µm) that are often used in clinical settings. The flap was not lifted after dissection, but the entire corneal specimen was fixated for 48 hours following the protocol of Grazadei et. al. [124]. After this, the specimen was dehydrated in propyleneoxide (1,2-epoxy propane), embedded in epoxy (Epon 812, Araldite 502, Sigma Aldrich) and stained with Toluidine blue. Series of semi thin sections (0.7 µm) were cut for light microscopic analysis. In addition, classical Paraffin sections stained with Hematoxylin and Eosin (H&E) were prepared for overviews of the dissected regions.

Digital image processing

Manual evaluation of the bubble size from the high-speed photographic image series is not manageable due to the large amount of data (4000 images were recorded in the stroboscopic measurement series. Therefore, determination of the bubble size was automated using digital image processing based on Matlab software (MathWorks, Inc). The algorithm starts with a regularized gradient-based edge detection in which the derivation in one direction and smoothing in the other direction is used to find the boundary of the bubble wall. The filter is based on the imaginary part of the Gabor transformation (Gabor filter edge detection) and a threshold relative to the maximum of the gradient amount is used to determine the contour of the bubble. In addition, if there is a gap in the bubble edge, the contour is closed by the software. The closed contour is then reduced to a line with a width of one pixel.

The sequence from the original image through gradient formation, contour determination and thinning of the contour line to the finally determined bubble edge is shown in Fig. 2. To determine the bubble size, the number of pixels within the bubble contour is converted into an area which is then transformed to an area-equivalent spherical bubble radius R. The large image magnification ($M = 110$) provides a high precision of the digital analysis. The accuracy of the determination of the position of the contour line is in the order of one pixel and, hence, better than 0.18 µm in object space. Systematic errors in the determination of the bubble wall position

owing to the diffraction ring around the bubble would influence the absolute radius value but not affect the parameter dependence of bubble radius on time or laser pulse energy.

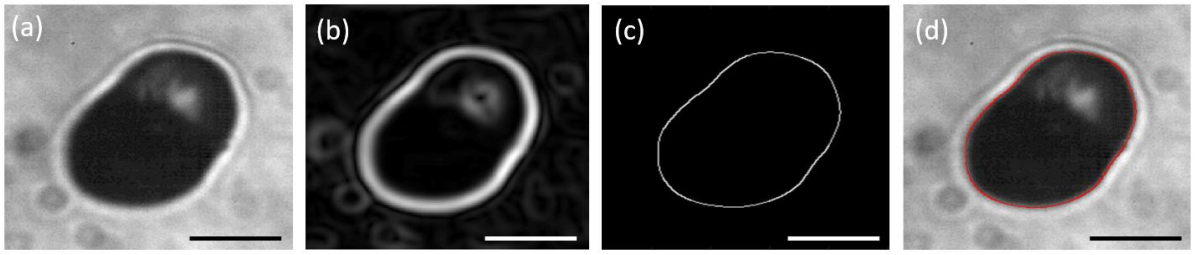

Fig. 3.2. Sequence of digital imaging processing for the determination of the bubble size from (a) original image, (b) gradient based Gabor filter detection, (c) thinning of the contour to a line with one pixel width, (d) final outcome of the bubble wall detection (red line). The reference bar in the images corresponds to 10 μm.

3.3. Results

Time evolution of intrastromal bubble dynamics over 100 ms

Figure 3.3 summarizes intrastromal bubble dynamics induced by single laser pulses with Gaussian and vortex beam profiles as determined by stroboscopic photography. The energy of the laser pulses was adjusted for both beam profiles (Gauss: 162.5 nJ, Vortex: 329.9 nJ) such that the maximum bubble radius R_{max} is in the range between 10 µm and 12 µm, which will certainly suffice for refractive surgery at 6 x 6 µm spot separation. The investigation at equal maximum radius allows a direct comparison of the bubble dynamics for Gaussian and vortex beams. To achieve the same maximum bubble size, we had to use laser pulse energies that are 3x (Gauss) and 1.9x (Vortex) above the cutting threshold ($E_{cut,Gauss}$ = 54 nJ and $E_{cut,Vortex}$ = 173 nJ).

Figure 3.3 clearly shows that the intrastromal bubble dynamics is similar for both beam profiles. The bubble radius increases very rapidly within the first 200 - 300 ns. After the maximum bubble size has been reached, the radius collapses to about 80 % of R_{max} within 1 µs after which it slowly decreases between 2 µs and 100 ms from about $R \approx 7$ µm to $R \approx 6$ µm. The long time interval of almost constant bubble size allows us to investigate the dependence of intrastromal bubble size on laser pulse energy at a fixed time delay of 3.5 µs.

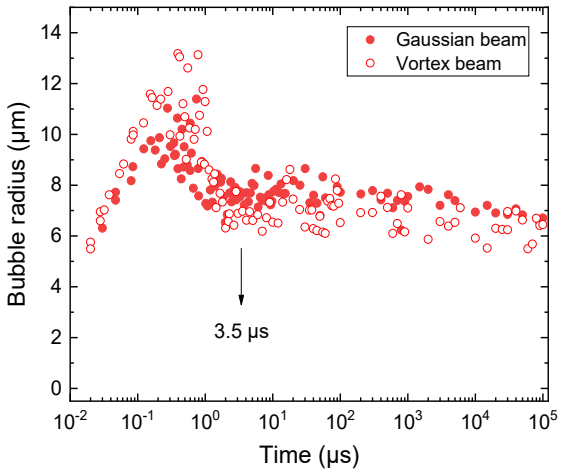

Fig. 3.3. Intrastromal bubble dynamics 20 ns to 100 ms after focusing laser pulses with Gaussian (red dots) and vortex (red circles) beam profile at NA 0.38 into the corneal stroma.

Dependence of bubble size on pulse energy

Figure 3.4 (a) shows a representative video with a sequence of 200 photographs of laser induced intrastromal bubbles at one pulse energy that were imaged 3.5 µs after the laser pulses. For better visibility, the photographs were converted into a video with 10 images per second. The bubbles in the video were generated by focusing single laser pulses with a vortex beam profile and 270 nJ pulse energy into the corneal stroma. It is clearly visible that the bubble size strongly fluctuates from shot to shot even though the laser pulse energy is almost constant. Furthermore, the bubbles within the corneal stroma are not spherical, rather, the bubble shape is partially elongated and the shape fluctuates from shot to shot. Therefore, the bubble size was evaluated by digital image processing and the red line in the video represents the bubble wall automatically determined by the algorithm presented in 2.6. To compensate for the shape fluctuations, the cross sectional area within the closed red line was calculated and converted into an equivalent spherical radius.

Figure 3.4 (b) summarizes the dependence of bubble size on laser pulse energy for Gaussian and vortex beams. The threshold for photographically detectable bubble formation was 46.8 nJ (Gauss) and 148.6 nJ (Vortex). Above threshold, the bubble size increases rapidly with increasing laser pulse energy to R = 5.0 µm (Gauss) and R = 6.3 µm (Vortex) at 2 times bubble threshold. The increase in bubble size with laser pulse energy is, thus, steeper for the vortex beam than for the Gaussian beam.

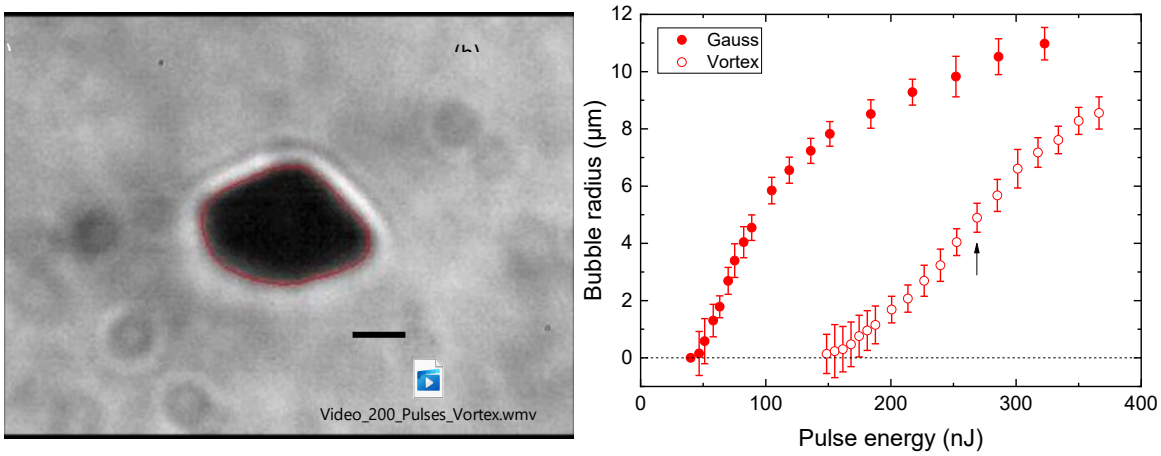

Fig. 3.4. (a) Representative video of 200 individual intrastromal bubbles generated by laser pulses (1030 nm wavelength, 330 fs pulse duration) at 100 Hz repetition rate (see Visualization 1). Laser pulses with 270 nJ single pulse energy and a vortex profile were focused through NA 0.38 into 150 µm corneal depth. Photographs were taken 3.5 µs after each laser pulse. The size of the bubble was evaluated by digital image processing and the automatically detected bubble wall is visible as red line in each image. The reference bar is 10 µm. (b) Bubble size (radius) in dependence on pulse energy for Gaussian and vortex beam profile. The black arrow at 270 nJ marks the data shown in (a).

For an even better comparison, the photographically determined bubble radius in porcine cornea is shown together with the maximum bubble radius in water in dependence on the laser pulse energy in Fig. 3.5 on a double logarithmic scale. Additionally, the energy required for successful flap dissection is marked both for Gaussian and vortex beams. The threshold for flap dissection was determined as described in section 4. We performed flap cuts with different pulse energies and afterwards the flap was lifted using a hockey knife. The quality of the dissection was judged subjectively and classified into one of the three categories: (1) no flap lifting, (2)

hard flap lifting, or (3) easy flap lifting. Depending on this classification, the laser pulse energy was then either increased or decreased to determine the minimum value required for easy flap lifting. This procedure was repeated in 10 different corneas for both the Gaussian and the vortex beam. The transition from "hard" to "easy" flap lifting required an energy increase of less than 10%, so that the uncertainty of the respective threshold values is in the range ± 5%.

Figure 3.5 shows that bubbles in cornea are generated already at pulse energies below the threshold for bubble formation in water (63.2 nJ Gauss, 172.1 nJ Vortex). The bubble formation threshold in cornea could be even lower, because very small bubbles in cornea may have already disappeared in the photographs taken 3.5 µs after the laser pulse. Hence, for equal energies in the threshold range, bubbles in water are smaller than in cornea. Well above threshold, the picture then changes and the bubble radius in water is 4x larger than in cornea.

At the flap cutting threshold the bubbles are significantly smaller with the vortex beam. The bubble radius at the energy required for flap cutting at 6 x 6 µm spot distance is $R = 1$ µm for the Gaussian beam and $R = 0.7$ µm for the vortex beam, which corresponds to a 3 x reduced bubble volume.

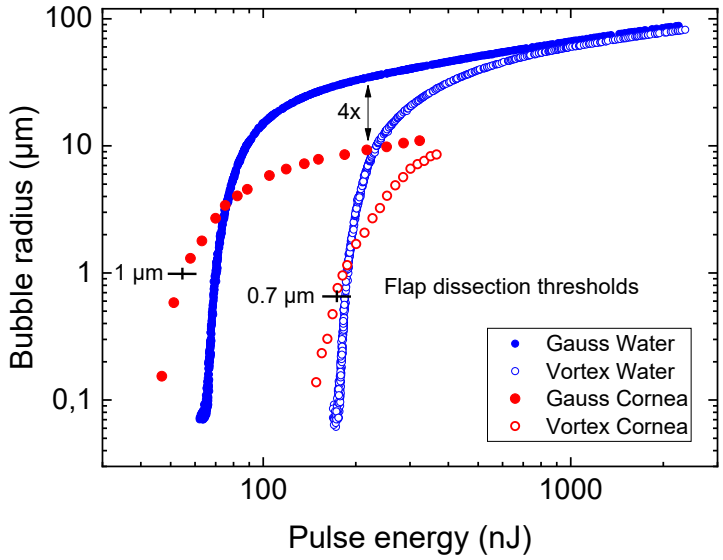

Fig. 3.5. Photographically determined bubble size in cornea (red) and maximum bubble size in water (blue) in dependence on laser pulse energy for Gaussian (dots) and vortex (circles) beams at NA 0.38 (1030 nm wavelength, 330 fs pulse duration). The threshold energy required for smooth flap cutting at 6 x 6 µm spot distance is marked in the graphs and amounts to 54 nJ (Gauss) and 173 nJ (Vortex). For these pulse energies, the bubble radius for individual intrastromal bubbles amounts to 1 µm and 0.7 µm, respectively.

Ultra-high-speed photography of the interaction between individual bubbles and corneal lamellae

Figure 3.6 shows an ultra-high-speed photographic series of intrastromal bubble dynamics induced by a single laser pulse with 2 µJ pulse energy. The laser pulse energy is 3 times above the energy required for successful flap dissection (section 4.3) and amounts to 0.67 µJ at 6 x 6 µm spot separation. The relatively high laser pulse energy enables a more detailed investigation of the interaction of the cavitation bubble with the surrounding corneal lamellae and a comparison with the results obtained previously by Juhasz et al. [113].

The first eight frames in Fig. 3.6 show the initial bubble expansion within the first 125 ns after the laser pulse. These pictures are taken with extremely high temporal resolution (10 ns exposure time) and spatial resolution (below 0.5 µm) at 50 million frames per second. Due to the high pressure and temperature during optical breakdown, the bubble grows very fast and already after 125 ns, the bubble has a radius of more than 10 µm. However, it can also be seen from the images that the bubble does not look spherical: The bubble has a lobular structure with lobes expanding along the direction of the collagen fibrils in the individual lamellae. The fact that a stack of 4-5 lobes is seen on the images indicates that the plasma producing the bubble extends across several lamella and is 10 – 15 µm long.

Frames 8-16 in the ultra-high-speed series in Fig. 3.6 are taken with 1 million frames per second and show the initial collapse phase of the bubble during the first eight microseconds. The maximum bubble radius in the image photographed 545 ns after the laser pulse is approximately 20 µm, and four lobes lying on top of each other are identifiable. The bubble then slightly decreases in size during the following first micro second but remains almost constant in size and shape during the next 7 frames covering a time interval of 7 micro seconds.

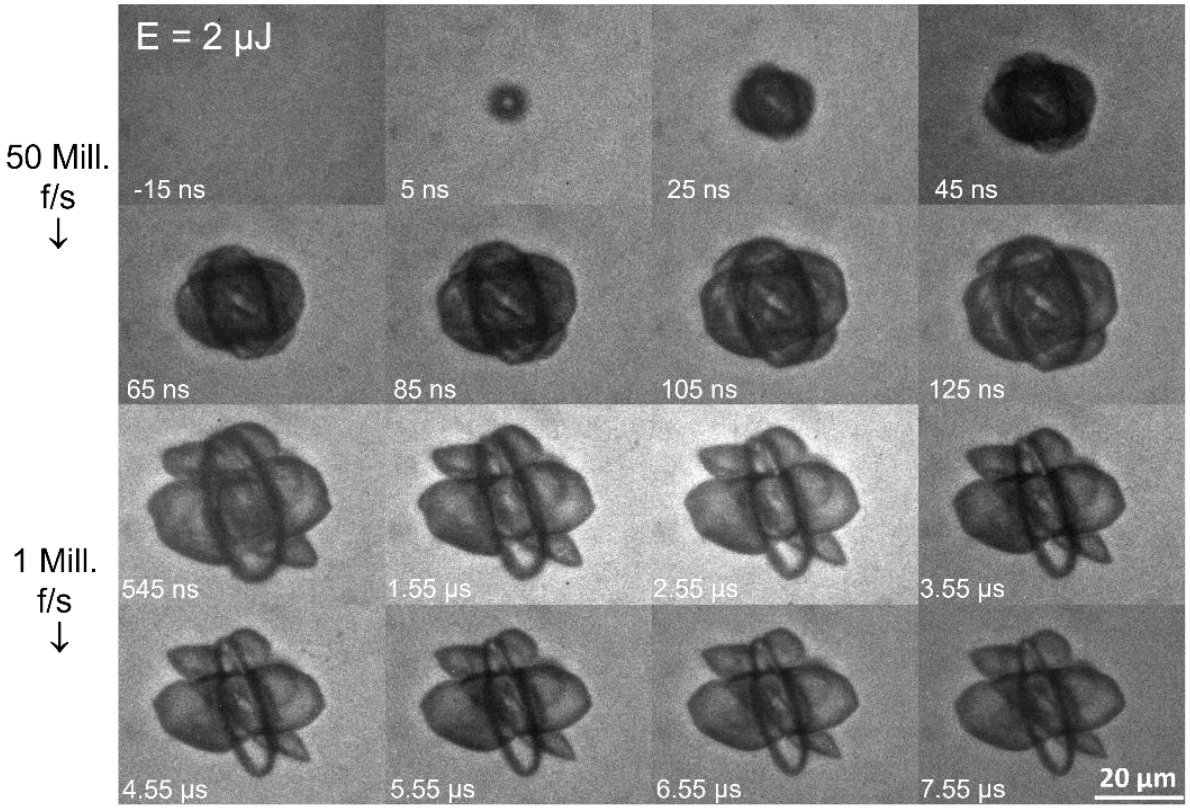

Fig. 3.6. High-speed photography of intrastromal bubble dynamics. A single laser pulse (355 nm wavelength, 560 ps pulse duration) with 2 µJ pulse energy was focused at NA 0.75 in 150 µm depth into the porcine cornea. The view is from the top, along the axis of the laser beam producing the bubble. The first 8 pictures are taken at 50 million frames/s, the following 8 pictures at 1 million frames/s. Imaging times are shown in each photograph. They refer to the center of the time windows set by the 10-ns camera exposure time.

The collapse phase becomes even more interesting when looking at a longer time period, as presented in Fig. 3.7. Here, the bubble dynamics is captured at smaller laser pulse energy (1.2 µJ) than in Fig. 3.6 (2 µJ). The first five photographs are taken at 1 million frames per

second and the following three photographs at 150 000 frames per second, which allows a longer observation time of 17.6 µs. Due to the lower pulse energy, the laser-induced plasma is shorter and only two overlapping bubble lobes are formed. The high speed images of the collapse phase show that the small lobe collapses first and pushes its content into the bigger bubble. The vertically in the image plane oriented, elongated bubble part (marked by blue arrows) collapses from the sides, not from the ends as it would occur in water. The collapse is, therefore, probably driven by the elastic force exerted by the collagen fibrils which are elongated along the bubble axis.

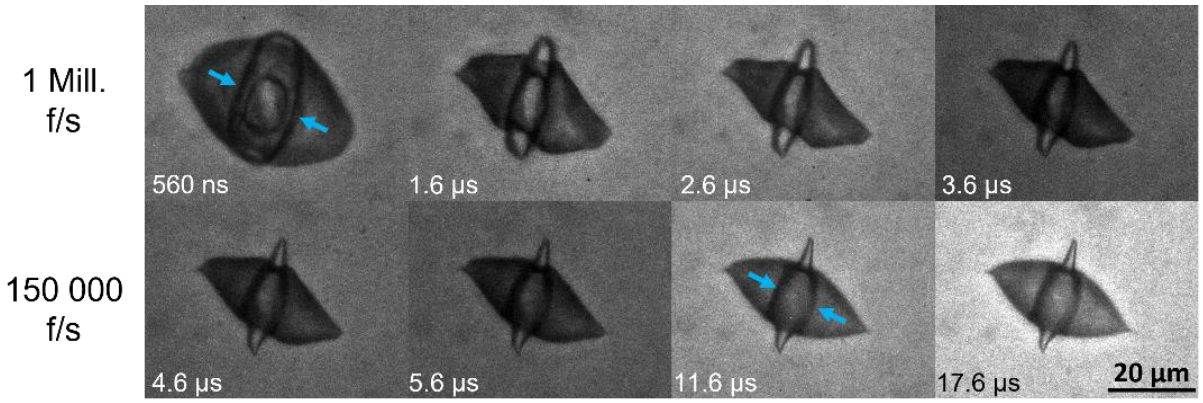

Fig. 3.7. High-speed photography of the collapse phase during intrastromal bubble dynamics. A single laser pulse (355 nm wavelength, 560 ps pulse duration) with 1.2 µJ pulse energy was focused through NA 0.75 in 150 µm depth into the porcine cornea. The view is from the top, along the axis of the laser beam producing the bubble. The first 5 pictures are taken at 1 million frames/s and the last 3 pictures at 150000 frames/s. Imaging times are shown in each photograph.

Figure 3.8 shows an ultra-high-speed series of intrastromal bubble dynamics at even higher pulse energy (3 µJ). The first eight photographs show the initial, fast bubble expansion during the first 150 ns. The bubble dynamics is very similar to the dynamics shown in Fig. 6, even at the higher pulse energy when the entire bubble gets larger. The next five photographs in Fig. 3.8 are taken at 1 million frames per second followed by three photographs at 150 000 frames per second, which allows an entire observation period of 17.6 µs. Again, multiple overlapping bubble lobes are formed within the corneal stroma that collapse slowly from their sides, where the collagen fibers are elongated. We evaluated the size of the bubbles in Fig. 3.8 to obtain insights on the bubble dynamics during initial and collapse phase. Fig. 3.9 shows the temporal evolution of the equivalent spherical diameter on a logarithmic time scale between 5 ns and 17.6 µs.

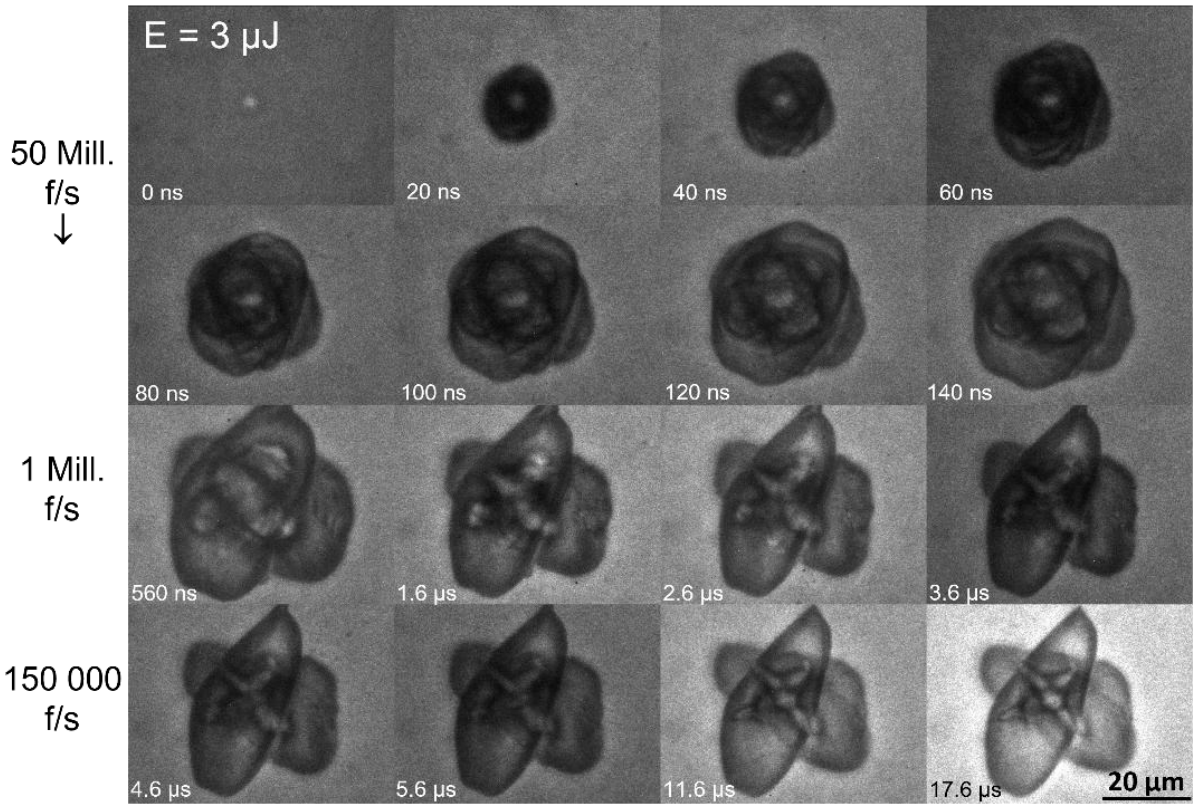

Fig. 3.8. High-speed photography of intrastromal bubble dynamics. A single laser pulse (355 nm wavelength, 560 ps pulse duration) with 3 µJ pulse energy was focused at NA 0.75 in 150 µm depth into the porcine cornea. The view is from the top, along the axis of the laser beam producing the bubble. Imaging times are shown in each photograph.

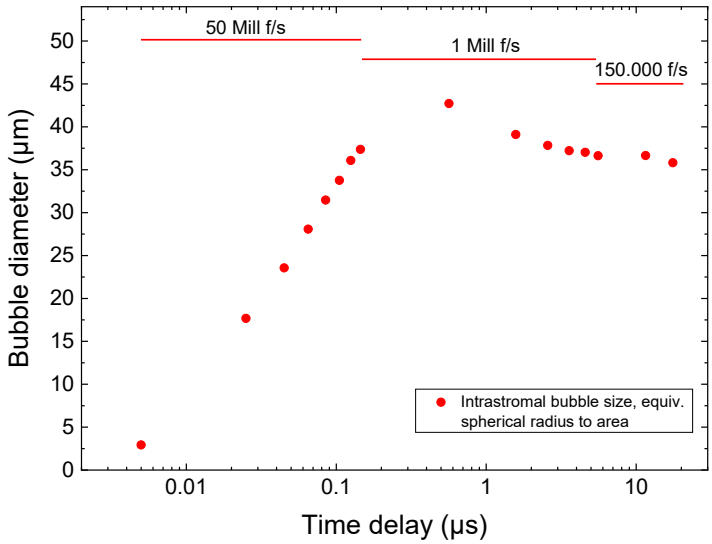

Fig. 3.9. Evaluation of the bubble dynamics from single-shot ultra-high-speed photography of intrastromal bubble formation (Fig. 8). A single laser pulse (355 nm wavelength, 560 ps pulse duration) with 3 µJ pulse energy was focused through NA 0.75 in 150 µm depth into the porcine cornea.

High-speed videography of cutting dynamics

Figure 3.10 shows high speed videography of intrastromal cutting dynamics with (a) 1.2 µJ and (b) 2.3 µJ laser pulse energy at 1 kHz repetition rate. These energies are 1.8 and 3.4 times larger than the energies required for successful flap dissection, respectively. The time delay between laser pulses and flash illumination was 2 µs. The corneal specimen was moved below the stationary focus at constant velocity (6 mm/s) so that the laser foci were separated by 6 µm. The corneal specimen in the videographs in Fig. 10 was moved from right to left and the videos show the interaction of 65 consecutive laser pulses. The upper part of the specimen shows already separated tissue in which a homogeneous bubble layer appears.

On the videos, the interaction of the laser pulses with residual bubbles from previous laser pulses as well as the interaction of the bubble with the surrounding corneal lamellae can be observed. In some cases, the laser pulses are focused into the already existing bubble layer, so that hardly any energy is deposited. However, as soon as the laser pulse reaches corneal tissue again, a cavitation bubble is formed, which then spreads along the corneal lamellae. As a result, partially pointed bubble lobes are formed. Overall, this results in a progressive dissection of the tissue along the pre-existing bubble layer, with the cavitation bubble always separating a new section of the tissue in the direction along the cutting movement.

Figure 3.11 shows high speed videographs of intrastromal cutting dynamics with lower pulse energy (a) at threshold for flap cutting (0.64 µJ) and (b) 1.8 times above threshold (1.2 µJ). The time delay between laser pulses and flash illumination was 24 µs. Although the delay time is longer than in Fig. 10, the cutting mechanics is very similar, which is due to the slow collapse phase of the intrastromally generated cavitation bubbles, as already shown in the previous sections.

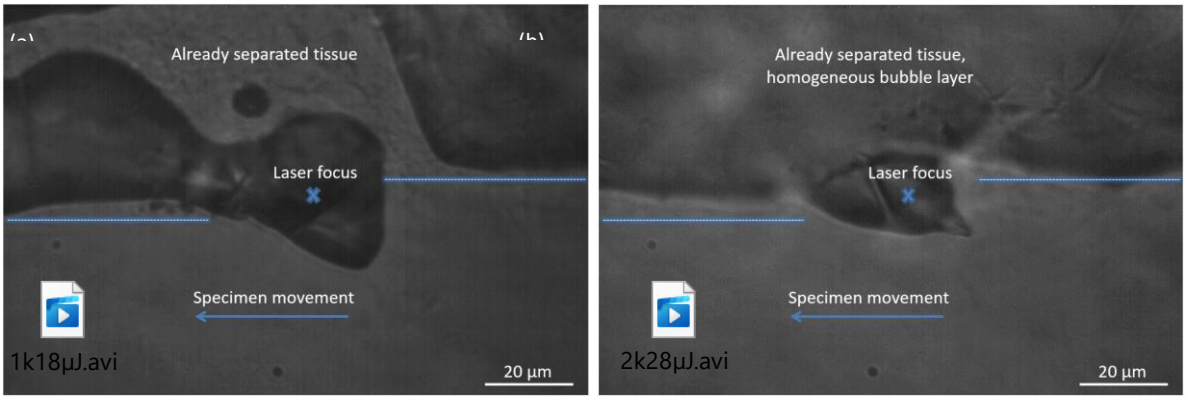

Fig. 3.10. High-speed videography of intrastromal dissection at 1 kHz with (a) 1.2 µJ and (b) 2.3 µJ laser pulse energy (see Visualization 2 and 3). The view is from the top, along the axis of the laser beam producing the dissection. The video shows the interaction of 65 consecutive laser pulses (355 nm wavelength, 560 ps pulse duration) that were focused at NA 0.38 into 150 µm depth in porcine cornea. Time delay between laser pulse and flash illumination was 2 µs.

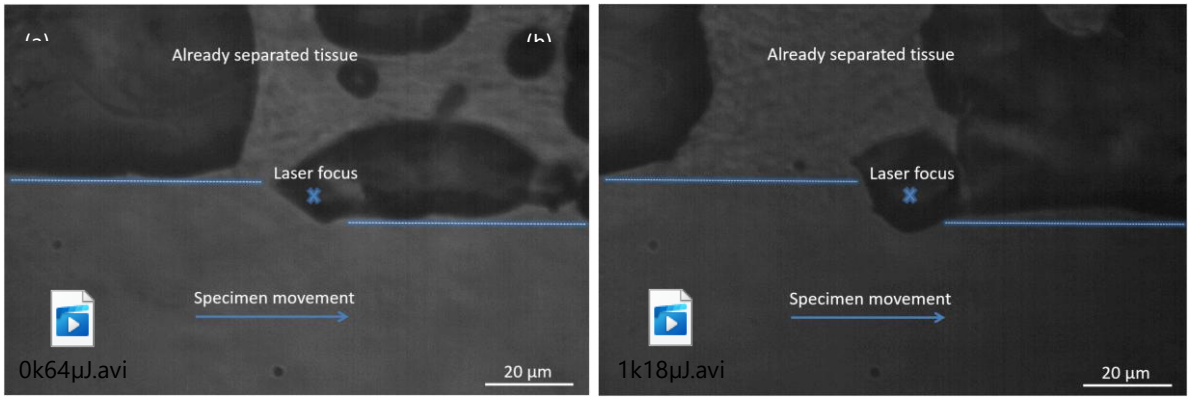

Fig. 3.11. High-speed videography of intrastromal dissection at 1 kHz with (a) 0.64 µJ and (b) 1.2 µJ laser pulse energy (see Visualization 4 and 5). The view is from the top, along the axis of the laser beam producing the dissection. The video shows the interaction of 65 consecutive laser pulses (355 nm wavelength, 560 ps pulse duration) that were focused at NA 0.38 into 150 µm depth in porcine cornea. Time delay between laser pulse and flash illumination was 24 µs.

Histology of corneal specimens

Figure 3.12 shows a histology image of a corneal specimen stained with H&E after intrastromal dissection. The laser pulse energy was 0.69 µJ, slightly above threshold for successful flap dissection at 4 µm spot separation. The flap has a thickness of 200 µm and the intrastromal cut is hardly visible in the histology. Some large residual bubbles within the dissection area are visible, but neither the bubble size nor the number of bubbles are correlated to the initial laser spot separation. Instead, the cut has closed again and the residual gas has collected in isolated large bubbles along the cutting plane.

For more details, Fig. 3.13 shows semi-thin histological sections of corneal specimens after dissection stained with Toluidine blue at larger magnification. Large cavities with diameters between 5 µm and 30 µm are formed within the dissection plane as seen in Fig. 3.13 (a). The cuts have closed through surface tension, which also drives coalescence of the residual gas into large bubbles. The layer thickness influenced by intrastromal cutting is below 10 µm thickness, especially in the reclosed regions. However, the thickness of material removal in the dissection plane is much smaller than 10 µm because the stroma was cleaved along the lamellar structure. Fig. 13 (b) shows that local tissue bridges can arise, when lamellae cross the cutting plane. These tissue bridges lead to difficulties in flap lifting.

Fig. 3.12. Overview of an intrastromal dissection in 200 µm depth using laser pulses with 355 nm wavelength, 560 ps pulse duration, and 0.69 µJ pulse energy focused at NA 0.38 into porcine cornea. Spot separation 4 x 4 µm, Paraffin embedding, H&E staining. Residual bubble are formed within the dissection plane.

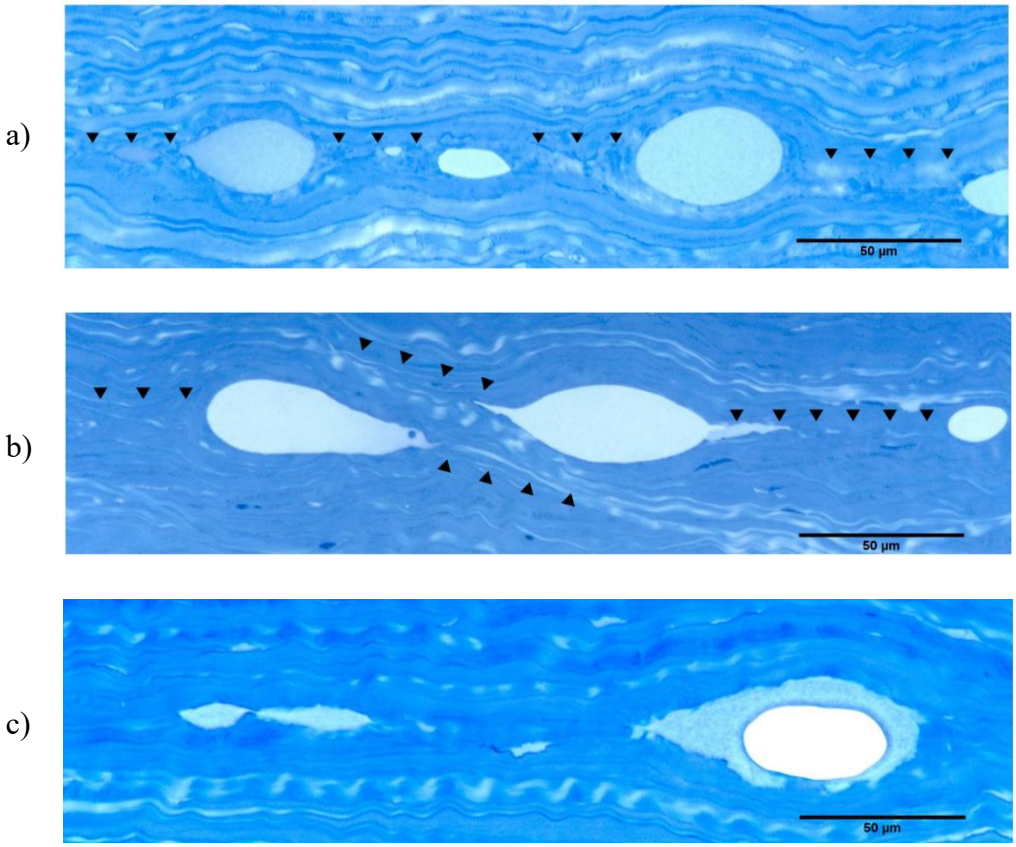

Fig. 3.13. Semi-thin histological sections of intrastromal dissections in porcine cornea performed using 355-nm, 560-ps laser pulses with 0.85 µJ pulse energy focused at NA 0.38 in (a) and at NA 0.28 in (b) and (c). Spot separation 4 x 4 µm, Araldite resin embedding, Toluidine blue staining. The laser beam was incident from the top of the images. The dissection/cleavage plane is marked by arrows. In (b), the dissection was not smooth but cleavage occurred along lamellae with oblique orientation such that a tissue bridge was formed. Cuts close locally after dissection and, due to surface tension, gas produced by tissue disintegration and water dissociation in the plasma collects in large bubbles. In (c) cavities are filled with gas, debris, and probably exudates from surrounding stroma.

Figure 3.14 shows semi-thin histological sections of corneal specimens after dissection stained with Toluidine blue at even higher magnification. The dissection zone can be identified by a slightly modified shape of the lamellar structure, with a thickness of less than 4 µm. Cutting is involves crack formation between the lamellae and cleavage. Fig. 3.14 (a) shows a smooth intrastromal cut with interspersed gas bubbles. These bubbles have an elongated shape along the horizontally oriented corneal tissue lamellae. The crack between the bubbles is closed through surface tension. In contrast, the cut shown in Fig. 3.14 (b) seems to involve a region with lamellae crossing the dissection plane in the central part of the image. This crossing reduces crack formation along the lamellar structure. In Fig. 3.14 (c), a subsidiary crack oriented in 60° upward direction relative to the lamellar orientation deviates from the main dissection cleavage close to one edge of the gas bubble. Such cracks may also lead to tissue bridges that make it difficult to detach the flap.

a)

b)

c)

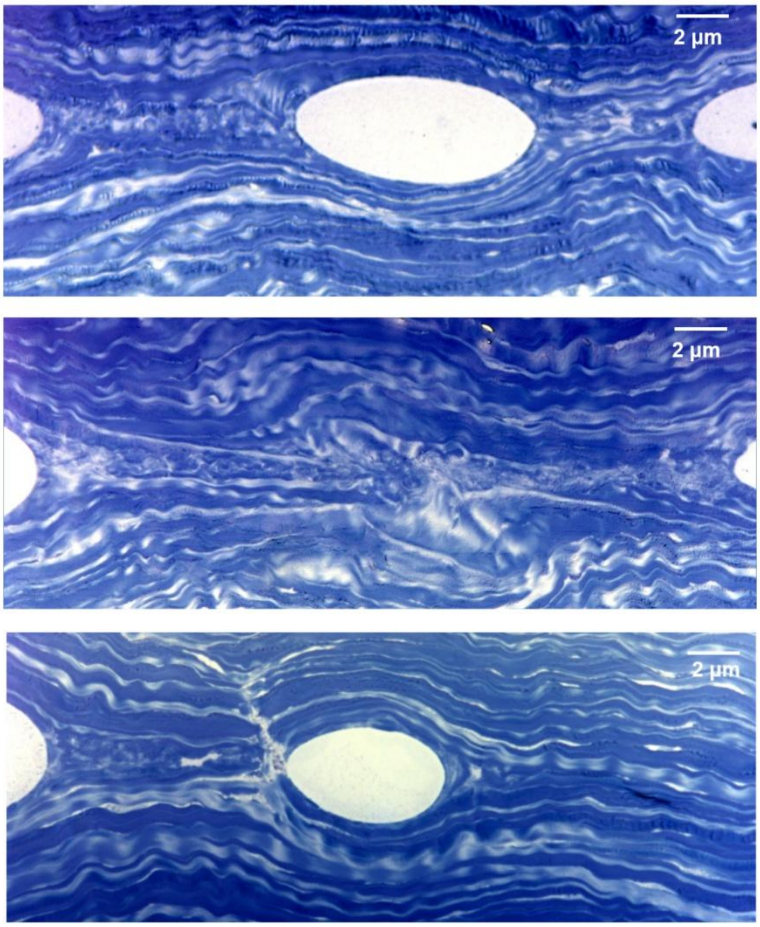

Fig. 3.14. Semi-thin histological section of an intrastromal dissection using laser pulses with 355 nm wavelength, 560 ps pulse duration, and 1.2 µJ pulse energy focused at NA 0.38, spot separation 6 x 6 µm. Araldite embedding, Toluidine blue staining. The laser beam was incident from the top of the images. The dissection plane in (a) and tissue bridges in in the center of (b) are clearly visible. In (c), one can identify the formation of a subsidiary crack oriented in 60° upward direction away from the main cleavage plane.

3.4 Discussion

Understanding intrastromal bubble dynamics und the mechanisms of corneal laser dissection requires consideration of the anatomical structure of the cornea (Fig. 2.2). Intrastromal dissection is usually performed in the corneal stroma in the anterior part 100 - 200 µm below the front surface. The corneal stroma amounts to 90 % of the entire corneal thickness. The major structural element of the stroma is fibrillar type I and V collagen, which has approximately 70 % of the corneal total dry weight [125-127]. The collagen in the human cornea forms long fibrils with a diameter of 31 to 34 nm [128]. Size, spacing and stability of the fibrils are regulated by nonfibrillar collagen (type VI) and proteoglycans in the interfibrillar matrix [125]. The organization of collagen fibrils into independent bundles leads to collagen fibers of approximately 1 to 2 µm thickness and up to 100 µm width, also known as corneal lamellae [115]. The lamellae are oriented in-plane across the cornea and are stacked vertically in 2 -3 µm thick layers. Thereby, the lamellae in the central cornea are aligned predominantly along the horizontal or vertical axis of the cornea, and each layer has a preferential orientation rotated by 90° relative to its neighbors [129]. At the posterior end, near Descement´s membrane, the fibers run in parallel almost entirely uninterrupted for several millimeters [130]. In contrast, the collagen organization in the anterior part of the cornea relevant for intrastromal dissection is much more complex. Within the first 150 – 200 µm of the cornea, fibers can change direction and interact with adjacent fibers. It was shown in studies by two-photon generated second harmonic signals that sutural fibers can run upward and insert into Bowman´s layer collagen [131, 132] (Fig. 3.15). Winkler et. al. showed that collagen fibers in the anterior stroma tend to branch into multiple distinct fibers that then fuse with each other or even with unrelated fibers originating from a different layer [133]. Furthermore, they identified new collagen fiber types named bow-spring and anchor-like fibers. Bow-spring like fibers originate from the intertwined layers beneath the Bowman´s layer, and arc up and backward through the underlying layers in a near-parabolic shape, whereas anchor like fibers originate near the limbus and extend for several millimeters through different layers across the cornea [134]. Transmission electron microscopy images also showed a larger degree of interconnectivity between fibrils in the anterior stroma in comparison to the posterior stroma [115, 135]. The densely intertwined meshwork and the connection between Bowman´s layer and anterior stroma by sutural or bow spring fibers increases the effective elastic modulus in the anterior corneal stroma [134]. The axial heterogeneity in fiber intertwining and mechanical rigidity has important implications for understanding the effects of refractive surgery [134], and will strongly influence intrastromal bubble dynamics and dissection. Although the present study was performed in porcine cornea, it was recently shown that the structure is very similar to human cornea [136].

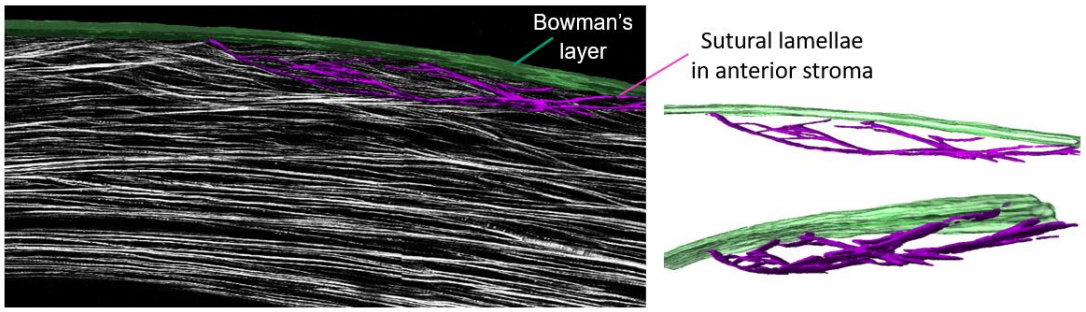

Fig. 3.15. SHG backscatter image of anterior corneal stroma [132].

In the following sections, we will step by step discuss laser-induced bubble formation in water and corneal tissue, followed by the interpretation of single-pulse effects on intrastromal bubble dynamics, and finally the consequences for multiple-pulse effects during dissection.

Bubble size in water and corneal tissue

The study of laser-induced bubble sizes in water and corneal tissue requires knowledge about the underlying processes that finally lead to bubble formation. Water and corneal tissue are largely transparent in the wavelength range between 350 nm and 1050 nm [137, 138]. Hence, energy deposition relies on nonlinear absorption at very high intensities that can be achieved by strong focusing of ultrashort laser pulses [9]. Above the optical breakdown threshold, a high-density free electron plasma is generated that leads to a high temperature and pressure increase and to shock wave emission and a rapidly expanding cavitation bubble [9, 41, 112-114]. In water, the rapid vaporization of the liquid leads to such a fast expansion of the bubble that it expands far above its equilibrium radius and collapses again after reaching its maximum radius, often exhibiting several re-oscillations. In this process, the initial bubble oscillation is almost undamped and bubble expansion and collapse take about the same amount of time. The maximum radius of the laser induced cavitation bubble is closely linked to the bubble oscillation time [139, 140]. The situation in corneal tissue is very different. Here, the laser-induced bubble must work against the restoring forces of the lamellar structure during expansion, and lamellar rupture results in a loss of bubble energy. This means that no symmetrical bubble oscillation as in water is observed; rather, after an initial small overshoot of the radius, the bubble gets stuck and the collapse progresses very slowly. The observed bubble dynamics in porcine cornea in Fig. 3 shows the rapid expansion of the bubble (the maximum radius is reached already after 300 ns) and the very slow bubble collapse lasting for milliseconds. The different dynamics of cavitation bubbles in corneal stroma and water was already investigated by Vogel et. al. for nanosecond and picosecond laser pulses [112], and by Juhasz et. al. for femtosecond laser pulses [113] but the study in this paper was performed at a much higher temporal and spatial resolution. The image sequence from stroboscopic photography in Fig. 4 (a) shows that the bubble size in cornea fluctuates from shot to shot and many of the bubbles have distinct lobes along the lamellar structure. Therefore, the study of the energy dependence of bubble size requires averaging over several events to obtain more accurate conclusions.

The comparison of bubble sizes in water and corneal tissue in Fig. 5 shows that the bubble formation threshold in cornea is lower than in water. If we estimate the bubble thresholds for cornea from the bubble size dependence on laser pulse energy, they are approximately 45 nJ for Gaussian and 140 nJ for vortex beams. This is about 20%-30% below the thresholds for water at 63.2 nJ and 172.1 nJ, respectively. Probably, the biomolecules in cornea provide intermediate energy levels within the bandgap of water leading to more efficient multiphoton ionization, so that the threshold for optical breakdown is slightly reduced compared to water. In previous investigations, researchers stated that the threshold for laser-induced bubble formation is similar for water and ocular media [120, 141], but this result may be due to lower temporal and spatial resolution when determining the thresholds.

With regard to intrastromal dissection, the threshold value for bubble formation is less relevant because it also depends on pulse duration, wavelength, and focusing angle. Instead, the

minimum bubble size that is required for successful flap dissection is crucial for the cutting mechanisms. If we look at the single pulse bubble size at the minimum energy required for successful flap dissection, it amounts to 1 µm for the Gaussian and 0.7 µm for the vortex beam which is surprisingly much smaller than the spot separation of 6 µm in our study. Intrastromal cutting at energies relevant for flap dissection must therefore be related to a dynamic multipulse interaction with a continuous cleavage propagation along the corneal lamellae as we will later discuss in section 4.3. It is also interesting to note that the bubbles at flap cutting threshold have a 3 times smaller volume with the vortex beam than with the Gaussian beam. When the bubbles are smaller at the flap cutting threshold, the cutting mechanisms must be more efficient. While cutting with the Gaussian beam is based on explosive vaporization and large bubbles, cutting with the vortex beam is more a gentle thermoelastic cleavage with less vaporization and smaller bubbles. To completely understand the higher efficacy of the vortex approach, it is required to investigate the interaction of cavitation bubbles with corneal tissue that underlies the cutting process. This will be discussed in the following chapters.

Content of the residual gas bubbles

The large bubbles visible in histology (Figs. 3.12 – 3.14) coalesce from the large number of smaller bubbles produced during laser tissue interaction, whereby the coalescence is driven by surface tension. The bubble interior contains some solid debris, as seen in Fig. 3.13(c). Gas chromatography revealed that the content of the bubble consists mainly of hydrogen and some oxygen [142]. This is somewhat surprising, considering the large collagen content of corneal stroma. An explanation could be that the small volatile gas molecules arise from free-electron-mediated cleavage of side chains from collagen peptide chains, as described in [143, 144], while larger chain fragments form the debris observed in histology. Besides that, dissociation of water in the plasma volume also produces molecular hydrogen [62, 142].

Cavitation bubble dynamics in the layered corneal stroma

Ultra-high-speed photography of the interaction between individual bubbles and corneal lamellae after single laser pulses enabled us to investigate the cavitation bubble dynamics in the layered corneal stroma. Figs. 6 - 8 show image series of the intrastromal bubble dynamics with up to 50 million frames per second. Here, the incoherent illumination under a large focusing angle provides novel insights into the bubble dynamics and its interaction with the lamellar structure. For comparison, Fig. 3.16 shows photographs of intrastromal bubbles from (a) Juhasz et. al. [113] and (b) our work. In the present images, it is clearly visible that the intrastromal bubble is not spherical like assumed previously, rather, the bubble expands along the lamellar structure and forms multiple bubble lobes that are vertically connected by a channel formed by the elongated laser plasma. The length (l) and diameter (d) of the laser focus are given by Abbe`s equations $d = \lambda/\mathrm{NA}$ and $l = 4(\lambda/\mathrm{NA}^2)$ [145]. The ratio l/d is 10.5 for NA = 0.38, which is relevant for clinical systems for flap cutting and was mainly used in our study. The length/diameter ratio of more than 10 illustrates that the laser plasma is not ideally suited for cutting horizontally to the elongated axis, the laser “knife” is oriented in the wrong direction. For $\lambda = 1030$ nm and $\lambda = 355$ nm, the focal length is $l = 28.5$ µm and $l = 9.8$ µm, respectively. Thus, even though the plasma size will be somewhat smaller due to the nonlinearity of the absorption process [9], the plasma length exceeds by far the 2 – 3 µm

thickness of a single corneal lamellae, especially when working above the threshold. Therefore, several overlapping bubble lobes are formed along the elongated plasma, which was now shown by our ultra-high-speed photographic technique. Interestingly, the orientation of the bubble lobes also corresponds to the preferred direction of the lamellae. On the photographs, each layer has an orientation rotated by 90° relative to its upper or lower neighbors, which reflects the structure and organization of collagen within the central corneal stroma [129].

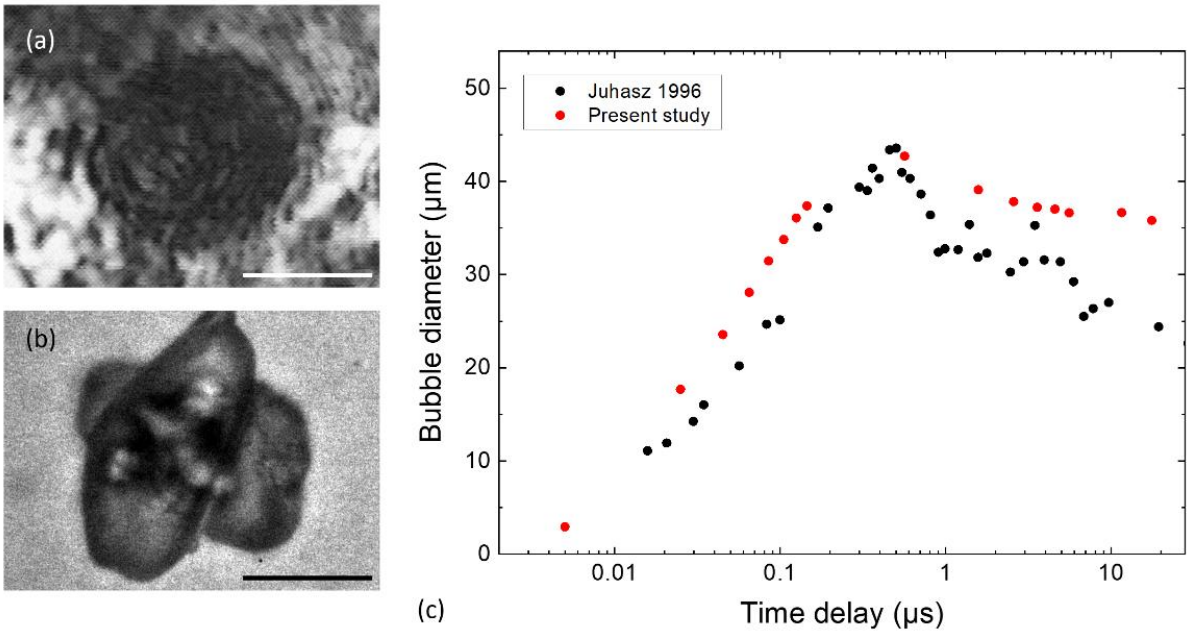

Fig. 3.16. Laser induced cavitation bubble dynamics in corneal stroma. (a) Stroboscopic photograph of bubble formation in bovine cornea (pulse energy 3 µJ, 1 µs delay) by Juhasz et. al. [113] (© 1996 Wiley-Liss, Inc.) showed a dark, spherical bubble and coherent imaging artefacts; (b) Present image of bubble formation in porcine cornea (pulse energy 3 µJ, 1.6 µs delay) enables a view into the bubble revealing several bubble lobes. (c) Bubble size evolution from single-shot ultra-high-speed photographs of intrastromal bubble formation (red dots) in comparison to Juhasz data (black dots) which were obtained from flash photography of several events [113]. Reference bar in the photographs is 20 µm.

The time dependence of the bubble size in the present study in comparison to the data from Juhasz et. al. [113] is shown in Fig. 3.16 (c) on a logarithmic scale. The fundamental sequence of bubble dynamics is similar, but the ultra-high-speed photography now allows the study of the intrastromal bubble interaction with the corneal lamellae in a single-shot technique. It revealed the interaction of the bubble with the corneal lamellae producing a lobular bubble shape. The $R(t)$ curve from [113] exhibits a stronger overshoot at R_{max} than observed in the present paper, where the bubble radius decreases more slowly. A strong overshoot is typical for bubbles in water. In our investigations, all experiments were performed less than 4 h after enucleation. A $R(t)$ curve closer to that of water may be due to a longer storage time of the eyes in saline solution. This could also explain the differences in bubble shape, which was observed to be approximately round in [113].

The results obtained in the first part of the present paper, in which the intrastromal cutting mechanisms was investigated exclusively via the interaction of single laser-induced cavitation bubbles, lead to the suggest that a homogeneous intrastromal cut would require a complete coverage of the entire dissection area with bubbles when the laser pulses are applied in a raster

pattern. Due to the lobed bubble shape, large bubbles are needed to achieve a cut, and the long plasma shape then leads to a relatively thick dissection layer. However, as shown in Fig. 5, the size of individual bubbles at the pulse energy required for intrastromal flap cutting is actually much smaller than the spot separation. This is surprising, especially when considering that cutting in the anterior part of the stroma is difficult due to the intertwining lamellae which are also partially tilted with respect to the cutting plane. The interwoven stromal architecture near Bowman's layer with suture lamellae make this even more difficult. Correspondingly, the histology of intrastromal cuts in Figs. 3.12 – 3.14 show some tissue bridges, where bubbles from neighboring plasmas do not meet, which is also known from clinical flap creation in LASIK [146]. The dissection mechanism is, therefore, much more complex than would be suggested by just looking at individual bubble dynamics.

A first attempt to solve this puzzle was made by Brujan and Vogel in 2006 [101]. They compared the individual bubble dynamics from Juhasz et. al. summarized in Fig. 3.16 (c) with model predictions for spherical bubble dynamics in tissue-like elastic-plastic media. Their fit to the experimental data provided elastic tissue properties for the cornea, namely the elastic modulus E = 144 MPa, the shear modulus G = 48 MPa and the fracture stress Y = 74 MPa. The elastic modulus E of the human cornea under physiological conditions is much smaller, in the range of 0.2 – 0.5 MPa [147-149]. This means that under rapid deformation such as during bubble formation for intrastromal cutting, the cornea stiffens [3, 150] and tearing may become 'cleavage'.

Multiple pulse effects during intrastromal dissection

The individual bubble dynamics and the histology in our study already explains some of the novel observations of the dissection mechanisms. At sufficiently high repetition rate of the laser system, there may be a transition from sequential cavitation-induced cleavage events to crack propagation. This dynamics was explored by high-speed videography with a moving specimen. The repetition rate of 1 kHz is lower than clinical repetition rates due to the use of a translation stage but the videos already provide some valuable insights.

The high-speed videography of multiple pulse effects during intrastromal dissection in Figs. 3.10 and 3.11 showed that the cutting dynamics is based on progressive fracture formation between the lamellar layers of the cornea. The interaction between the laser-induced cavitation bubble, the still existent and slowly collapsing cavitation bubble from the previous pulse, the residual bubble layer in the dissected area, and the lamellar structure of the cornea is highly complex. If the laser pulse energy is too high, the dissection process becomes less efficient, because the laser pulses are focused into already existing bubbles and almost no energy is deposited. Therefore, the energy must be in-between the bubble formation threshold and an energy, at which the subsequent laser pulses will reach corneal tissue, in which a cavitation bubble can be generated. The interaction results in a progressive dissection of the tissue starting from the pre-existing bubble layer, with the cavitation bubble always separating a new section of the tissue in the direction along the cutting movement. Each bubble expansion advances the crack propagation in the stroma along the bubble lobes. The tip part of the crack closes again in the millisecond time interval between subsequent laser pulses (Figs. 3.10 and 3.11) but one already sees a continuous movement of the bubble front resembling crack propagation in the

videos taken at 1 kHz. At higher repetition rates, it may occur also at the lower pulse energies employed in femtosecond laser based corneal dissection (see section 5). The consecutive expansion of bubbles generated along the laser beam track can drive crack propagation if the front bubble has already expanded to a certain size but not yet reached its maximum size or started to collapse, when the next pulse is released. Such crack propagation driven by sequential bubble formation may lower the pulse energy required for dissection. This hypothesis is supported by the fact that a higher efficiency in flap cutting and reduced side effects were observed when the repetition rate of clinical devices from Intralase was increased from 15 kHz to 60 kHz, and 150 kHz, respectively [109, 151].

Crack dynamics in solids and in intrastromal dissection

The energetics and speed of crack propagation in solids can be described using the Griffith theory [11, 152] that is well presented in a book by J. E. Gordon [153]. It's applicability is supported by the fact that cornea has strain-stiffening features, i.e. it's elastic modulus strongly increases during deformations at high strain rate as occurring in laser dissection [3]. In his seminal paper published in 1921, Griffith experimentally and theoretically investigated cracks and rupture in fragile solids like glass [152]. Later, this model was extended by Orowan et. al. to elastic plastic materials [154], and in 1948 the work has been extended and systematized to form the science of fracture mechanics [155, 156]. Often this work was performed to determine practical criteria to estimate the fracture toughness, which is the resistance of a material to the propagation of cracks [157]. In fracture mechanics, the stress field around a crack must be determined when external forces are subjected to the material. These forces induce a complicated system of stresses in its interior, but the stresses are particularly large near the end of the crack. Hence, for most purposes it is enough to know the stress field near the tip of the crack which can be described by stress intensity factors [156, 158]. In the work from Eshelby, crack formation of *mode I deformation* was defined as a crack that opens up by tension transvers to its length. This type of deformation corresponds quite well to the behavior of a cavitation bubble created at the end of an existing crack in an intrastromal cut between corneal lamellae as schematically shown in Fig. 3.17.

The elastic field near the crack tip can be calculated to determine the threshold for crack propagation. It is reasonable that the tip of the crack is pulled apart by the underlying forces, and held together by the cohesive forces acting between the faces inside the tip [159]. Barenblatt assumed that for small loads the cohesive forces are able to compensate the external forces, but at a critical threshold value, this equilibrium is suddenly broken, so that a stress-singularity develops and the crack begins to extend [159]. Such crack dynamics induced by repetitive formation of intrastromal cavitation bubbles may significantly contribute to intrastromal dissection. Subsidiary cracks propagating under oblique angles as visible in Fig. 3.14(c) may appear, when subsidiary stress maxima are formed at a small distance to the crack tip ('Cook Gordon effect' described in Refs. [153, 160]).

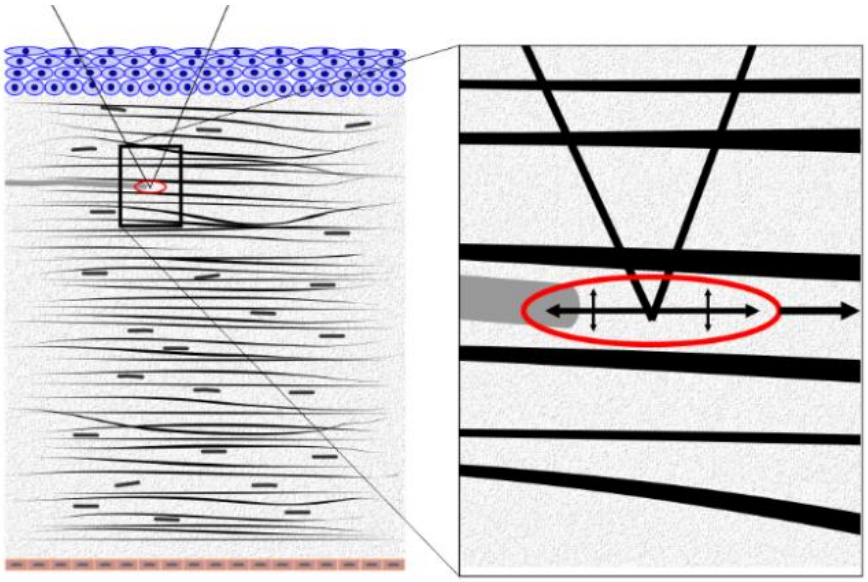

Fig. 3.17. Schematic drawing of laser induced cavitation bubble formation that induces crack formation along the corneal lamellae as fundamental cutting mechanism in intrastromal dissection.

An argument against the above considerations on crack propagation is that Griffith`s theory was developed for brittle fracture in solids driven by a continuously applied force. Here, the decrease of elastic and potential energy must be equal to or exceed the surface energy of the freshly formed crack as a condition for energy release and crack propagation [152]. However, in corneal laser dissection, energy and force are applied in short pulses, and the material is viscoelastic rather than brittle and consists of fibril bundles organized as lamellae. This constellation is similar to the many wires in the carrying rope of a suspension bridge, where crack propagation is stopped at the border of each wire.

Doubts about the essential role of crack propagation for corneal dissection are supported by the mode of corneal dissection used in the Zeiss Visumax refractive laser system. Here, the dissection pulses are applied in a spiral pattern starting in the corneal center. To maintain a constant spot separation, cutting starts with < 1 kHz pulse repetition rate in the corneal center (the slow speed is due to the inertia of the scanning mirrors) but the repetition rate reaches 2 MHz in the middle part and the periphery of the spiral pattern. In spite of the change of pulse repetition rate, cutting can be performed with constant pulse energy. This suggests that cutting essentially consists on an ‘incoherent’ addition of individual cleavage effects from the laser-induced breakdown events, which are strong enough for local rupture of collagen fibrils. This is particularly true if the collagen lamellae are oriented under an angle with the desired cutting direction. Nevertheless, crack propagation may play a role as a cause of tissue bridge formation. Most likely, crack-propagation between corneal lamellae and within lamellae in the direction of the collagen fibrils requires less energy and force than fibril rupture. Therefore, it can deviate the cleavage direction from the desired cutting direction, as shown in Fig. 3.13 (b).

How can these considerations be reconciled with the changes of required cutting energy that were observed, when the repetition rate of clinical devices from Intralase was increased from 15 kHz to 60 kHz, and 150 kHz, respectively [109, 151]? One possible explanation is that the beam quality of the laser and the quality of the optical delivery system was improved from the

very first pioneering Intralase system to later generations. The improvement of dissection would then be due to improvements of focus quality rather than to the change in repetition rate.

To resolve the open questions, it will be necessary to perform high-speed photographic investigations at pulse repetition rates and with pulse energies similar to those employed in clinical systems. This is a very challenging task because it involves the use of scanned laser beams and imaging of a large field at high spatial resolution.

3.5 Conclusions on dissection mechanisms

In this section, the mechanisms of corneal intrastromal laser dissection were investigated by stroboscopic photography, ultra-high-speed photography at up to 50 million frames per second, and videography. The unprecedented spatial and temporal resolution enabled to look inside the intrastromal bubble and to visualize the interaction with the corneal lamellae. It turned out that the bubble dynamics in corneal tissue is much more complex than in water. The laser-induced bubbles exist longer in tissue and the bubbles are not spherical but multiple bubble lobes evolve from the elongated laser plasma. They expand into the 2 - 3 µm thick corneal lamellae along the collagen fibrils. The multitude of bubble lobes can contribute to cleavage of the stroma but also result in tissue bridges if cleavages originating from neighboring bubbles do not overlap.

Intrastromal cutting relies on a progressive laser-driven propagation of the bubble layer from an already dissected region into a new section of the tissue, with the cavitation bubble separating tissue layers in scanning direction. Each bubble expansion advances cleavages or cracks along the bubble lobes. An optimization of cleavage overlap from neighboring breakdown events is the key for a gentle, precise and efficient intrastromal dissection. It will be shown in the next section that a vortex beam, which has a larger focal diameter but the same length as Gaussian beam, produces a favorable force distribution for smooth cleavage in cutting direction. This way, precision is increased and unwanted tissue bridges are reduced. A similar effect can be achieved by reducing the plasma length through the use of a high NA or a shorter laser wavelength, as will be shown in section 5. In addition, a high repetition rate in combination with a small spot separation may contribute to smoother cuts, especially if crack propagation according to the Griffith mechanism is involved in cutting.

4. Vortex beam for gentle and precise dissection

4.1. Motivation and objectives

Despite of more than 20 years of experience with LASIK and SmILE, there is still room for improvements of efficiency, precision, and safety. Significant improvements can be achieved by addressing the key-step of the refractive laser procedure: intrastromal dissection. In most clinical systems, IR fs laser pulses with pulse energies between 0.3 µJ and 1.6 µJ are focused into the corneal stroma at a numerical aperture NA 0.3 – 0.4 in a raster pattern with 3 – 6.5 µm spot separation [111]. Dissection is here based on laser-induced plasma formation followed by a rapidly expanding shock wave and cavitation bubble [9, 10, 41, 112, 113]. The creation of an intrastromal cut relies partly on tissue vaporization but mainly on the thermo-mechanical interaction of the plasma shock wave and cavitation bubble with the layered corneal tissue that leads to a cleavage of corneal lamellae [4, 41].

However, cutting precision is compromised by the elongated shape of the laser plasma, which is oriented along the optical axis, perpendicular to the desired cutting direction. The diameter d and length l of the elongated focus are given by Abbe's equations $d = \lambda/NA$ and $l = 4\ (\lambda/NA^2)$ [145], and the ratio l/d for parameters used in clinical systems for flap cutting is approximately 10.5. To improve the dissection process, it would be ideal to be able to rotate the "laser knife" such that the blade is oriented in cutting direction as shown schematically in Figs. 2.8 (a) and (c) (section 2.4). Unfortunately, the fundamental laws of optics do not allow this but one can try to get as close as possible towards that simple concept.

In this section, a novel concept of focus shaping for gentle and ultraprecise intrastromal dissection in refractive surgery is introduced, which is based on the idea presented in Figs. 2.8 and 2.10. A spiral phase plate with phase shift of 2π is used to convert the Gaussian beam into a helically phased vortex beam. The helical phase results in destructive interference at the center, where the phase difference between beam parts from opposite sides of the beam is always π, i.e. half of the wavelength of light. This feature is propagation invariant and the laser focus has, therefore, a ring shape. The focus length in axial direction remains the same as for the Gaussian beam but the diameter is two times larger [104].The larger aspect ratio between plasma diameter and length facilitates cleavage along the corneal lamellae and enables dissection with lower plasma energy density and less bubble formation that result in smoother cuts [12]. A detailed analysis of the underlying laser tissue interactions shows that this goes along with a significant reduction of mechanical side effects. Gentler dissection and reduced intrastromal deformation by residual bubbles may improve the safety and precision of both LASIK and SmILE.

4.2. Methods

Experiments are performed in ex-vivo porcine eyes. Flap cutting is taken as an example for an intrastromal dissection procedure that is relevant both for LASIK and SmILE because here the dissection quality can be readily assessed by evaluating the ease of flap lifting. In a first step, the energy required for flap cutting is determined for IR Gaussian and vortex beams. Pulse durations are varied from 480 fs to 9 ps to compare the influence of pulse length on cutting energy and precision for the novel approach (vortex beam) in comparison the established

technique (Gaussian beam). Secondly, the cutting quality is characterized by microscopic imaging and scanning electron microscopy. Finally, transmission measurements during flap cutting are employed to demonstrate that the plasma energy density can be significantly reduced by focus shaping.

Cornea Specimens

The study was performed on ex-vivo corneas obtained from fresh (<4 h postmortem) porcine eyes. After enucleation, the eyes were stored at 8°C in nutrient solution (Dulbecco´s Modified Eagle´s Medium, low glucose, Sigma-Aldrich, Co.). Immediately before the experiment, the epithelial layer of the cornea was removed, the cornea was excised by a cut close to the corneal limbus, and an 8 mm biopsy punch (KAI Medical, BP-80F) was used for preparing the circular specimen. Then, the cornea specimen was transferred into a custom-designed holder with exchangeable cover glasses on the front and back sides that flattened the cornea during dissection.

Laser system and beam delivery

A fiber-laser-based chirped pulse amplification system with 1030 nm wavelength and a tunable pulse duration was used for dissection of the corneal flap (Cazadero, CALMAR LASER, INC.). Pulse durations were 480 fs, 3 ps, and 8.8 ps. The beam quality parameter of the fiber laser system is specified by the manufacturer to $M^2 < 1.2$. The laser pulse shape and laser pulse duration were characterized by use of an autocorrelator (PulseCheck, APE, Berlin, Germany). A schematic drawing of the experimental setup is shown in Fig. 4.1.

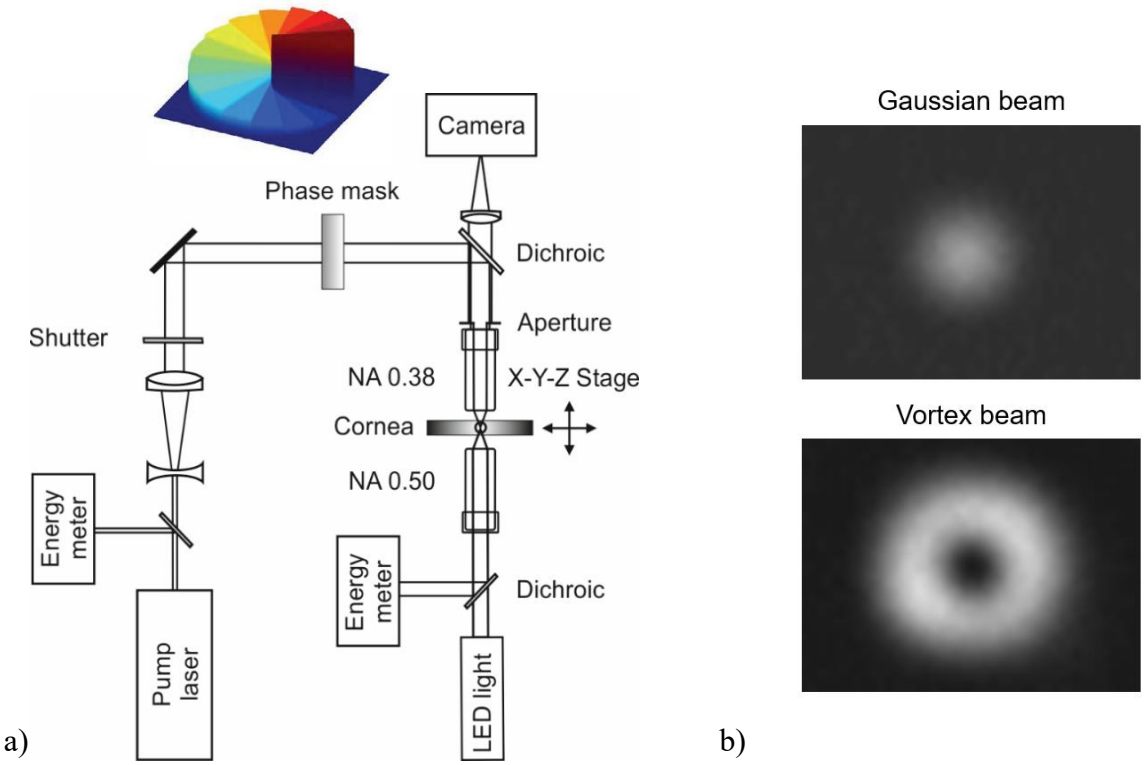

Fig. 4.1. (a) Experimental setup for the investigation of intrastromal laser dissection. (b) Measured focal light distributions with the original Gaussian beam and after insertion of the spiral phase mask creating a vortex beam.

To convert the linear polarized Gaussian (G) beam into a helically phased Laguerre-Gaussian (LG) vortex beam, a fused-silica spiral phase plate with maximum phase shift $\Delta\varphi = 2\,\pi$ (VL-209-I-Y-A, vortex grade A, HOLO/OR Ltd., Ness Ziona, Israel) was inserted into the beam path. Because the phase plate is produced by etching, it consists of 16 segments with stepwise increasing $\Delta\varphi$. By passing the phase plate, the laser beam is converted into a Laguerre-Gaussian vortex beam of order m = 1. The focus has a ring shape, with the same length in the axial direction as the focus of the Gaussian beam, but two times larger diameter as shown in Fig. 2.10 (see section 2.4) [161] [104].

Laser pulses with Gaussian and Laguerre-Gaussian shapes were focused through a microscope objective (Zeiss, LD Plan Neofluar, 63x, NA 0.75) into the cornea. The numerical aperture (NA) was reduced to 0.38 by means of an aperture in the rear entrance pupil to mimic focusing conditions in clinical flap and lenticule dissection. Assuming $M^2 = 1.1$, the corresponding focus diameters are $d_{\mathrm{Gauss}} = 3.0$ µm for the clipped Gaussian beam, and $d_{\mathrm{ring}} = 6.0$ µm for the vortex beam (factor 2) [145, 161]. Pulses were applied in a raster pattern with 6-µm spot separation. For this purpose, the laser was run at 5 kHz repetition rate and the porcine cornea was continuously moved by means of a three-dimensional translation stage at 30 mm/s translation velocity adjusted to the repetition rate. The flap bed was cut at 150 µm depth within a circular area of 6 mm in diameter. The side cut for opening the flap was made by stepwise moving the laser focus in a circular arc of 345°, with 2 µm vertical separation between the lines. A part of the circle (15°) was left out from cutting to produce a hinge for folding the flap.

Imaging of corneal dissections

The cutting plane was imaged onto a CMOS camera (Nikon D5100) through a combination of the Zeiss microscope objective used for focusing the laser pulses into the corneal stroma with a tube lens (Zeiss). The dissection zone was illuminated through a second microscope objective (Zeiss, Plan Neofluar 20x, NA 0.5) with light from a white LED placed below the cornea holder. Immediately (< 1min) after cutting the flap, photographs of the cutting area were taken to determine the amount of gas bubble formation during the dissection process. In addition, an overview picture of the entire cornea after flap cutting and removing the cornea holder from the stage was photographed using a stereo microscope (Zeiss Op Mi-1) and a digital camera (Canon LEGRIA HF R18).

Determination of laser pulse energy required for flap cutting

The laser pulse energy at the laser focus was measured during each cut using an Ophir PD 10 energy meter. It was pre-calibrated without microscope objective behind the aperture and considering the transmittance T of the Zeiss objective at 1030 nm (T = 40 %). To determine the laser pulse energy required for flap cutting, the pulse energy was in a first step adjusted to a level at which bubble formation in the corneal stroma became visible. The side cut was always performed at higher pulse energies to ensure a smooth cut. After flap cutting, the specimen was removed from the holder and the flap was opened by an experienced surgeon using a hockey knife. The quality of the dissection was judged subjectively and classified into one of the three categories “no flap lifting”, “hard flap lifting”, or “easy flap lifting”. Depending on this classification, the laser pulse energy was then either increased or decreased to determine the

minimum value required for easy flap lifting. This procedure was, at every laser pulse duration, repeated in ten different corneas both for the Gaussian and the vortex beam (total number of investigated corneas: n = 60).

The irradiance threshold for plasma formation (also called laser induced breakdown threshold) is known to be similar for water and ocular media [141, 162]. Therefore, we use the threshold for plasma-induced bubble formation in water as a bench mark to assess the strength of mechanical effects in corneal dissection. A larger ratio between flap cutting threshold and bubble threshold will imply more vigorous mechanical effects. Bubble thresholds in water at NA = 0.4 were determined in a different setup using a scattering technique described previously [7, 53, 119].

Characterization of cutting quality

After successful flap dissection and lifting, the corneal specimens were fixated for 48 hours in fixing solution following the protocol of Grazadei et. al. [124]. Then the cornea was prepared for scanning electron microscopy (SEM, Philips REM 505) by critical point drying and gold sputtering. The intrastromal cutting quality was characterized by the SEM images of the flap beds. The surface roughness in the SEM images was assessed using software designed for roughness analysis ("SurfChar" plugin according to ISO 25178 standard, ImageJ, National Institutes of Health and the Laboratory for Optical and Computational Instrumentation, University of Wisconsin) [163]. The software was originally designed to evaluate topographical information obtained through stereo-SEM, where picture pairs are taken under different angles. However, it is useful also for the analysis of individual SEM pictures [164]. Brightness contrast in SEM relies on the fact that the secondary electrons are detected under an oblique angle such that height variations are transformed into brightness variations [145]. Analysis of the local brightness fluctuations thus provides information on the roughness but in arbitrary units (a.u.) rather than on an absolute length scale.

Determination of absorbed laser energy

For determining the laser pulse energy absorbed during intrastromal cutting, the transmitted laser light was collected with a second microscope objective (Zeiss, NA 0.5) that was confocally and collinearly aligned to the focusing objective (NA 0.38). The larger NA of the second objective ensured that also forward scattered light was collected. The transmitted laser light was reflected by a dichroic mirror onto an energy meter (either Ophir PE10 or PD10, depending on transmitted energy). To account for light losses by reflections at optical surfaces and absorption in the cornea, the energy meter behind the cornea was calibrated against the reference energy meter in the initial beam path (Fig. 4.1) and it was assumed that well below the energy required for flap cutting 100 % of the incident light is transmitted through the laser focus. The incident laser pulse energy was stepwise increased from sub threshold values to higher energies leading to strong bubble formation. A large spot distance of 250 x 200 µm in the raster pattern was used to avoid interactions with larger bubbles from previous laser pulses at large pulse energies well above the bubble threshold. For this purpose, the velocity of the translation stage was reduced to 1 mm/s at a low laser repetition rate of 4 Hz. The absorbed energy, E_{abs}, was calculated from the measured values of incident energy, E_{in}, and transmitted energy, E_T, by $E_{abs} = E_{in} - E_T$.

4.3. Results

Laser pulse energy required for intrastromal flap cutting

Figure 4.2 summarizes the results of the measurement series performed to determine the laser pulse energy required for intrastromal flap with Gaussian and vortex beams at different pulse durations.

At all investigated pulse durations, the pulse energies required for flap cutting are a factor of 1.6 to 1.8 higher with the larger ring focus of the vortex beam than with the Gaussian beam. The threshold energy for flap cutting, $E_{th,cut}$, decreases significantly with decreasing pulse duration. For Gaussian beams it drops from 759 nJ at 8.8 ps to 187 nJ at 480 fs, and for vortex beams it decreases from 1.4 µJ at 8.8 ps to 303 nJ at 480 fs. The highest cutting quality with least disruptive side effects is expected at the lowest $E_{th,cut}$ values. Therefore, a detailed characterization of the cutting quality was performed for the pulse duration of 480 fs.

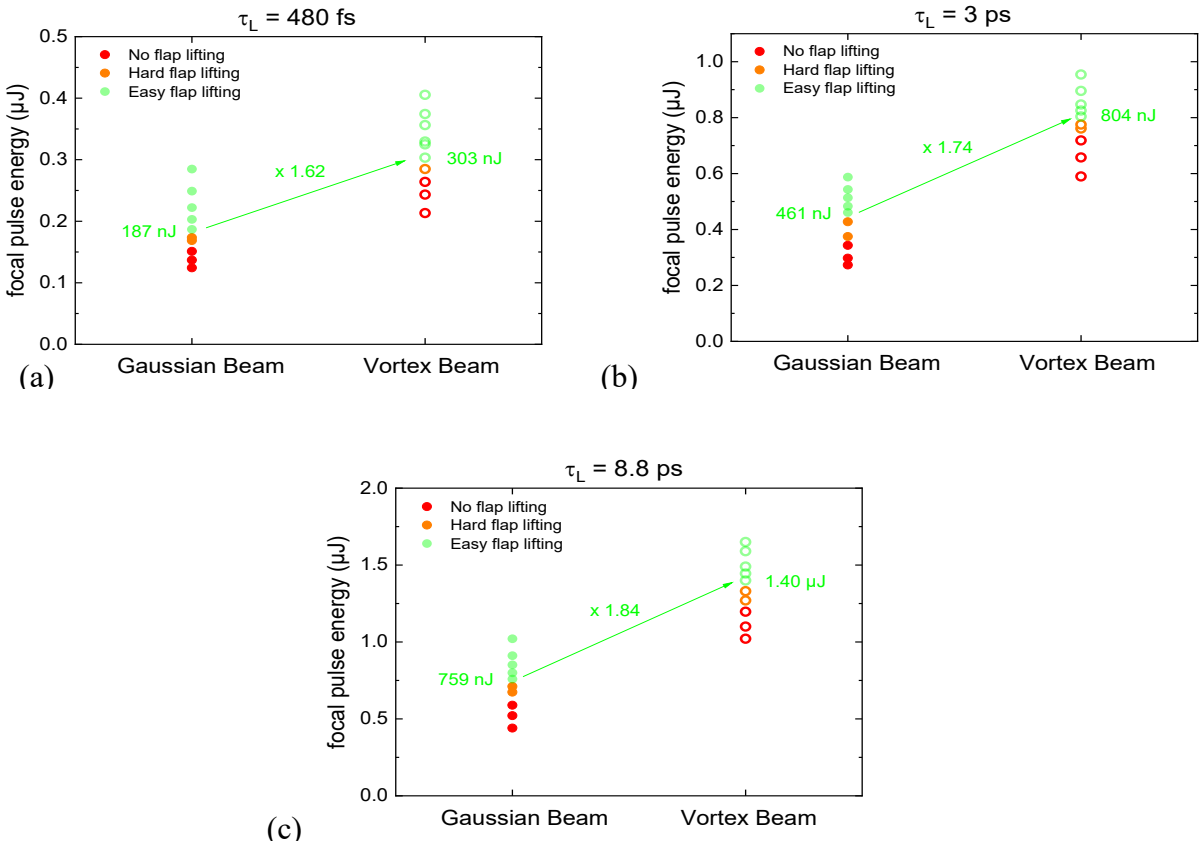

Fig. 4.2. Classification of flap cuts at different laser pulse energies for Gaussian (dots) and vortex (circles) beams at (**a**) 480 fs, (**b**) 3 ps, and (**c**) 8.8 ps laser pulse duration. Cutting attempts where "no flap lifting" was possible are marked in red, "hard flap lifting" in orange, and "easy flap lifting" in green. For each measurement series, the lowest energy value for which easy flap lifting could be achieved is indicated next to the corresponding data point.

Scanning electron microscopic images

Figure 4.3 shows representative SEM images of the flap beds in porcine corneas produced with 480-fs pulses at energies slightly above $E_{th,cut}$. At low magnification (Fig. 4.3a), the entire flap bed and a part of the flap are clearly visible. The edge of the flap bed shows some imperfections due to the higher laser pulse energy used for the side cut. The quality of the flap cuts can be determined by the surface roughness of the flap beds, visible at higher magnification (Figs. 4.3b and c). For the vortex beam, the flap bed is much smoother, with fewer irregularities along the lamellar structure of the cornea, than for the Gaussian beam. Average surface roughness is characterized by the arithmetic mean height deviation S_a, which amounts to 14.90 (a.u.) vs 9.97 (a.u.) for Gaussian and vortex beams in Fig. 4.3b, and 29.25 (a.u.) vs 18.31 (a.u.) in Fig. 4.3c, respectively.

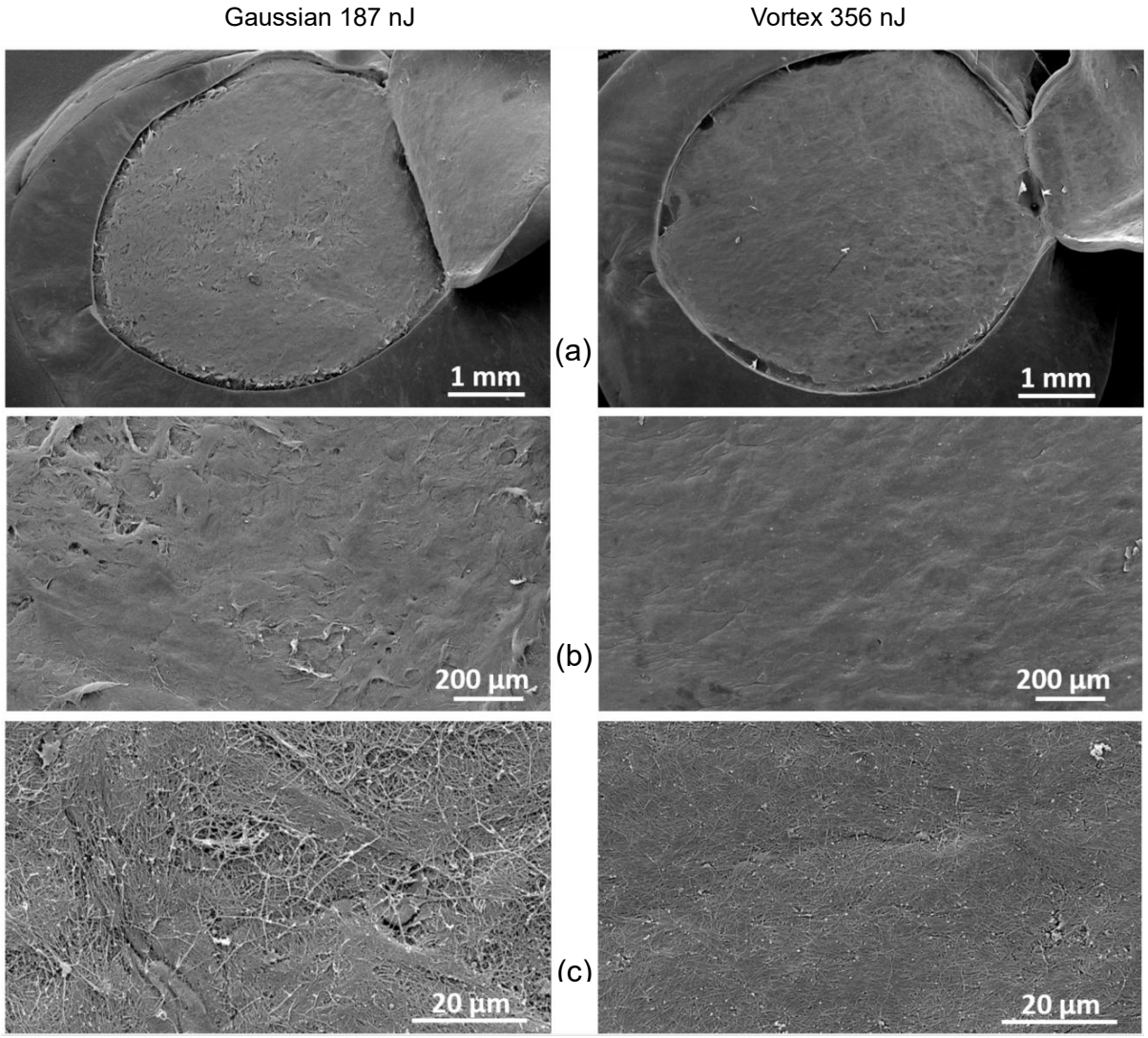

Fig. 4.3. Scanning electron microscopic images of 6-mm flaps in porcine cornea that were cut using Gaussian (left column) and vortex (right column) beams with 1030 nm wavelength and 480 fs laser pulse duration. Pulse energies were slightly above the threshold for easy flap lifting.

Bubble layer after flap cutting

Figure 4.4 shows the bubble layer after flap cutting with 480 fs, 1030 nm laser pulses, applied at 6 x 6 µm spot separation. Hardly any gas bubble formation is observed with the vortex beam, although the flap could be easily lifted. At high magnification, only the raster pattern of the laser foci is visible. By contrast, the Gaussian pulses produced a dense bubble layer. Already 1 min after dissection small bubbles have coalesced. Therefore, individual bubbles are visible also at low magnification under the stereo microscope.

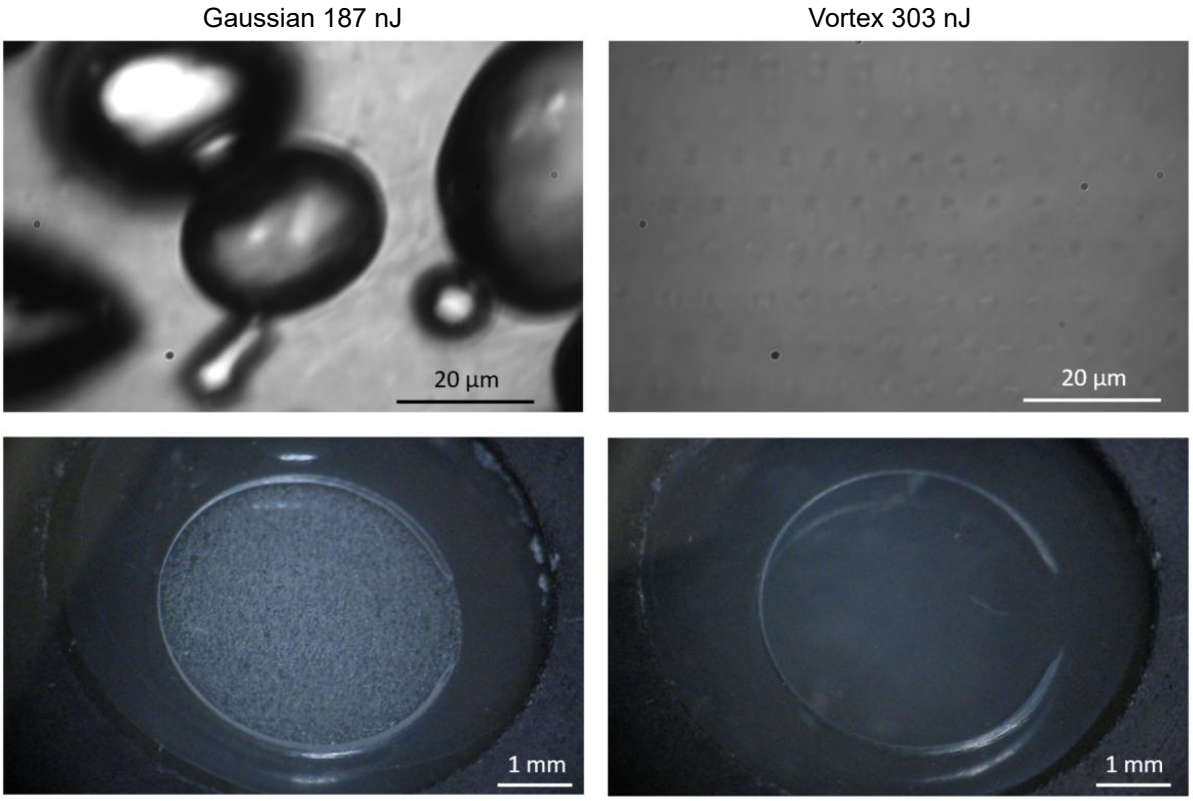

Fig. 4.4. Photographs of the laser-induced gas bubble layer after flap dissection with Gaussian (left column) and vortex (right column) beams with 1030 nm wavelength and 480 fs laser pulse duration. Photographs in the upper row were taken through the focusing objective less than 1min after flap cutting. Photographs in the lower row were taken 10 mins after flap cutting using a stereo microscope.

Dissection thresholds in comparison to bubble thresholds in water

Figure 4.5 shows the thresholds for flap cutting in cornea in comparison to bubble thresholds in water for Gaussian and vortex beams of different pulse durations. For the Gaussian beam, the energy required for flap cutting is always significantly higher than the bubble threshold in water (+76 % at 480 fs, +56 % at 3 ps, and +48 % at 8.8 ps). In contrast, the vortex beam cuts already with energies very close to the bubble threshold (+1.0 % at 480 fs, +8.6 % at 3 ps, and +2.9 % at 8.8 ps).

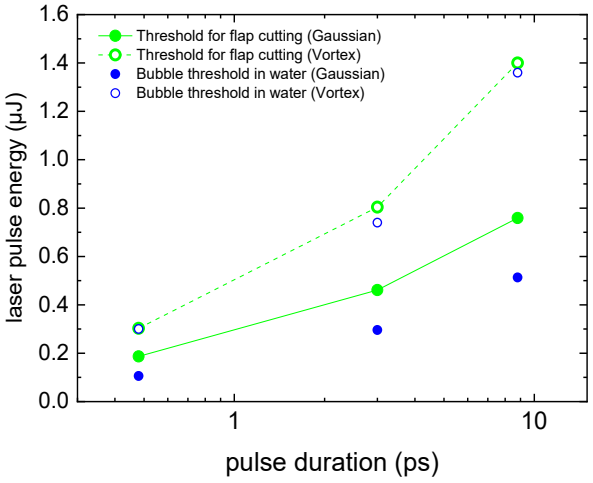

Fig. 4.5. Thresholds for flap cutting (green) and bubble formation in water (blue) for Gaussian (dots) and vortex (circles) beams at 1030 nm wavelength and 480 fs, 3 ps, and 8.8 ps pulse duration. Numerical apertures were NA = 0.38 in cornea, and NA = 0.4 in water.

Absorbed laser energy during intrastromal flap cutting

Figure 4.6 shows the laser energy transmission during intrastromal cutting in dependence on the incident laser pulse energy, and Fig. 4.7 presents the absorbed energy at $E_{th,cut}$. Below the threshold for visible bubble formation in cornea, the transmission through the porcine cornea stays constant at 100 percent. After bubble formations sets in, the transmission decreases with increasing laser pulse energy, because ever more laser energy is absorbed and converted into mechanical energy of bubbles and acoustic transients. At $E_{th,cut}$, the transmission for the Gaussian beam is 72.2 % at 480 fs, 64.0 % at 3 ps, and 62.5 % at 8.8 ps, corresponding to absorbed energy fractions of 27.8 %, 36.0 %, and 37.5 %. For the vortex beam, the energy for flap cutting is higher than for the Gaussian beam, but the percentage of absorbed energy is much lower. We found transmission values of 98.0 % at 480 fs, 93.5 % at 3 ps, and 86.0 % at 8.8 ps, corresponding to absorbed fractions of only 2.0 %, 6.5 %, and 14 %.

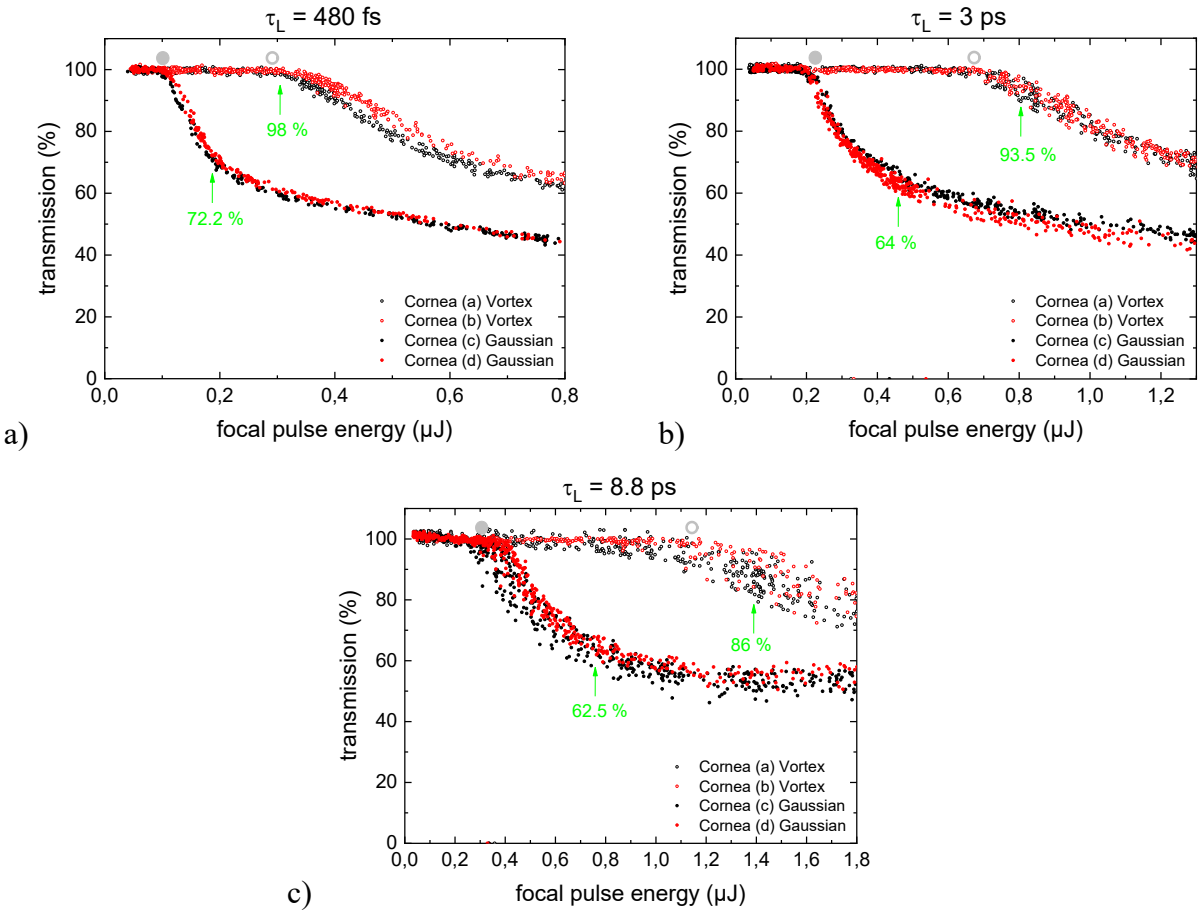

Fig. 4.6. Laser energy transmission during intrastromal flap cutting for Gaussian and vortex beams at (**a**) 480 fs, (**b**) 3 ps, and (**c**) 8.8 ps laser pulse duration. For each parameter set, two different porcine corneas were investigated (red and black dots). The thresholds for visible bubble formation in cornea are shown as grey dots (Gaussian) and grey circles (vortex). The energy values required for flap cutting are marked with green arrows and the corresponding transmission values are indicated.

Figure 4.7 shows that also the absolute values for E_{abs} are lower for the vortex beam. The difference becomes larger with decreasing pulse duration, and at 480 fs, the absorbed energy values are 6 nJ for the vortex beam versus 52 nJ for the Gaussian beam.

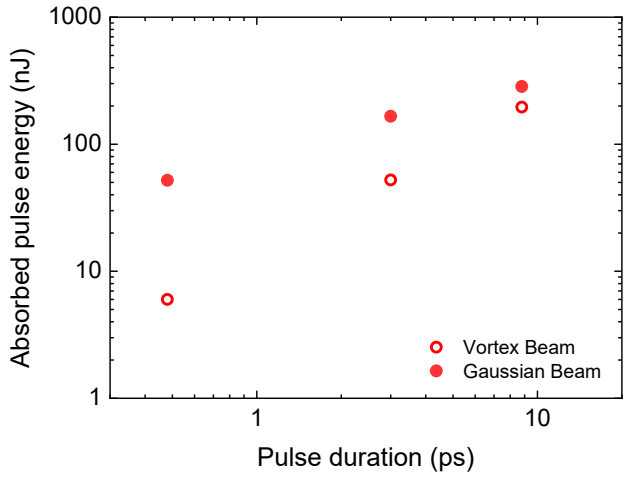

Fig. 4.7. Absorbed laser pulse energy at $E_{th,cut}$ during flap cutting with Gaussian (dots) and vortex beam (circles).

4.4 Discussion

Cutting efficiency and precision

The results show that focus shaping using vortex laser beams is a promising approach for gentle and ultraprecise intrastromal flap cutting in refractive surgery. Dissection of the transparent cornea is based on plasma formation by nonlinear energy deposition [4, 9, 165]. Scanning of the corneal stroma in a raster pattern at the same cutting depth produces many individual micro-explosions and cavitation bubbles, and their combined action finally leads to a cleavage plane. Tissue bridges arise where bubbles from neighboring plasmas do not meet. At equal spot distance within the 6 µm raster patter, the part of the cleave plane covered by laser plasmas is larger for the vortex beam than for the Gaussian beam, and the reduced distance between the periphery of individual plasmas makes it easier that cleavage lines from neighboring foci meet [12]. This reduces the number of tissue bridges arising from collagen fiber branching in the anterior cornea [134], enhances the cutting efficiency and improves the smoothness and precision of the cut (Fig. 4). While many researchers use a scoring system to support the subjective assessment of the surface properties of intrastromal dissections [36, 166, 167], we followed the approach by Sarayba et al. (2007), who employed specialized software designed for roughness analysis [164]. The results of the automated methodology confirmed the subjective impression gained from the SEM images, which favors cuts by the vortex beam.

For all investigated pulse durations, the incident energy E_{in} required for flap cutting was larger for the vortex beam than for the Gaussian beam (Fig. 4.2) because LIOB is an irradiance dependent process and the area of the ring-shaped focus is 4 times larger than the Gaussian focus. However, the real parameter governing both the efficiency and disruptiveness of dissection is the absorbed energy E_{abs} rather than E_{in}. The value of this parameter was dramatically reduced by use of the ring shaped focus (Fig. 4.6). At 480 fs pulse duration, E_{abs} at the flap cutting threshold is only 6 nJ energy per pulse with the vortex beam but 52 nJ (8.7 times higher) for the Gaussian beam.

For a better assessment of the cutting efficiency, the energy needed to mechanically separate corneal lamellae is compared with the energy required for corneal dissection at different irradiation parameters. Smolek and McCarey determined the tearing force required to separate corneal lamellae at 50 % stromal depth in 16 human eye bank corneas [168]. Traction was applied perpendicular to the orientation of the lamellae, which minimizes the tearing work. The mean force needed for the separation of a 1 cm wide stripe was 0.142 kp = 1.39 N. The corresponding tearing work for a stripe of 1 cm length is $1.39 \cdot 10^{-2}$ J, and the separation energy per unit area is $E_{sep} = 1.39 \cdot 10^{-2}$ J/cm². In the present study, 6 nJ deposited energy per laser pulse was necessary for flap cutting with the vortex beam at 480 fs pulse duration and 6 µm × 6 µm spot separation. The corresponding energy per unit area is $E_{Flap,vortex} = 1.67 \cdot 10^{-2}$ J/cm², just 20 % above the separation energy by tearing. Hence, corneal dissection using a vortex beam and appropriate spot separation is energetically close to the possible optimum achievable with mechanical tearing. With a Gaussian beam, the deposited energy per unit area required for flap dissection is $E_{Flap,Gaussian} = 14.5 \cdot 10^{-2}$ J/cm² and therefore 10.4 times larger than for mechanical tearing, which is much less efficient than flap cutting using the vortex approach and may cause more disruption and mechanical side effects.

Mechanical side effects

Cutting energies are always well above the bubble threshold with Gaussian beams but close to the bubble threshold with vortex beams (Figs. 4.4 and 4.5). This suggests that not only E_{abs} but also the plasma energy density is significantly lower for vortex beams. For ultrashort laser pulses, energy deposition is stress-confined and thermos-elastic stress lowers the bubble threshold well below the superheat limit [3, 9]. This way, the ring shaped focus of the vortex beam facilitates cleavage along the corneal lamellae to such a degree that an explosive vaporization is not necessary for dissection but the thermoelastic stress produced at the bubble threshold is sufficient. As a consequence, cutting is less disruptive and mechanical side effects will be smaller.

In the following, the mechanical stress on keratocytes close to the cut and on epithelial cells in approximately 100 µm distance from the dissection plane (as often used clinically) is assessed for the shortest investigated pulse duration, 480 fs, which produced the smoothest cuts with least energy. For fs breakdown at the bubble threshold, Vogel and coworkers obtained a theoretical prediction of 42 MPa for the amplitude of the thermos-elastic stress wave at the plasma rim, and experimental values between 56 MPa and 61 MPa by back-extrapolation of far-field hydrophone measurements [9]. With a vortex beam, flap dissections are performed very close to the bubble threshold (Figs. 4.5 and 4.6), and one can thus assume peak pressures of about 50 MPa in immediate vicinity of the cut. The pressure decays with a scaling law $p \propto r^n$ with $n = 1.12$ [9, 10], which results in a pressure of 0.57 MPa at 100 µm distance, considering a plasma radius of 1.83 µm that is smaller than the ring focus radius of 3.0 µm because of the 6^{th} order multiphoton ionization process involved in the plasma formation process [9].

With a Gaussian beam of 480-fs pulses, the pressure at the plasma rim will be much higher. The incident energy required for flap cutting is 76 % larger than the bubble threshold $E_{th,bubble}$ (section 4.3) but the absorbed energy is even 8.7 times larger than for the vortex beam. The ratio of plasma energy densities U depends on the ratio of absorbed energies and on the respective plasma volumes. The focal diameter is smaller for the Gaussian beam but the plasma length at $1.76 \times E_{th,bubble}$ will be larger than for flap cutting with the vortex beam occurring close to $E_{th,bubble}$. Since a precise quantification of the plasma volumes is difficult; one roughly estimates a plasma energy density ratio $U_{Gaussian}/U_{vortex} = 10 - 15$. Energy deposition in femtosecond breakdown is isochoric [9] (i.e. volume and mass density remain constant during heating) and the relations between internal energy, temperature, and pressure are unambiguously determined by the equation of state (EOS) of the material. Since tissue consists mostly of water, the IAPWS-95 formulation of the water EOS [169] is used to determine the peak plasma pressure for the Gaussian beam at the flap cutting threshold (Fig. 4.8 b).

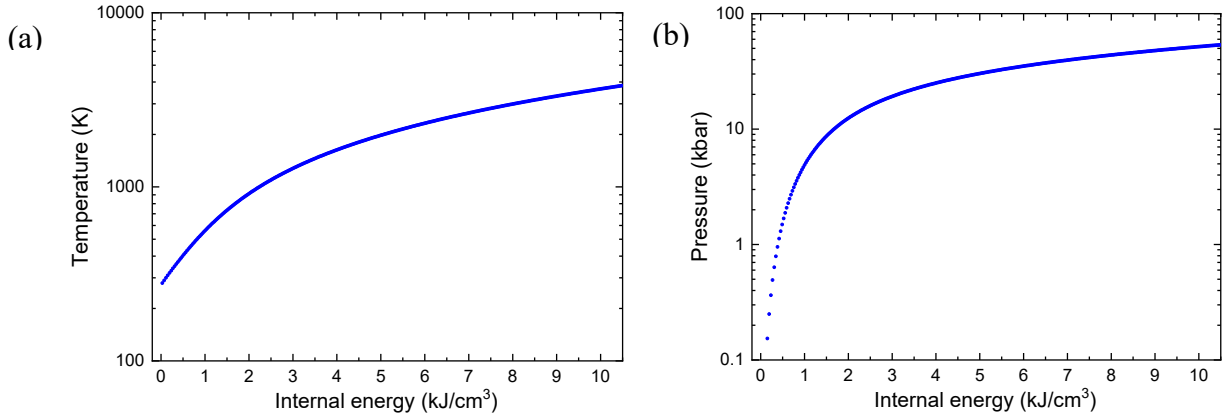

Fig. 4.8. Temperature (**a**) and pressure (**b**) as a function of internal energy for a mass density ρ_0 = 1000 kg m^{-3}, according to the IAPWS-95 formulation of the equation of state of water.[169]

The calculation is based on the finding from Vogel et. al. [9] that at the bubble threshold the temperature at the focus center rises by 131.5°C, corresponding to an internal energy gain of 0.50 kJ/cm³. It is assumed that the same holds for the bubble and flap cutting threshold of the vortex beam. A 10 - 15 times larger jump in internal energy of 5.0 - 7.5 kJ/cm³ with the Gaussian beam will result in peak temperatures of 2000 – 2850 °C and peak pressures of 3000 – 4200 MPa. The pressure at the plasma rim is ≈ 25 % of the maximum compressive amplitude at the focus center (see Fig. 14 in Vogel et. al. [9]), and amounts to 750 – 1050 MPa. The corresponding pressure at the epithelium obtained using the scaling law $p \propto r^n$ with n = 1.12 and a plasma radius of 1.0 µm (value assumed for 1.76 × $E_{th,bubble}$) lies in the range between 4.3 MPa and 6.0 MPa, more than 7.6 - 10.6 times larger than with the vortex beam.

Corneal cells are not just exposed to compressive stress but to a bipolar wave in which the compressive part is followed by tensile stress. This is partly a feature of the thermo-elastic stress wave produced by isochoric energy deposition with ultrashort laser pulses [9, 170] but in corneal tissue it is also a general feature arising from the elastic tissue response that is relevant also for longer (ns) pulses [101]. The threshold for cell death after exposure to individual shock waves is ≈ 50 MPa [171, 172] but the damage threshold for bipolar stress waves was found to be smaller, around 10 MPa for the peak tensile stress amplitude[172, 173] because cells are more susceptible to tensile than to compressive stress [174]. These damage threshold data suggest that with a vortex beam, where at the cutting threshold the compressive pressure of the bipolar stress wave at the plasma rim is ≈ 50 MPa, damage is produced only in the immediate vicinity of the dissection plane. The corneal epithelium and also the endothelium, which is > 300 µm away from the cut, are safe because the pressure amplitude at 100 µm distance is only ≈ 0.6 MPa. By contrast, the damage range is much larger for the Gaussian beam, where the pressure at the plasma rim is ≈ 750 – 1050 MPa. Even in the epithelial layer pressure amplitudes of ≈ 4.3 – 6.0 MPa are reached, and each epithelial cell is exposed to about 50 pressure waves of similar amplitude because the laser pulses are applied in a raster pattern with a few micrometer spot separation. Thus, there is a certain potential for epithelial damage induced by acoustic transients waves that may become relevant if combined with other stress factors.

Besides the laser-induced stress transients, shear stress arising from cavitation bubble oscillations is another mechanical stress factor [10, 101, 102, 175]. It will be relevant in a zone reaching approximately up to the maximum bubble radius, which extends a few micrometer beyond the cutting plane (≤ 10 µm for $E_{\text{pulse}} \leq 1$ µJ with a Gaussian beam [113]). Beyond this range, stress-wave induced damage will dominate.

The above assessment of the damage range by mechanical stress is corroborated by investigations on cell viability after flap dissections in rabbit eyes with Gaussian beam that were based on ultrastructural analysis, detection of apoptosis by means of the TUNEL assay, and immunocytochemistry [109, 110]. The width of the apoptotic zone was found to be ≈ 20 µm for $E_{\text{pulse}} = 0.5$ µJ and increased to ≈ 60 µm for $E_{\text{pulse}} = 2.7$ µJ [110]. We hypothesize that the pronounced reduction of mechanical stress going along with the lower pressure amplitudes and the diminished cavitation with markedly reduce early keratocyte apoptosis and necrosis. This could lead to a diminished keratocyte proliferation and myofibroblast generation later in the wound healing process [176], which will improve the clinical outcome and predictability of refractive procedures and may further reduce haze.

Bubble layer after dissection

Cutting with vortex beam occurs close to the bubble threshold. Because in ultrashort-pulse optical breakdown, the phase transition at bubble threshold is facilitated by thermoelastic tensile stress, the threshold temperature is lowered to ≈ 150°C compared to ≈ 300°C for explosive vaporization without stress confinement [9, 119]. As a consequence, relatively little liquid is vaporized at threshold, and the amount of non-condensable gas resulting from free-electron-mediated molecular fragmentation is also small. This explains the lack of long-lived gas bubbles in dissections produced with the vortex beam (see in Fig. 5, right column).

With a Gaussian beam, the absorbed energy is 8.7 times ($\tau_L = 480$ fs) to 1.45 times ($\tau_L = 8.8$ps) higher than with the vortex beam, and the focal volume is much smaller. Therefore, the plasma density and temperature rise in the focal volume are much higher as discussed above, and peak temperatures can well exceed 1000°C. This favors free-electron-mediated molecular disintegration as well as pyrolysis and explains the large amount of non-condensable gas that forms the layer of long-lived gas bubbles [9, 142, 177-179] (seen in Fig. 4.4, left column).

Pulse duration dependence of cutting energy

A decrease of the pulse duration from 8.8 ps to 480 fs results in a reduction of the absorbed laser pulse energy required for flap cutting by a factor of 5.5 for the Gaussian beam, and by a factor of 32 for the vortex beam (Fig 4.7). This result is remarkable and not easy to understand. It is discussed in section 5.4 together with other data for UV-A wavelengths to cover a larger range of laser pulse durations and wavelengths.

Potential improvements of refractive surgery by focus shaping

An opaque bubble layer in the anterior stroma during LASIK [180] is a well-known intraoperative finding seen with all clinical femtosecond laser systems [25]. An excessive opaque bubble layer can lead to complications during flap creation, and bubble remnants remaining in the corneal stroma after flap lifting may compromise residual stromal thickness

measurements and the reliability of pupil tracking systems [26, 180]. In rare cases, vertical gas breakthrough can occur when cavitation bubbles dissect superiorly toward Bowman´s layer and through the epithelium. A vertical channel, a so called buttonhole is then created and complications like epithelial ingrowth and scarring can reduce the outcome of the procedure [27, 181]. Reduction of the opaque bubble layer when using a vortex beam can, therefore, greatly improve the dissection process.

Increase of precision and reduction of mechanical side effects in intrastromal cutting by the use of vortex beams is certainly a promising approach for the flap cutting in LASIK [4] and intrastromal pocket dissection for hyperopia correction [38, 39] but bears an even higher potential for an improvement of small incision lenticule extraction (SmILE) [6]. Here, a small lenticule is dissected and removed through a small side cut to achieve refractive correction in one step (Fig. 2.4). Formation of an opaque bubble layer is a known complication in SmILE [182-184]. Mechanical deformation of the corneal stroma by bubble formation during the lower cut may induce undesired local variations of the lenticule thickness because the mechanical distortions of the corneal lamellae by cavitation affect a significantly larger volume than the plasma-induced tissue vaporization [112, 185]. The decrease of bubble formation and mechanical stress enabled by the vortex approach along with the increase of cutting quality can improve precision and predictability of SmILE.

4.5 Conclusions on focus shaping

Possible improvements of intrastromal dissection by focus shaping were explored in an ex-vivo study on porcine eyes, using a helical phase plate for creating a vortex beam with a ring focus. The focus has the same length as with a Gaussian beam of equal NA but a four times larger cross section. The use of a vortex beam was found to improve precision and efficiency of cuts and reduce bubble formation in the cutting plane, which is of interest for LASIK and SmILE.

Cutting with the vortex beam is less disruptive and mechanical side effects are less severe than with conventional Gaussian beams. A reduction of early keratocyte apoptosis and necrosis could lead to a diminished keratocyte proliferation and myofibroblast generation later in the wound healing process, and may lower the incidence of diffuse lamellar keratitis. In SmILE, the refractive outcome largely relies on the precision of lenticule dissection. Bubble formation distorts the stromal morphology during cutting and compromises precision, and reduced bubble formation would thus improve the predictability of the surgical procedure.

Since the phase plate for creating a helical phase can be implemented into the delivery systems of existing clinical device, the vortex beam approach can be easily tested in animal experiments and clinical trials. This could enable its use in the next generation of refractive laser systems.

5. Influence of Wavelength and Pulse Duration on surgical efficiency and precision

5.1. Motivation and objectives

The dissection efficacy and precision of corneal dissection depend on focusing NA, laser wavelength, focus shape, and laser pulse duration. The focusing *NA* of the laser beam used for corneal dissection must generally be as large as possible to minimize the focus length and is kept constant at a value of *NA* = 0.38 in most investigations of this thesis. The influence of focus shape (ring focus from vortex beam vs Airy pattern from a truncated Gaussian beam) has been investigated in the previous section. In this section, the influence of wavelength and laser pulse duration is addressed.

We have seen in section 2.3 that nanosecond (ns) UV-A laser pulses with well reproducible temporal shape offer to produce deterministic nano- and microeffects in a similar way as femtosecond laser pulses [14, 186, 187] and can be used for corneal dissection. One expects an improvement of the surgical precision for the shorter wavelength, because when sub-ns UV-A laser pulses of 355 nm wavelength from a compact diode-pumped MOPA laser system are used, the focus length is about one third of the focus length for IR fs pulses at equal *NA* (see section 2.5). However, since the use of different wavelength goes along with different pulse durations, this raises the question of the pulse duration dependence of corneal dissection. It will be investigated for IR and UV laser wavelengths as well as for Gaussian and vortex beams.

5.2. Methods

The experimental setup is similar to the setup described in detail in Section 4.2 and its features are here only shortly summarized. Laser pulses were focused through a microscope objective with *NA* =0.38 into the cornea of freshly excised ex vivo porcine eyes. To achieve a homogeneous cut of the circular flap bed with a diameter of 6 mm, cavitation bubbles were produced at 150 µm depth in a raster pattern with 6-µm spot separation.

To cover the large parameter range from IR to UV wavelength and fs to sub-ns pulse duration, five different laser systems were used. A fiber-laser-based chirped-pulse-amplification system with 1030 nm wavelength and tunable pulse duration (Cazadero; Calmar Laser, Palo Alto, CA) provided IR pulses of 1030 nm wavelength at durations at 480 fs, 3 ps, and 8.8 ps, as already presented in section 4.2. Frequency-tripled laser systems with mode-locked oscillator and regenerative amplifier provided 1-ps pulses at 343 nm wavelength (Staccato, Coherent, Fremont, CA) and 10-ps pulses at 355 nm wavelength (RAPID LX UV, Coherent, Fremont, CA). Sub-nanosecond laser pulses at 355 nm were delivered by compact amplified microchip lasers, where the short oscillator length guarantees single-longitudinal mode emission with reproducible pulse shape. 200-ps pulses were provided by a Selene HM 355 laser (Coherent, Fremont, CA) and 400-ps pulses by a Powerchip PNV-0001525-140 laser (teem photonics, Meylan, FR). To convert the linear polarized Gaussian beam into a helically-phased vortex beam, phase plates were inserted into the beam path that are optimized for IR and UV wavelengths, respectively (VL-209-I-Y-A for IR and VL-209-U-Y-A for UV, both Holo/OR Ltd., Ness Ziona, Israel).

As described in section 4.1, we first determined the minimum laser pulse energy $E_{th,cut}$ that is required for easy flap lifting. This was done for every pulse duration and wavelength both for Gaussian and vortex beams. The total number of investigated corneas is n = 140. Then transmission measurements were performed, which enabled us to determine the part E_{abs} of the incident energy that was absorbed in the laser focus during dissection at $E_{th,cut}$.

5.3. Results

Figure 5.1 shows the incident laser pulse energy $E_{th,cut}$ that was required for easy flap lifting for IR and UV wavelengths and pulse durations between 480 fs and 0.4 ns both for Gaussian and vortex beams.

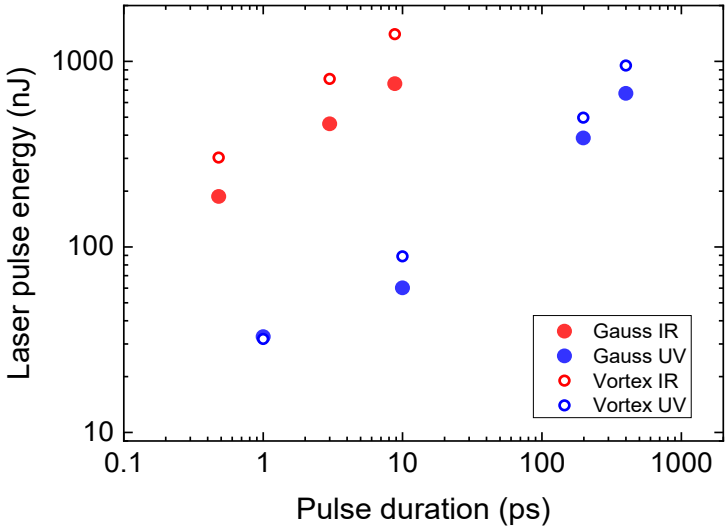

Fig. 5.1. Incident laser pulse energy $E_{th,cut}$ required for easy flap lifting during dissection of porcine cornea with IR (1030 nm) and UV-A (343 nm / 355 nm) laser pulses, applied at 6 × 6 µm spot separation (NA = 0.38).

The threshold energy for flap cutting, $E_{th,cut}$, decreases significantly with decreasing pulse duration for UV and IR wavelengths (results for IR wavelengths already shown in section 4.3). For Gaussian IR beams it drops from 759 nJ at 8.8 ps to 187 nJ at 480 fs, and for Gaussian UV beams it decreases from 672 nJ at 0.4 ns to 32.8 nJ at 1 ps. For Vortex beams the pulse energies for flap cutting are higher with the larger ring focus of the vortex beam than with the Gaussian beam, but the decrease with decreasing pulse duration is very similar to the Gaussian beam and ranges from 1.4 µJ at 8.8 ps to 303 nJ at 480 fs for IR, and 950 nJ at 0.4 ns to 31.9 nJ at 1 ps for UV. Note that both pulse duration dependencies are almost parallel in the double-logarithmic plot in Fig. 5.1, with the energies required for the flap cut for UV approximately one order of magnitude below the values for IR at the same pulse duration. The highest cutting quality with least disruptive side effects is expected at the lowest $E_{th,cut}$ values.

To demonstrate the very high cutting quality, Fig. 5.2 shows exemplary scanning electron microscopic images of a 5-mm flap created by Gaussian UV-A laser pulses from an amplified slm microchip Nd:YAG laser emitting sub-ns pulses at 355 nm wavelength (see section 3.2). The flap bed is very smooth, and the flap side cut is very precise with little distortions of the tissue structure. Even individual lamellae can be recognized in the electron micrograph.

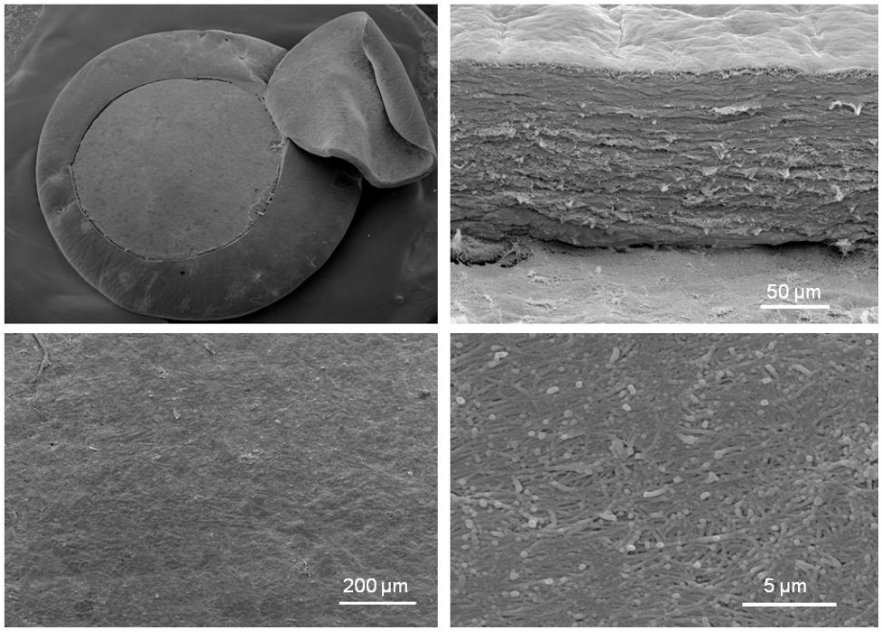

Fig. 5.2. Scanning electron microscopic images of a flap with 5 mm diameter in porcine cornea. The flap was produced with 1.0-µJ UVA laser pulses ($\lambda = 355$ nm, $\tau_L = 560$ ps) focused at NA = 0.28 with 6 µm spot separation. The cutting energy per unit area averaged over the corneal surface was 2.8 J/cm^2. The side cut (upper right image) was produced with 0.8-µJ pulses focused at NA = 0.75 with 2 µm spot separation.

The effective laser energy deposited during the flap cut is relevant for the amount of disruptive side effects and the cutting quality. Figure 5.3 shows the pulse duration dependence of the absorbed laser pulse energy E_{abs} that was required for easy flap lifting for IR and UV wavelengths and for Gaussian and vortex beams.

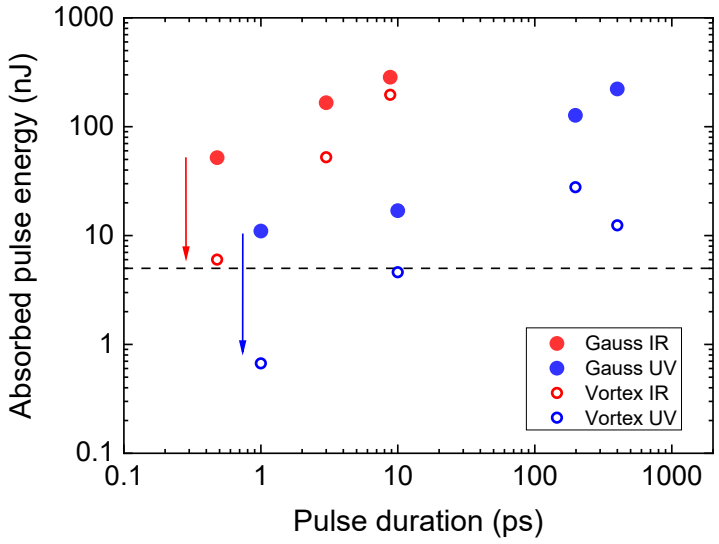

Fig. 5.3. Absorbed laser energy E_{abs} required for easy flap lifting after dissection of porcine cornea with IR (1030 nm) and UV-A (343 nm / 355 nm) laser pulses, applied at 6×6 µm spot separation (NA = 0.38). The dashed line demarcates the value of absorbed pulse energy that corresponds to the work per unit area needed for mechanical tearing of corneal lamellae at small strain rates (see section 4.4).

The absorbed cutting energy E_{abs} is considerably lower for UV-A pulses than for IR laser pulses, and also considerably lower for the vortex beam compared to the Gaussian beam (Fig. 5.3). Moreover, E_{abs} decreases with decreasing laser pulse duration, regardless of wavelength and focus shape. For IR beams E_{abs} decreases from 285 nJ (Gauss) and 196 nJ (Vortex) at 8.8 ps to 52 nJ (Gauss) and 6 nJ (Vortex) at 480 fs by a factor of 5.5 (Gauss) and 33 (Vortex). For UV beams it decreases from 222 nJ (Gauss) and 12.4 nJ (Vortex) at 0.4 ns to 11 nJ (Gauss) and 0.67 nJ (Vortex) at 1 ps by a factor of 20 (Gauss) and 19 (Vortex).

5.4. Discussion

For the same focusing conditions (beam quality, NA), a wavelength reduction from IR to UV through frequency tripling reduces the diffraction-limited focal spot size by a factor of 3, and the focal area by a factor of 9. The energy threshold for optical breakdown at constant threshold irradiance should, therefore, be 9 times lower. A similar decrease of the required cutting energy with decreasing wavelength is indeed observed in Figs. 5.1 and 5.3.

The pulse duration dependence of the *incident* laser pulse energy required for flap cutting (Fig. 5.1) shows a decrease of $E_{th,cut}$ with decreasing pulse duration, regardless of wavelength. This trend reflects the well-known decrease of the energy threshold of optical breakdown with decreasing pulse duration [100]. Remarkably, the *deposited* laser pulse energy E_{abs} (Fig. 5.3) also shows also a pronounced decrease with decreasing pulse duration. The explanation of this trend is more challenging.

Looking merely at the mechanical energy required to separtate corneal lamella, one would expect that the mechanical work needed for dissection is independent of laser pulse duration. Smolek & McCarey determined the average adhesive strength in human corneas by measuring the tearing force required to separate the cornea lamellae [168]. They found a tearing force per unit tissue width of F_{spec} = 0.142 kp/cm which corresponds to a tearing work of E_{sep} = 1.39 10^{-2} J/cm² and the required separation energy amounts to E = 5 nJ for the cutting area at 6 x 6 µm spot separation. This value is marked as dashed line in Fig. 5.3 - and it turns out that the values for UV Vortex pulses at short pulse durations are below this value. For the shortest pulse duration of 1 ps, the value of the absorbed energy required for a flap cut is 0.67 nJ, a factor of 7.5 below the separation energy determined by Smolek & McCarey. This observation becomes even more remarkable if one considers that Smolek & McCarey determined the lamellar adhesive strength along physiological separation lines, while laser dissection may also involve the rupture of collagen fibrils.

Smolek & McCarey' values were determined for relatively slow separation of the lamellae at small stress vakues. However, tissue properties change at high strain and tearing rates [3], and this may implicate that the separation energy also changes. Brujan and Vogel determined the elastic tissue properties of cornea under the rapid deformation by an expanding cavitation bubble and found values of E = 144 MPa for the elastic modulus, G = 48 MPa for the shear modulus, and Y = 74 MPa for the fracture stress [101]. The elastic modulus of the human cornea under physiological conditions is much smaller, in the range of 0.2 – 0.5 MPa [147-149]. This means that under rapid deformation such as during bubble formation for intrastromal cutting, the cornea stiffens [3, 150] and tearing becomes 'cleavage'. As discussed in section 3.4, the

intrastromal ‘cleavage’ process is not merely a succession of individual disruptive events but also influenced by the interaction of subsequent cavitation bubbles. Thus, cleavage may assume some features of fracture and crack propagation in solids [152, 156]. However, even if these features reduce the energy required for lamellar separation, they do not suffice to explain the observed dependence on laser pulse duration. For this purpose, one has to look at the τ_L dependence of the energy efficiency of individual effects involved in crack initiation and propagation.

Factors governing the strength of the individual thermomechanical effects in bulk media are *1. plasma features* (shape and energy density), *2 Pulse energy dependence of nonlinear absorption and conversion into mechanical energy* (reflected in the slope of the $R_{max}(E_L)$ curve), *3. Thermal, stress, and inertial confinement of energy deposition. 4. Rupture strength and viscoelastic properties of corneal tissue.* The first three factors influence the vigor of shock wave emission and bubble dynamics, which are relevant for fibril rupture and cleavage. The first two factors are little influenced by the breakdown medium, (whether it is water or tissue) but the overall confinement becomes stronger, when inertial confinement is complemented by an elastic deviatoric force and a rupture threshold must be overcome. In the following, all factors are discussed step by step.

Plasma absorption and energy density

Variations of the plasma absorption coefficient with laser pulse duration lead to changes of the plasma energy density and peak pressure. It was found experimentally, that plasma transmission first increases, when the laser pulse duration is shortened from the nanosecond into the picosecond range, has a maximum at a few ps, and decreases again when the pulse duration is shortened into the fs range [100, 118] [Fig. 5.4(a)]. This observation is corroborated by numerical simulations by Noack and Vogel [8] [Fig. 5.4(b)].

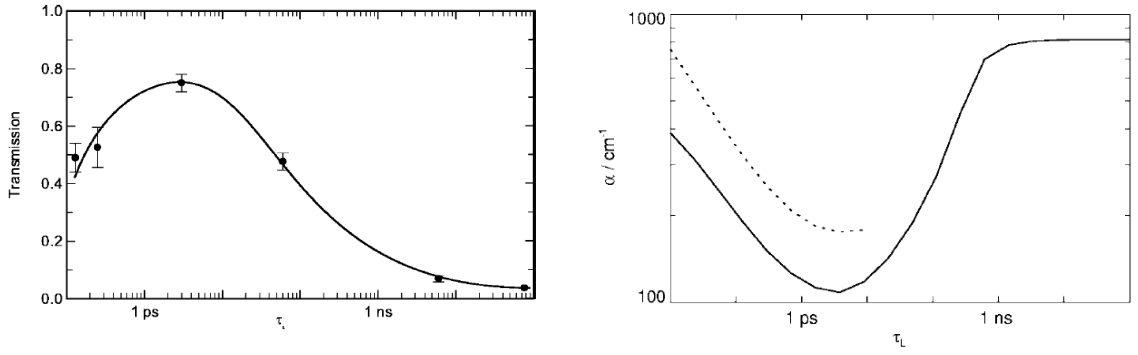

a) b)

Fig. 5.4 Pulse duration dependence of (a) the plasma transmission at six times bubble threshold [118] and (b) the simulated average plasma absorption coefficient obtained with the optical breakdown model by Noack & Vogel [8]. In (a), the wavelength was 750 nm for 76-ns pulses, 1064 nm for 6-ns pulses, 532 nm for 60-ps pulses, and 580 nm for all other pulse durations. In (b), the solid line represents λ = 580 nm, and the dashed line λ = 1064 nm. The data refer to optical breakdown in water at moderate numerical aperture, similar to the used in refractive eye surgery.

The simulations in [8] showed that for the ps pulses a high electron density is reached only late during the laser pulse, after its irradiance maximum is surpassed, which diminishes absorption.

The absorption coefficient grows in the femtosecond domain, because the increasingly strong generation of free electrons by multiphoton absorption results in an early rise of the free electron density, which is then amplified by avalanche ionization $\propto \rho \times I$. As a consequence of the higher time-averaged absorption coefficient at $\tau_L = 480$ fs, the plasma volume into which a given amount of laser energy is absorbed should be smaller than for the ps pulses. Therefore, for a given laser pulse energy, the energy density and plasma pressure are higher at shorter laser pulse duration. This implies that the pressure values required for disruptive tissue dissection are reached at lower pulse energies for the shorter pulse durations.

Future spatio-temporal simulations of plasma growth and plasma energy density distribution are still needed to confirm this hypothesis. Although the necessary tools already exist for femtosecond breakdown [188-191], they still need to be developed for nanosecond breakdown where besides stong-field and avalanche ionization also recombination and thermal ionization play a role (see section 2.3). Moreover, it should be noticed that the simulations in Ref. [8] were performed with an optical breakdown model that simply assumed a band gap of 6.5 eV for water and did not yet consider the complex band structure of water [7, 53, 60]. Furthermore, it did not consider nonlinear beam propagation effects that become relevant at the moderate NAs used for corneal dissection [188]. Nevertheless, the experimental results quoted in Fig. 5.4(a) provide evidence for a pulse duration dependence of plasma absorption and energy density at pulse durations below a few picoseconds. The higher plasma energy density at shorter pulse duration as a result of the higher average absorption coefficient could therefore be one factor explaining that shorter pulses are more efficient in intrastromal dissection.

Nonlinear beam propagation

Lower limits for an increase of plasma energy density by reduction of laser pulse duration are given by plasma filamentation through nonlinear beam propagation through self focusing in conjunction with plasma defocusing [192]. Self focusing depends on irradiance and is favored by shorter pulse durations. Heisterkamp and coworkers reported up to 100 µm long streaks in the corneal stroma, when 780-nm pulses of 160 fs duration and 1 µJ energy were focused with a spot size of 5 µm [106]. They attributed the streaks to chemical tissue modifications by low-density plasma in plasma filaments. The focusing NA used in their experiments is not given but they state in the discussion that "in initial experiments with a higher aperture (NA > 0.2) streak formation was significantly reduced" [106]. Modern clinical systems have numerical apertures larger than 0.2, and pulse energies required for flap cutting at $\tau_L = 160$ fs are well below 1 µJ. In the present study, the energy needed for flap cutting with Gaussian 1030-nm, 480-fs pulses focused at $NA = 0.38$ was less than 200 nJ (Fig. 5.1), and no indications for filamentation were found in scanning electron micrographs.

Tunability characteristics of energy deposition

Figure 5.5 (a) shows the maximum cavitation bubble radius as a function of laser pulse energy together with a range of bubble sizes in water between 10 µm and 20 µm radius that should be large enough to bridge the gap between laser spots by corneal cleavage, when a Gaussian beam is used. The maximum bubble size in cornea is (for the same laser pulse energy) approximately 4 times smaller than in water, as already shown in section 3.3 (Fig. 3.5). The corresponding conversion rates of the *incident* laser energy into bubble energy are shown in Figure 5.5 (b). In

the small-bubble regime, the conversion rate is considerably smaller for sub-ns UV-A laser pulses than for fs pulses and, as a consequence, the incident laser energy for producing the same bubble sizes must be larger for the longer pulse duration. However, this does not yet explain, why also the *absorbed* pulse energy needed for dissection is larger (Fig. 5.3). To understand this observation, one must consider that the bubble size required for cutting lies in the transition between small bubble regime and luminescent plasma regime. Therefore, it is likely that during dissection mostly luminescent plasmas are produced that have a higher absorption than plasmas in the small-bubble regime. This increases E_{abs} for cutting at longer pulse duration, in agreement with the observed pulse duration dependence in Fig. 5.3.

In corneal stroma, the transition regime will be not as sharp as in water because tissue contains many biomolecules with lower excitation energy than water molecules [88-92], which smoothen the transition and make it more stochastic [193, 194]. Therefore, the increase of laser light absorption and bubble size in corneal dissection with UV-A sub-ns pulses will likely be not quite as large as suggested by Fig. 5.4 (a) but it will certainly be a significant reason for the pulse duration dependence of the cutting threshold.

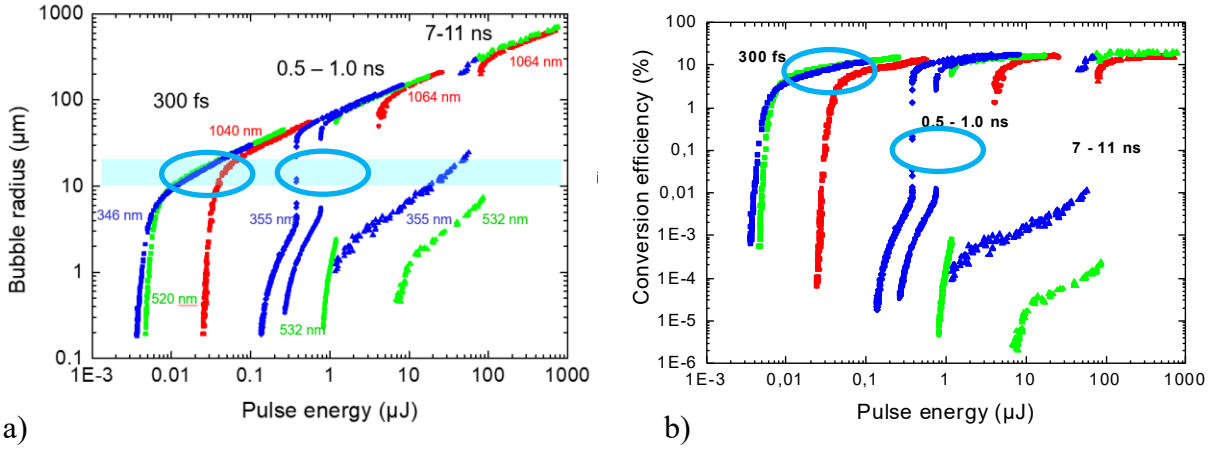

a) b)

Fig. 5.5 (a) Maximum cavitation bubble radius as a function of laser pulse energy for different pulse durations and wavelengths for bubble generation with mode-locked or single longitudinal mode laser pulses at NA = 0.8 [data form Fig 2.6 (c)]. The colors denote the wavelengths: blue = 347 nm for fs pulses, and 355 nm for ns pulses; green = 520 nm and 532 nm, respectively, red = 1040 nm and 1064 nm. The blue bar indicates a range of bubble sizes in water between 10 µm and 20 µm. In cornea, the bubble sizes at same E_L are 4 times smaller than in water (see Fig. 3.5) and corneal dissection in the corresponding bubble radius range between 2.5 µm and 5 µm would be possible at a spot separation of 6 µm. (b) Conversion of incident laser energy into the cavitation bubble energy for the data in (a), quoted from [15].

Thermal and stress confinement

At laser pulse durations below 1 µs, energy deposition is fast enough that losses by heat diffusion out of the focal region play no role [3]. Hence, energy deposition in the entire investigated parameter range between 0.4 ns and 480 fs is ***thermally confined***.

If not only heat diffusion but also thermal expansion of the heated volume is suppressed during the laser pulse, the energy deposition is isochoric. This condition is often denoted as "*stress confinement*" because thermal expansion occurs with sound velocity, and its suppression leads to the buildup of thermoelastic stress during heating [3, 9]. Stress confinement is much

harder to achieve than thermal confinement. It requires that the laser pulse duration τ_L is shorter than the stress relaxation time τ_{ac} given by the propagation time of acoustic waves through plasma volume: $\tau_{ac} = R_0/c_\infty$, where c_∞ is the sound velocity. This leads to the stress confinement condition

$$\tau_L / \tau_{ac} = \tau_L \frac{c_\infty}{R_0} \leq 1 \tag{5.1}$$

The buildup of compressive thermoelastic stress results in a radial outward motion of the heated material that, in turn, produces tensile stress within the source, which then facilitates a phase transition and bubble formation[3, 170, 195]. Such bipolar stress wave with tensile component is formed if the energy density within the source lies below the kinetic spinodal limit for homogeneous nucleation (≈ 300°C at ambient pressure) [3]. Above this limit, bubble formation is driven by explosive vaporization in the same way as for longer pulses without stress confinement [119]. Thus, thermoelastic tensile stress plays a role only for bubble generation by ultrashort pulse durations in a small energy range reaching from the bubble threshold, E_{th}, up to about $1.1 \times E_{th}$ [119]. It is particularly relevant for corneal dissection with a vortex beam, which occurs close to the bubble threshold.

Plasma-mediated heating occurs by thermalization of the energy of the free electrons via collisions and recombination. At plasma densities leading to bubble formation, this process is completed within 10-20 ps [7, 79]. Thermal expansion of the focal volume is completed when the expansion wave traveling with sound velocity has reached the periphery of the heated region. For the sound velocity in water or tissue of ≈ 1500 m/s = 1.5 µm/ns and a plasma radius of ≈ 1 µm, this takes 666 ps. Thus, energy deposition is 'stress confined' for all pulse durations investigated in this study but *the degree of stress confinement* varies. The degree of stress confinement is given by the amplitude of the thermoelastic stress wave for a given pulse duration divided by the amplitude for instantaneous heating [195]. It depends on laser pulse duration and the source size, which can be expressed as equivalent spherical plasma volume R_0. The plasma volume depends on wavelength, focusing NA and wavelength. It is not exactly known for corneal dissection and the degree of stress confinement can only be estimated. It increases slightly from ≈ 30% at 0.4 ns to 100% at a few ps pulse duration [195] but is not strong enough to fully explain the observed dependence of cutting energy on pulse duration that decreases by a factor of 20 for the UV wavelength.

Inertial confinement

Another factor that comes into play during the cavitation bubble expansion after the initial tearing of collagen fibrils is ***inertial confinement***. For very small plasma volumes, a significant movement of the bubble wall during the laser pulse will reduce the peak pressure that can be reached for a given pulse energy and thus the disruptive force of the laser pulse. The criterion for inertial confinement is that the volume of the seed bubble, in which the phase transition occurs, increases less than a factor of 2 during the laser pulse [96]. Assuming a $\sin^2$ shape of the pulse with duration τ_L (width at half maximum) and total duration $2\ \tau_L$ [see Eq. (2.12)], the confinement criterion for a spherical source with radius R_0 reads

$$\left(R\big|_{t=2\tau_L}\right)^3 \leq 2R_0^3, \quad \text{or} \quad \frac{R\big|_{t=2\tau_L}}{R_0} \leq \sqrt[3]{2} \approx 1.26\,. \tag{5.2}$$

Since inertial confinement increases with decreasing laser pulse duration, higher peak pressures are reached in fs breakdown than at τ_L = 0.4 ns. Hence, variations of inertial confinement may contribute to the pulse duration dependence of cutting energy.

While stress confinement refers to stress relaxation at sound velocity, which is fixed, fulfillment of inertial confinement relies on the initial bubble wall velocity, which depends on plasma energy density. In contrast to stress confinement that is most relevant for dissection occurring close to the bubble threshold, the influence of inertial confinement is relevant in all cases. Figure 5.6 shows the bubble expansion *R(t)* during the laser pulse for various pulse durations between 100 fs and 5 ns [96].

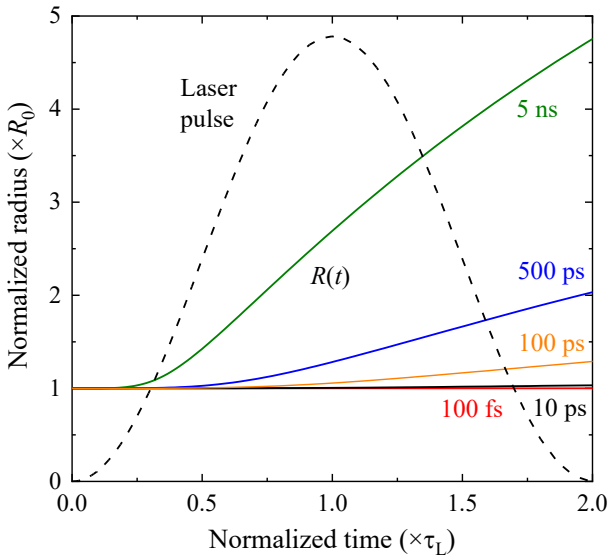

Fig. 5.6 Bubble expansion during the laser pulse for various pulse durations. All calculations were performed for R_0 = 210 nm and R_{nbd} = 10.4 R_0 using the Gilmore/Liang model of section 2.2.) The figure is from Ref. [96].

The degree of inertial confinement does not only influence the bubble pressure and bubble wall velocity but also determines whether the acoustic transient emitted during plasma expansion forms a shock front and how large the pressure and velocity jump at the shock front are [95]. In fs breakdown, energy deposition is isochoric, and the bubble wall does not move during the laser pulse. In this condition of full inertial confinement, the shock front forms right at the plasma boundary during the laser pulse. The initial plasma and bubble pressure P is identical with the shock pressure p_s, and the initial bubble wall velocity equals the initial particle velocity behind the shock front. This results in a "jump-start" of the bubble wall. For longer pulse durations, the bubble wall starts to move already during the laser pulse, which influences the pressure buildup during energy deposition. Here, shock front formation occurs only after the pressure transient has moved a certain distance and steepened through the nonlinearity of sound propagation at high pressure. The bubble wall still exhibits a rapid start due to the particle velocity in the high-pressure liquid region but its velocity is much smaller than for ultrashort laser pulses due to the lower bubble pressure.

Figure 5.7 shows the pulse duration dependence of bubble expansion during the laser pulse, bubble size at maximum expansion, peak bubble pressure and peak bubble wall velocity for a bubble in water with $R_{max} \approx 5$ µm. Simulations are performed for $R_0 = 210$ nm and $R_{nbd} = 10.4\ R_0$. In simulations with the Gilmore model, the ratio $R_{nbd} = / R_0$ reflects the plasma energy density [96]. The value of 10.4 was adopted from a fit to experimental results obtained for IR fs breakdown goind along with explosive vaporization of the plasma volume [95].

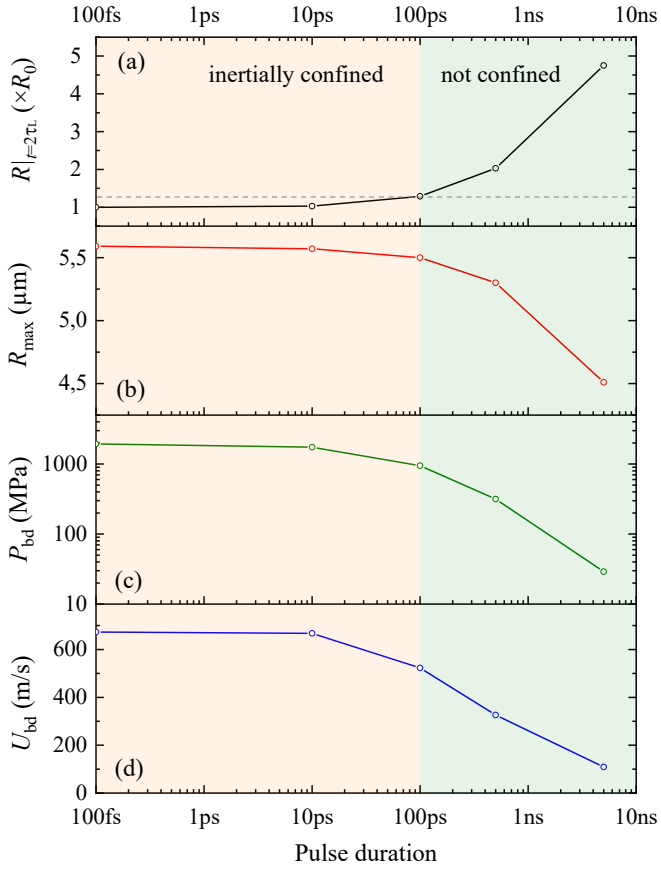

Fig. 5.7 Change of bubble parameters as a function of laser pulse duration for $R_0 = 210$ nm and $R_{nbd} = 10.4\ R_0$. The loss of inertial confinement degree shown in (a) diminishes the maximum bubble size R_{max} (b), the peak breakdown pressure P_{bd} (c), and the peak bubble wall velocity U_{bd} (d). Calculations were performed for pulse durations between 100 fs and 5 ns; the solid lines are drawn to guide the eye. The figure is from Ref. [96].

The peak bubble pressure drops to about 1/6 of the value for fs breakdown, when the pulse duration is increased from the femtosecond range to 0.5 ns, and the peak bubble wall velocity drops by about 50% [Figs. 5.7 (c) and (d)].

Changes are even larger for the pressure and velocity jump at the shock front, as seen in Fig. 5.8. For 0.5 ns pulses, the shock pressure is only 1/144 of the respective value at 100 fs, and the bubble wall velocity drops to 1/79. For 5-ns pulses, no shock front evolves at all.

The pulse duration dependencies in Figs. 5.6 to 5.8 suggest that the loss of inertial confinement with increasing pulse durations contributes to the increase of dissection energy for sub-nanosecond laser pulses. However, the simulations can only illustrate parameter dependencies. For quantitative predictions of bubble pressure and wall velocity for specific experimental conditions, the respective equivalent plasma radius R_0 and the maximum bubble size R_{max} must be experimentally determined [95].

For pulse durations below 10 ps, the change of shock pressure and particle velocity is not strong enough to explain the drop of flap cutting energy by more than one order of magnitude, when the pulse duration is reduced from 10 ps to 480 fs (Fig. 5.3). Here, changes of plasma energy density come into play, as discussed further above in the context of Fig. 5.4.

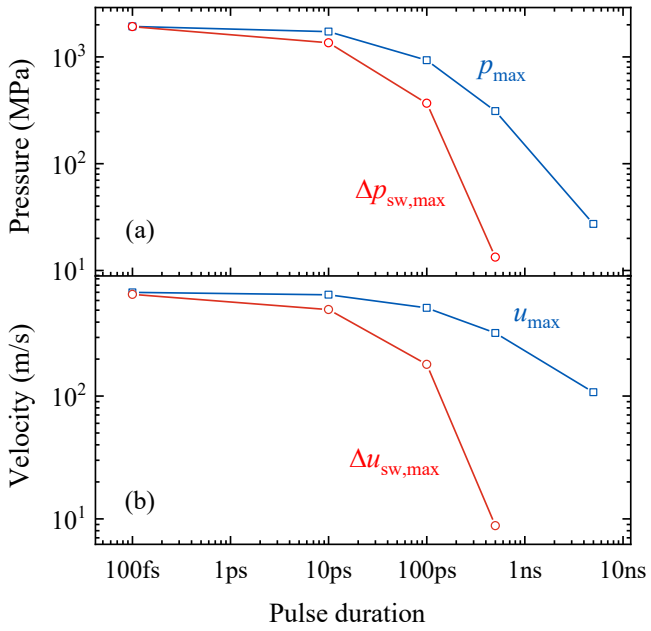

Fig. 5.8 (a) Pulse duration dependence of the peak pressure in the liquid, p_{max}, during acoustic transient emission and the maximum pressure jump at shock front, $\Delta p_{sw,max}$. (b) Pulse duration dependence of the peak velocity within the liquid, u_{max}, and the maximum particle velocity behind the shock front, $\Delta u_{sw,max}$. The respective R_{max} values are the same as in Fig. 5.7. The figure is taken from Ref. [96].

Tissue properties and rupture dynamics

A major point not yet considered in the discussion of the pulse duration dependence of corneal dissection is the difference between laser-induced bubble dynamics in tissue and water. Bubbles are smaller in tissue than in water, i.e. the confinement by the surrounding medium is stronger. The initial bubble wall movement is influenced not only by the particle velocity behind the shock front but also by the deviatoric stress of the viscoelastic tissue and by the threshold for fibrillary rupture. For reaching the same bubble size in tissue as in water, a much larger breakdown pressure is needed because the deviatoric elastic stress and viscous damping must be overcome. The increased pressure required to produce a given R_{max} value makes it easier to overcome the fibrillary rupture threshold and - vice versa - a constant rupture threshold can be overcome with breakdown producing a smaller bubble. A homogeneous cut can be produced as long as the bubbles are sufficiently large such that the cleavage regions from neighboring laser spots merge smoothly.

The tissue response to free-electron mediated bond breaking in combination with mechanical stress influences the fibrillary rupture threshold. Changes of this interplay with laser pulse duration may contribute to the τ_L dependence of dissection. Covalent bonds in biomolecules can be broken through interactions with the CB electrons in the laser plasma – regardless on plasma temperature [9, 15, 60]. The bond breaking capability of CB electrons depends on their energy, which lies between 0 eV and the impact ionization energy (3/2) $\tilde{\Delta}$ of

≈ 14.5 eV in water (see section 2.3). For laser parameters used in corneal dissection, the mean CB electron energy is ≈ 6.5 eV at 1035 nm and ≈ 8.0 eV at 350 nm [60] – enough to break a large variety of covalent bonds. Bond breaking by low-energy electrons has been studied for DNA (mainly in the context of radiation therapy) [90, 196] and for proteins (mainly in the context of proteomic mass spectroscopy) [197, 198]. It occurs on ultrashort time scales and plays a role also in laser-plasma-mediated corneal dissection [199].

Shock fronts exhibit strong pressure gradients at a scale of the mean free molecular path length in liquid water, which is smaller than the length of biomolecules [200-202]. The influence of mechanical stresses on molecular rupture in pulsed laser ablation has been investigated by Kitai et al. [203], and the influence of shock front passage on cells in Ref. [204]. The combination of tissue weakening by molecular bond breaks and large localized stress values will lower the fibrillary rupture threshold. A larger pressure jump and -gradient requires a smaller density of molecular bond breaks to overcome the rupture threshold. Vice versa, a larger plasma energy density going along with a higher CB electron density will increase the density of electron-mediated bond breaks and facilitate rupture. Hence, the increase of shock pressures with decreasing laser pulse duration (Fig. 5.8) and the corresponding increase of plasma density (Fig. 5.4) go hand in hand in enabling dissection with lower pulse energy by sub-picosecond pulses.

For testing these hypotheses through numerical simulations, the radial deviatoric stress corresponding to the viscoelastic properties of the medium, as well as the rupture strength of the medium must be included into the bubble model [101, 102]. Furthermore, the influence of free-electron-mediated bond breaking and mechanical stress on tissue rupture under high strain rates on a molecular and microscopic level requires a better understanding. Another aspect needed to portray the pulse duration dependence of plasma energy density is the inclusion of spatiotemporal properties of plasma formation into the breakdown modeling. These are all challenging tasks for future theoretical work. The experimental results of the present thesis can guide model development and validation.

5.5 Conclusions for laser parameter optimization

We have found a strong influence of wavelength and pulse duration on surgical efficiency and precision for intrastromal cutting. For constant focusing conditions (NA), the energy required for flap cutting can strongly be reduced by shorter wavelengths, shorter pulse duration and focus shaping. Use of shorter wavelengths (355 nm or 347 nm instead of 1030 nm) reduces the absorbed energy needed for flap cutting by a factor of ≈ 5 for fs pulses and even 10-fold for 10-ps pulses. Focus shaping of the Gaussian beam into a vortex beam further reduced the volumetric energy density and increases the surgical precision. Lower limits for τ_L are given by plasma filamentation through nonlinear beam propagation that involves irradiance-dependent self-focusing and is favored by shorter pulse durations[192]. However, pulse energies required for flap cutting in modern clinical systems and in the present study are lower and numerical apertures are larger than those reported in an earlier study, where side effects by nonlinear beam propagation were reported [106].

The factors relevant for a drop of dissection energy with decreasing pulse duration are complex and change with pulse duration. Around 500 ps, the shift of the work point for flap

cutting into the BPL regime increases the absorbed pulse energy needed for cutting. Between 500 ps and 10 ps, the increase of inertial and stress confinement with decreasing τ_L results in an increase of breakdown pressure and initial bubble wall velocity. Below 10 ps, a change of plasma energy density may lead to a further pressure increase beyond the effects of inertial and stress confinement. These factors help to overcome the threshold for collagen fibril disruption, which is needed to initiate the dissection process through laser-induced cavitation.

A deeper theoretical understanding of these effects requires a spatiotemporal modeling of plasma formation and a consideration of the viscoelastic tissue response and its rupture threshold.

Altogether, the findings of this thesis confirm the high suitability of pulse durations in the lower fs range down to about 150 fs, which can be produced by modern solid state and fiber laser systems.

6. Safety considerations

For Femto-LASIK at IR wavelengths, Juhasz and coworkers performed studies that proved low temperature rise [43], and clinical practice has proven that the method is safe. By contrast, for corneal dissection using an UV-A wavelength of 355 nm, the question arises, whether the method is safe for corneal epithelium, endothelium, and the retina.

Figure 6.1 provides an overview about the wavelength dependence of corneal transmission and of the transmission of the entire eye up to the retina. While the corneal transmission does not depend on age, the UV light absorption in the lens, which governs the transmission to the retina, increases strongly with age [205]. The changes on the lens protein resulting in their increased absorption are caused by sunlight, have a protective effect for the retina and are, at the same time, a major cause of cataract at old age [206]. Since refractive laser surgery is only performed after adolescence, when the growth of the body and eye has ceased, only data for ages ≥ 20 years are included in Fig. 6.1.

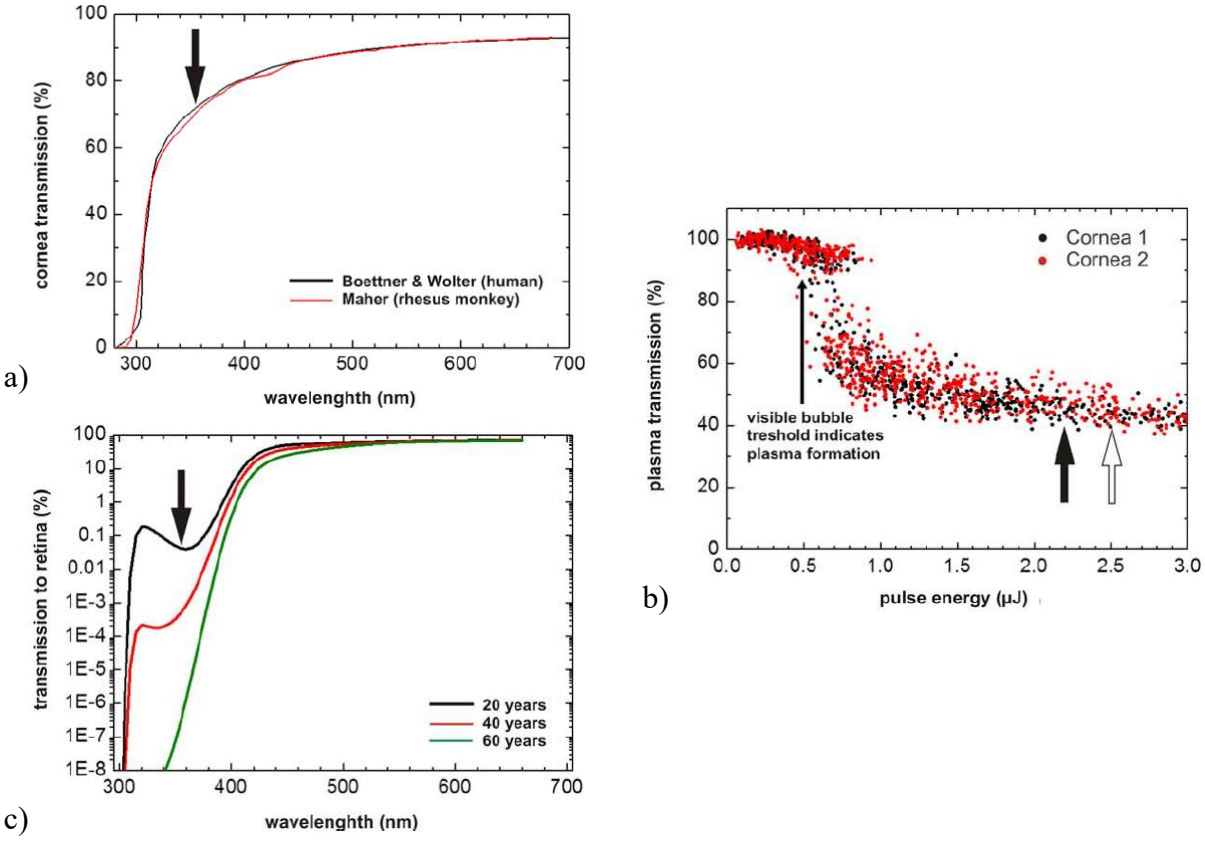

Fig. 6.1. Assessment of retinal safety with UV-A corneal laser surgery. (a) Corneal transmission at different wavelengths in human and rhesus monkey, according to experimental data of Boettner and Wolter [137] and Maher [207] at 355 nm. The black arrow represents the laser wavelength 355 nm. Here, 70% of the light is transmitted through the cornea, while 30% of UV radiation is absorbed within corneal tissue. (b) Transmittance of the 355-nm laser pulses through porcine cornea as a function of pulse energy. For the energies used for flap cutting, the laser plasma absorbs 54% (at 2.2 mJ, black arrow) and 56% (at 2.5 µJ; white arrow), respectively of the incident light. (c) Light transmission to the retina, calculated with the help of mean density and aging coefficients, introduced by van de Kraats and van Norren [205]. These coefficients allow to determine average data for the age and wavelength dependence of ocular transmittance. At 355 nm (black arrow), less than 0.1% of the applied light at the cornea will reach the retina in a 20-year-old eye, and this fraction further declines with age to less than 0.005% at 40 years and < 10^{-6} % at 60 years. The figure is adapted from Ref. [186].

At the age of 20, less than 0.1% of the radiation incident on the cornea is transmitted up to the retina, where it is spread over a much larger area than the flap diameter in the corneal stroma. This way, the radiant exposure of 6.9 J/cm^2 needed for flap dissection in rabbit eyes with 355-nm, 850-ps pulses at 150 kHz [186], translates into a retinal irradiation dose well below 10^{-3} J/cm^2, which is regarded to be safe [205, 208].

Potential damage of the corneal epithelium and endothelium is more likely because of two reasons: 1. The mechanical stress arising from shock waves and bubbles associated with laser-induced plasma formation may produce a 'negative synergy' with the UV-A induced stress. 2. The large irradiance in the vicinity of the laser focus my lead to two photon absorption, which could cause cellular damage in keratocytes also in epithelial and endothelial cells. Since epithelial cells are typically only ≈ 100 µm away from the dissection plane, damage is here more likely than for endothelial cells that are 300-400 µm away and, furthermore, protected by corneal and plasma absorption [Figs. 6.1(a) and (b)]. Thus, short-pulsed laser irradiation implicates a larger damage probability for the cornea than incoherent radiation. This is considered in the maximum permissible exposure (MPE) values presented in Fig. 6.2.

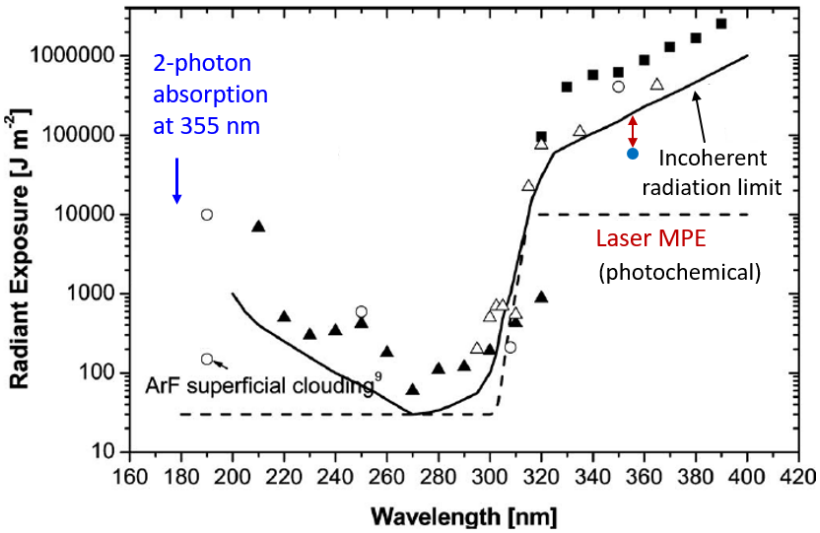

Fig. 6.2. Comparison of dissection parameters at 355 nm with maximum permissible exposure values. The graph is adapted from Ref. [17], ICNIRP Guidelines on limits of laser exposure to wavelengths between 180 and 1000 nm. The blue dot indicates the radiant exposure of 6.9 J/cm^2 needed for flap dissection in rabbit eyes with 355-nm, 850-ps pulses at 150 kHz [186]. It is a factor 2.7 below the maximum permissible exposure (MPE) at the cornea for incoherent light (19 J/cm^2) but 7 times above the much more conservative laser MPE (1 J/cm^2 up to 400 nm).

The energy of 2 photons is 7 eV, sufficient to damage and even ionize DNA bases, water, and some amino acids [60, 88, 90]. Therefore, photochemical damage by two-Photon absorption at 355 nm could possibly lead to epithelial clouding, which has been observed after one-photon absorption of ArF laser irradiation with photon energies of 6.42 eV (Fig. 6.2). Such clouding is usually transient because of epithelial regeneration but not compatible with a clinical refractive procedure.

Use of a vortex beam for corneal dissection would mitigate the additional mechanical stress aggravating the stress from UV-A irradiation but there was no opportunity to test this on animals or in preclinical trials. Moreover, the MPE values at 355 nm (Fig. 6.2) already prohibit to

perform such trials for UV-A pulse from compact and cost-effective laser devices emitting sub-ns pulses. With UV fs lasers, corneal dissection can be performed with considerably smaller pulse energies [209, 210] but such lasers are more costly than IR fs lasers, and the design and manufacturing of UV delivery optics for clinical devices is also challenging and costly.

By contrast, the novel focus shaping approach presented in this thesis is safe, when implemented into IR fs laser system, and it enables to perform more precise and gentler dissection than present clinical systems.

7. Conclusions and future perspectives

In this thesis, the mechanisms of corneal dissection for refractive eye surgery were experimentally investigated, and novel approaches for gentle and precise cutting were presented and explored. Experimental results were analyzed using modeling results from the research team at the Institute of Biomedical Optics.

The cutting dynamics was analyzed with unprecedented spatiotemporal resolution using a combination of stroboscopic photography, high-speed photography with up to 50 million frames/s, high-speed videography and histologic analysis. Dissection proceeds through disruption of collagen fibrils and cleavage of lamellae. The process is initiated by vaporization of tissue in the plasma volume and driven by the high plasma pressure and the rapidly expanding cavitation bubble. The cutting process is largely an addition of individual disruption/cleavage effects, which depend mainly on pulse energy and spot separation. However, it has also a dynamic component resembling crack propagation during fracture in solids, which implicates a dependence on pulse repetition rate. The relative strength of both components still remains to be analyzed but present results indicate that the first component dominates in clinical procedures.

It could be shown that the elongated shape of the laser plasmas in direction perpendicular to the desired cutting direction compromises the cutting precision. The plasma extends through several corneal lamellae and its rapid expansion leads to irregularly shaped lobular cavitation bubbles. Lobes from neighboring bubbles do not always meet, which leads to tissue bridges impairing flap lifting or lenticule extraction. The irregular cutting process increases the pulse energy required for dissection, which goes along with the generation of relatively large gas bubbles that dissolve only slowly and affect the precision of lenticule cutting in SmILE.

Dissection can be improved by focus shaping using a Laguerre-Gaussian vortex beam. Vortex beams are propagation invariant like a Gaussian beam but feature a ring focus with larger diameter than a Gaussian beam but the same focus length. The directional distribution of the forces during the plasma expansion from a ring focus facilitates tissue cleavage in the cutting direction parallel to the corneal surface. Scanning electron microscopy showed that the cuts are smoother than with a Gaussian beam. Furthermore, the volumetric energy density in the focal volume is considerably smaller with a vortex beam than with a Gaussian beam, which reduces plasma pressure and mechanical side effects. The smaller plasma energy density results in less permanent gas generation by free-electron-mediated molecular disintegration and, thus, in a strong reduction of long-lived gas bubbles. Altogether, dissection using a vortex beam is more precise and gentler than with a Gaussian beam.

It was shown that the precision of corneal dissection can be further improved by using UVA laser pulses at 355 nm or 347 nm instead of the near-IR laser pulses presently used clinically. However, although the photodamage potential of the investigated UVA wavelengths lies four orders of magnitude below the peak value [16] and no corneal damage was observed in previous animal experiments [186], the total radiant exposure required for flap cutting was found to lie above the maximum permissible dose [17].

Both for UV and near-IR wavelengths, a strong pulse duration dependence of absorbed laser energy required for easy flap lifting was observed. At longer laser pulse durations, the cavitation

bubble starts to expands already during the laser pulse, which reduces peak pressure and bubble wall velocity and, thus, the disruptive power needed for corneal dissection [96]. This effect plays a major role for pulse durations longer than ≈ 10 ps. For shorter pulses, plasma formation is both inertially and stress confined, and peak pressure and bubble wall velocity remain constant regardless of τ_L if plasma volume and pulse energy are constant. Here, other factors must contribute to the observed lowering of cutting energy. One possibility is an increase of plasma energy density with decreasing pulse duration that was predicted by numerical simulations and corroborated by experimental results for $\tau_L < 3$ ps [8, 118]. Like an increase of inertial confinement, an increase of plasma energy density also results in a larger plasma pressure. Both effects lower the pulse energy required for collagen fibril disruption, which is the starting point of dissection that is afterwards driven by the bubble expansion.

Lower limits for τ_L are given by plasma filamentation through nonlinear beam propagation that involves irradiance-dependent self-focusing and is favored by shorter pulse durations [106]. However, for pulse energies close to the flap dissection threshold, no indications for filamentation were found in scanning electron micrographs or in recent literature. The findings of this thesis confirm the high suitability of pulse durations in the lower fs range, which are presently employed in clinical systems.

Implementation of focus shaping into clinical systems

The improvement of dissection through use of a vortex beam instead of a Gaussian beam is the finding of this thesis with greatest clinical relevance. Like Gaussian beams, Laguerre-Gaussian vortex beams are propagation invariant, i.e. after the phase plate the beam retains its vortex characteristics along the entire beam path. This feature enables an easy implementation of the phase plate into a beam delivery system and is compatible with scanning. The phase plate can be easily swung in and out of the laser beam to switch between Gaussian and vortex beam [12]. While the vortex beam is advantageous for lenticule cutting in SmILE and the flap bed in LASIK, the Gaussian beam with a more elongated plasma shape may be better suited for vertical side cuts of the LASIK flap.

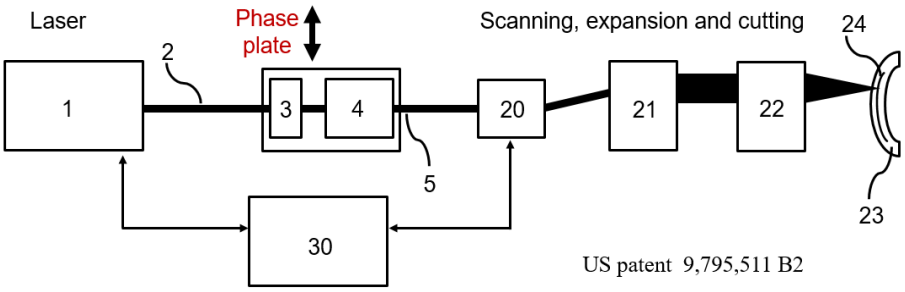

Fig. 7.1. Drawing adapted and modified from US patent on corneal dissection with vortex beam [12].

Alternative approaches for creating a ring focus do not have these advantages. A lens-axicon combination provides a ring focus at the focal plane of the lens [211] but the z-location of the optical elements is critical, combination with beam scanning is difficult, and the ring focus is longer than the Gaussian focus without axicon because the effective NA in the optical system is halved by the use of an axicon. By contrast, the ring focus of a vortex beam has the same length as the Gaussian focus produced at equal NA. Beam shaping by diffractive or refractive

optics can produce arbitrary intensity distributions in a plane of interest, which can also be the focal plane of a laser [212]. However, the z-location of the optical elements is again critical, and combination with beam scanning is impossible. Moreover, intensity peaks (“hot spots”) are usually located in front or behind the plane with the desired intensity distribution, which compromises plasma-mediated cutting in a well-defined plane. Instead, the creation of vortex beams by insertion of a spiral phase plate is a simple, versatile, and cost-effective way of improving the efficiency and precision of intrastromal corneal dissections for LASIK and SmILE.

In vitro tests on porcine eyes with a commercial medical device emitting IR fs pulses at MHz repetition rate have already been done and confirmed the laboratory results presented in this thesis. An obstacle for a rapid clinical implementation of the novel technique is the need for a clinical study required by regulatory rules for clinical instruments. This goes along with high costs, and the present economic crisis delays such study.

Overall resume

Investigations in the framework of this thesis have led to many new insights in the mechanisms underlying corneal dissections and two different patented approaches for its improvement. Due to safety considerations, the use of UV-A wavelengths for dissection is clinically not possible although it improves surgical precision. However, focus shaping is possible at UV and IR wavelengths and, therefore, clinically applicable. The improvement of dissection quality has been already demonstrated on a medical device and the final hurdle for clinical implementation is the conduction of a clinical study and licensing of the patent family [12].

References

1. Pallikaris, I.G., et al., *Laser in situ keratomileusis.* Lasers Surg Med, 1990. **10**(5): p. 463-8.
2. Buratto, L., M. Ferrari, and P. Rama, *Excimer laser intrastromal keratomileusis.* Am J Ophthalmol, 1992. **113**(3): p. 291-5.
3. Vogel, A. and V. Venugopalan, *Mechanisms of pulsed laser ablation of biological tissues.* Chemical Reviews, 2003. **103**(2): p. 577-644.
4. Juhasz, T., et al., *Corneal refractive surgery with femtosecond lasers.* IEEE Journal of Selected Topics in Quantum Electronics, 1999. **5**(4): p. 902-910.
5. Schallhorn, S.C., et al., *Wavefront-Guided LASIK for the Correction of Primary Myopia and Astigmatism.* Ophthalmology, 2008. **115**(7): p. 1249-1261.
6. Sekundo, W., K.S. Kunert, and M. Blum, *Small incision corneal refractive surgery using the small incision lenticule extraction (SMILE) procedure for the correction of myopia and myopic astigmatism: results of a 6 month prospective study.* British Journal of Ophthalmology, 2011. **95**(3): p. 335-339.
7. Linz, N., et al., *Wavelength dependence of femtosecond laser-induced breakdown in water and implications for laser surgery.* Physical Review B, 2016. **94**(2): p. 024113.
8. Noack, J. and A. Vogel, *Laser-induced plasma formation in water at nanosecond to femtosecond time scales: Calculation of thresholds, absorption coefficients, and energy density.* Ieee Journal of Quantum Electronics, 1999. **35**(8): p. 1156-1167.
9. Vogel, A., et al., *Mechanisms of femtosecond laser nanosurgery of cells and tissues.* Applied Physics B-Lasers and Optics, 2005. **81**(8): p. 1015-1047.
10. Vogel, A., S. Busch, and U. Parlitz, *Shock wave emission and cavitation bubble generation by picosecond and nanosecond optical breakdown in water.* Journal of the Acoustical Society of America, 1996. **100**(1): p. 148-165.
11. Freidank, S., A. Vogel, and N. Linz, *Mechanisms of corneal intrastromal laser dissection for refractive surgery: ultra-high-speed photographic investigation at up to 50 million frames per second.* Biomedical Optics Express, 2022. **13**(5): p. 3056-3079.
12. Vogel, A., S. Freidank, and N. Linz, *Device for laser cutting within transparent materials: European Patent 2760622 B1, US Patent 9795511 B2, Chinese Patent 104703563 B, Japanese Patent 6005290 B2*. 2015.
13. Freidank, S., A. Vogel, and N. Linz, *Optical Vortex Beam for Gentle and Ultraprecise Intrastromal Corneal Dissection in Refractive Surgery.* Translational Vision Science & Technology, 2020. **9**(10): p. 22.
14. Vogel, A., S. Freidank, and N. Linz, *Method for laser machining transparent materials, US Patent 8,350,183, Publication date 2013/1/8*. 2013.
15. Linz, N., et al., *Laser-induced plasma formation and cavitation in water: from nanoeffects to extreme states of matter.* arXiv:2501.11029 [physics.flu-dyn], 2025: p. 1-84.
16. Coohill, T.P., *Uses and effects of ultraviolet radiation on cells and tissues*, in *Lasers in Medicine*, R.W. Waynant, Editor. 2002, CRC Press: Boca Raton. p. 85-107.
17. Schulmeister, K., et al., *Review of exposure limits and experimental data for corneal and lenticular damage from short pulsed UV and IR laser radiation.* Journal of Laser Applications, 2008. **20**(2): p. 98-105.
18. Munnerlyn, C.R., S.J. Koons, and J. Marshall, *Photorefractive keratectomy: a technique for laser refractive surgery.* J Cataract Refract Surg, 1988. **14**(1): p. 46-52.
19. O'Brart, D.P., et al., *Hyperopic photorefractive keratectomy with the erodible mask and axicon system: two year follow-up.* J Cataract Refract Surg, 2000. **26**(4): p. 524-35.
20. Basicmedicalkey, *Corneal and sclera.* https://basicmedicalkey.com/cornea-and-sclera/, 2016.

21. Meek, K.M., *Corneal collagen—its role in maintaining corneal shape and transparency.* Biophysical Reviews, 2009. **1**(2): p. 83-93.
22. Asiyo-Vogel, M., *Methods for the Analysis of Thermal Denaturation of Corneal Collagen in Refractive Laser Surgery, PhD thesis.* Faculty of Medicine, University of Luebeck, 1998. **PhD**: p. 1-105.
23. Benedek, G.B., *Theory of transparency of the eye.* Appl Opt, 1971. **10**(3): p. 459-73.
24. Kohnen, T., A. Strenger, and O.K. Klaproth, *Basic knowledge of refractive surgery: correction of refractive errors using modern surgical procedures.* Dtsch Arztebl Int, 2008. **105**(9): p. 163-70.
25. Shah, D.N. and S. Melki, *Complications of femtosecond-assisted laser in-situ keratomileusis flaps.* Semin Ophthalmol, 2014. **29**(5-6): p. 363-75.
26. dos Santos, A.M., et al., *Femtosecond Laser-Assisted LASIK Flap Complications.* J Refract Surg, 2016. **32**(1): p. 52-9.
27. Tucker, S.H. and P. Sood, *Flap Complications from Femtosecond Laser-assisted in Situ Keratomileusis.* US Ophthalmic Review, 2019. **12**(1): p. 21-7.
28. Peyman, G.A., *Method for modifying corneal curvature.* US Patent 4,840,175, 1989.
29. Pallikaris, I.G., et al., *A corneal flap technique for laser in situ keratomileusis. Human studies.* Arch Ophthalmol, 1991. **109**(12): p. 1699-702.
30. Vogel, A. and V. Venugopalan, *Mechanisms of pulsed laser ablation of biological tissues.* Chem Rev, 2003. **103**(2): p. 577-644.
31. Lubatschowski, H., et al., *Application of ultrashort laser pulses for intrastromal refractive surgery.* Graefes Arch Clin Exp Ophthalmol, 2000. **238**(1): p. 33-9.
32. Holzer, M.P., et al., *Diffuse lamelläre Keratitis.* Der Ophthalmologe, 2002. **99**(11): p. 849-853.
33. Vaddavalli, P.K., et al., *Corneal Haze Following Disruption of Epithelial Basement Membrane on Ultra-high-resolution OCT Following Femtosecond LASIK.* Journal of Refractive Surgery, 2012. **28**(1): p. 72-74.
34. Blum, M., et al., *Five-year results of Small Incision Lenticule Extraction (ReLEx SMILE).* Br J Ophthalmol, 2016. **100**(9): p. 1192-5.
35. Shtein, R.M., *Post-LASIK dry eye.* Expert Rev Ophthalmol, 2011. **6**(5): p. 575-582.
36. Ziebarth, N.M., et al., *Surface quality of human corneal lenticules after SMILE assessed using environmental scanning electron microscopy.* J Refract Surg, 2014. **30**(6): p. 388-93.
37. Dave, R., et al., *Sixteen-year follow-up of hyperopic laser in situ keratomileusis.* J Cataract Refract Surg, 2016. **42**(5): p. 717-24.
38. Freidank, S., et al., *Correction of hyperopia by intrastromal cutting and liquid filler injection.* J Biomed Opt, 2019. **24**(5): p. 058001.
39. Wertheimer, C.M., et al., *Refractive Changes After Corneal Stromal Filler Injection for the Correction of Hyperopia.* J Refract Surg, 2020. **36**(6): p. 406-413.
40. Vogel, A., et al., *Apparatus for changing the refractive power of the cornea: U.S. Patent 11,076,994*, PCT/US2017/035333, Editor. 2017. p. WO/2017/210374.
41. Lubatschowski, H., *Overview of commercially available femtosecond lasers in refractive surgery.* Journal of Refractive Surgery, 2008. **24**(1): p. 102-107.
42. Song, W.Y., et al., *Wavelength-dependent optical properties of melanosomes in retinal pigmented epithelium and their changes with melanin bleaching: a numerical study.* Biomedical Optics Express, 2017. **8**(9): p. 3966-3980.
43. Sun, H., et al., *Simulation of the temperature increase in human cadaver retina during direct illumination by 150-kHz femtosecond laser pulses.* J Biomed Opt, 2011. **16**(10): p. 108001.
44. Palanker, D.V., et al., *Femtosecond Laser-Assisted Cataract Surgery with Integrated Optical Coherence Tomography.* Science Translational Medicine, 2010. **2**(58): p. 58ra85.

45. Nagy, Z., et al., *Initial Clinical Evaluation of an Intraocular Femtosecond Laser in Cataract Surgery.* Journal of Refractive Surgery, 2009. **25**(12): p. 1053-1060.
46. Donaldson, K.E., et al., *Femtosecond laser-assisted cataract surgery.* J Cataract Refract Surg, 2013. **39**(11): p. 1753-63.
47. Montes-Mico, R., et al., *Visual performance with multifocal intraocular lenses: mesopic contrast sensitivity under distance and near conditions.* Ophthalmology, 2004. **111**(1): p. 85-96.
48. Latz, C., et al., *Femtosecond-Laser Assisted Surgery of the Eye: Overview and Impact of the Low-Energy Concept.* Micromachines, 2021. **12**(2): p. 122.
49. Pajic, B., et al., *Why Use Ultrashort Pulses in Ophthalmology and Which Factors Affect Cut Quality.* Medicina-Lithuania, 2021. **57**(7): p. 700.
50. Kaiser, A., et al., *Microscopic processes in dielectrics under irradiation by subpicosecond laser pulses.* Physical Review B, 2000. **61**(17): p. 11437-11450.
51. Christensen, B.H. and P. Balling, *Modeling ultrashort-pulse laser ablation of dielectric materials.* Physical Review B, 2009. **79**(15).
52. Keldysh, L.V., *Ionization in the Field of a Strong Electromagnetic Wave.* Soviet Physics Jetp-Ussr, 1965. **20**(5): p. 1307-&.
53. Linz, N., et al., *Wavelength dependence of nanosecond infrared laser-induced breakdown in water: Evidence for multiphoton initiation via an intermediate state.* Physical Review B, 2015. **91**(13): p. 134114.
54. Balling, P. and J. Schou, *Femtosecond-laser ablation dynamics of dielectrics: basics and applications for thin films.* Reports on Progress in Physics, 2013. **76**(3).
55. Ammosov, M.V., N.B. Delone, and V.P. Krainov, *Tunnel Ionization of Complex Atoms and Atomic Ions in a Varying Electromagnetic-Field.* Zhurnal Eksperimentalnoi I Teoreticheskoi Fiziki, 1986. **91**(6): p. 2008-2013.
56. Rethfeld, B., *Unified model for the free-electron avalanche in laser-irradiated dielectrics (vol 92, art no 187401, 2004).* Physical Review Letters, 2004. **92**(20).
57. Grojo, D., et al., *Long-wavelength multiphoton ionization inside band-gap solids.* Physical Review B, 2013. **88**(19).
58. Sarpe, C., et al., *Real-time observation of transient electron density in water irradiated with tailored femtosecond laser pulses.* New Journal of Physics, 2012. **14**.
59. Kennedy, P.K., *A First-Order Model for Computation of Laser-Induced Breakdown Thresholds in Ocular and Aqueous-Media .1. Theory.* Ieee Journal of Quantum Electronics, 1995. **31**(12): p. 2241-2249.
60. Liang, X.X., Z.X. Zhang, and A. Vogel, *Multi-rate-equation modeling of the energy spectrum of laser-induced conduction band electrons in water.* Optics Express, 2019. **27**(4): p. 4672-4693.
61. Rethfeld, B., *Free-electron generation in laser-irradiated dielectrics.* Physical Review B, 2006. **73**(3).
62. Elles, C.G., et al., *Excited state dynamics of liquid water: Insight from the dissociation reaction following two-photon excitation.* Journal of Chemical Physics, 2007. **126**(16): p. 164503.
63. Nikogosyan, D.N., A.A. Oraevsky, and V.I. Rupasov, *Two-photon ionization and dissociation of liquid water by powerful laser UV radiation.* Chemical Phyics, 1983. **77**: p. 131-143.
64. Lian, R., et al., *Geminate recombination of electrons generated by above-the-gap (12.4 eV) photoionization of liquid water.* Chemical Physics Letters, 2004. **398**(1-3): p. 102-106.
65. Docchio, F., *Lifetimes of Plasmas Induced in Liquids and Ocular Media by Single Nd-Yag Laser-Pulses of Different Duration.* Europhysics Letters, 1988. **6**(5): p. 407-412.
66. Nikjoo, H. and T. Limsuwan, *Biophysical basis of ionizing radiation*, in *Comprehensive Biomedical Physics* A. Brahme, Editor. 2014, Elsevier.
67. Plante, I., *A review of simulation codes and approaches for radiation chemistry.* Physics in Medicine and Biology, 2021. **66**(3).

68. Woutersen, S. and H.J. Bakker, *Resonant intermolecular transfer of vibrational energy in liquid water.* Nature, 1999. **402**(6761): p. 507-509.
69. Seilmeier, A. and W. Kaiser, *Ultrashort intramolecular and intermolecular vibrational energy transfer of polyatomic molecules in liquids* in *Ultrashort Laser Pulses*, W. Kaiser, Editor. 1993, Springer Verlag.
70. Cowan, M.L., et al., *Ultrafast memory loss and energy redistribution in the hydrogen bond network of liquid H2O.* Nature, 2005. **434**(7030): p. 199-202.
71. Goulet, T. and J.P. Jaygerin, *Thermalization of Subexcitation Electrons in Solid Water.* Radiation Research, 1989. **118**(1): p. 46-62.
72. Kai, T., et al., *Dynamics of low-energy electrons in liquid water with consideration of Coulomb interaction with positively charged water molecules induced by electron collision.* Radiation Physics and Chemistry, 2014. **102**: p. 16-22.
73. Kai, T., et al., *Cross sections, stopping powers, and energy loss rates for rotational and phonon excitation processes in liquid water by electron impact.* Radiation Physics and Chemistry, 2015. **108**: p. 13-17.
74. Kai, T., et al., *Dynamic Behavior of Secondary Electrons in Liquid Water at the Earliest Stage upon Irradiation: Implications for DNA Damage Localization Mechanism.* Journal of Physical Chemistry A, 2016. **120**(42): p. 8228-8233.
75. Minardi, S., et al., *Time-resolved refractive index and absorption mapping of light-plasma filaments in water.* Optics Letters, 2008. **33**(1): p. 86-88.
76. Kai, T., et al., *Thermal equilibrium and prehydration processes of electrons injected into liquid water calculated by dynamic Monte Carlo method.* Radiation Physics and Chemistry, 2015. **115**: p. 1-5.
77. Mattsson, T.R. and M.P. Desjarlais, *Phase diagram and electrical conductivity of high energy-density water from density functional theory.* Physical Review Letters, 2006. **97**(1).
78. Mattsson, T.R. and M.P. Desjarlais, *High energy-density water: Density functional theory calculations of structure and electrical conductivity*, in *Sandia Report: SAND2006-7539, Sandia National Laboratories, USA*. 2007.
79. Schaffer, C.B., et al., *Dynamics of femtosecond laser-induced breakdown in water from femtoseconds to microseconds.* Optics Express, 2002. **10**(3): p. 196-203.
80. Sarpe-Tudoran, C., et al., *Plasma dynamics of water breakdown at a water surface induced by femtosecond laser pulses.* Applied Physics Letters, 2006. **88**(26).
81. Saleh, B.E.A. and M.C. Teich, *Fundamentals of photonics*. 2nd ed. Wiley series in pure and applied optics. 2007, Hoboken, N.J.: Wiley Interscience. xix, 1175 p.
82. Datta, S., *Electronic transport in mesoscopic systems*. Cambridge studies in semiconductor physics and microelectronic engineering. 1995, Cambridge ; New York: Cambridge University Press. xv, 377 p.
83. Zel′dovich, I.A.B., et al., *Physics of shock waves and high-temperature hydrodynamic phenomena*. 1966, New York,: Academic Press.
84. Brenner, M.P., S. Hilgenfeldt, and D. Lohse, *Single-bubble sonoluminescence.* Reviews of Modern Physics, 2002. **74**(2): p. 425-484.
85. Kroll, N. and K.M. Watson, *Theoretical Study of Ionization of Air by Intense Laser Pulses.* Physical Review A, 1972. **5**(4): p. 1883-&.
86. Garcia-Lechuga, M., et al., *Wavelength-Independent Performance of Femtosecond Laser Dielectric Ablation Spanning Over Three Octaves.* Physical Review Applied, 2023. **19**(4).
87. Linz, N., et al., *Roles of tunneling, multiphoton ionization, and cascade ionization for optical breakdown in aqueous media.* Final Report AFOSR International Research Initiative Grant FA 8655-05-1-3010 2010.
88. Close, D.M., *Calculated Vertical Ionization Energies of the Common α-Amino Acids in the Gas Phase and in Solution.* Journal of Physical Chemistry A, 2011. **115**(13): p. 2900-2912.

89. Pluharová, E., P. Slavícek, and P. Jungwirth, *Modeling Photoionization of Aqueous DNA and Its Components.* Accounts of Chemical Research, 2015. **48**(5): p. 1209-1217.
90. Schmalz, M., et al., *Dissection of DNA damage and repair pathways in live cells by femtosecond laser microirradiation and free- electron modeling.* Proceedings of the National Academy of Sciences of the United States of America, 2023. **120**(25).
91. Varghese, B., et al., *Influence of absorption induced thermal initiation pathway on irradiance threshold for laser induced breakdown.* Biomedical Optics Express, 2015. **6**(4): p. 1234-1240.
92. Sacchi, C.A., *Laser-Induced Electric Breakdown in Water.* Journal of the Optical Society of America B-Optical Physics, 1991. **8**(2): p. 337-345.
93. Kovalchuk, T., et al., *Laser breakdown in alcohols and water induced by λ=1064 nm nanosecond pulses.* Chemical Physics Letters, 2010. **500**(4-6): p. 242-250.
94. Lauterborn, W. and T. Kurz, *Physics of bubble oscillations.* Reports on Progress in Physics, 2010. **73**(10).
95. Liang, X.X., et al., *Comprehensive analysis of spherical bubble oscillations and shock wave emission in laser-induced cavitation.* Journal of Fluid Mechanics, 2022.
96. Liang, X.X. and A. Vogel, *Influence of inertial confinement on laser-induced bubble generation and shock wave emission.* arXiv:2501.13749 [physics.flu-dyn], 2025: p. 1-43.
97. Cole, R.H., *Underwater explosions*. 1948, Princeton,: Princeton Univ. Press. ix, 437 p.
98. Löfstedt, R., B.P. Barber, and S.J. Putterman, *Toward a hydrodynamic theory of sonoluminescence.* Physics of Fluids A: Fluid Dynamics, 1993. **5**(11): p. 2911-2928.
99. Rice, M.H. and J.M. Walsh, *Equation of State of Water to 250 Kilobars.* The Journal of Chemical Physics, 1957. **26**(4): p. 824-830.
100. Vogel, A., et al., *Energy balance of optical breakdown in water at nanosecond to femtosecond time scales.* Applied Physics B-Lasers and Optics, 1999. **68**(2): p. 271-280.
101. Brujan, E.A. and A. Vogel, *Stress wave emission and cavitation bubble dynamics by nanosecond optical breakdown in a tissue phantom.* Journal of Fluid Mechanics, 2006. **558**: p. 281-308.
102. Gaudron, R., M.T. Warnez, and E. Johnsen, *Bubble dynamics in a viscoelastic medium with nonlinear elasticity.* Journal of Fluid Mechanics, 2015. **766**: p. 10.1017/jfm.2015.7.
103. Estrada, J.B., et al., *High strain-rate soft material characterization via inertial cavitation.* Journal of the Mechanics and Physics of Solids, 2018. **112**: p. 291-317.
104. Hao, X.A., et al., *Effects of polarization on the de-excitation dark focal spot in STED microscopy.* Journal of Optics, 2010. **12**(11): p. 115707.
105. Yao, A.M. and M.J. Padgett, *Orbital angular momentum: origins, behavior and applications.* Advances in Optics and Photonics, 2011. **3**(2): p. 161-204.
106. Heisterkamp, A., et al., *Nonlinear side effects of fs pulses inside corneal tissue during photodisruption.* Applied Physics B-Lasers and Optics, 2002. **74**(4-5): p. 419-425.
107. Arnold, C.L., et al., *Streak formation as side effect of optical breakdown during processing the bulk of transparent Kerr media with ultra-short laser pulses.* Applied Physics B-Lasers and Optics, 2005. **80**(2): p. 247-253.
108. Loesel, F.H., et al., *Laser-induced optical breakdown on hard and soft tissues and its dependence on the pulse duration: Experiment and model.* Ieee Journal of Quantum Electronics, 1996. **32**(10): p. 1717-1722.
109. Netto, M.V., et al., *Femtosecond laser and microkeratome corneal flaps: Comparison of stromal wound healing and inflammation.* Journal of Refractive Surgery, 2007. **23**(7): p. 667-676.
110. de Medeiros, F.W., et al., *Effect of femtosecond laser energy level on corneal stromal cell death and inflammation.* J Refract Surg, 2009. **25**(10): p. 869-74.
111. Zuberbuhler, B., et al., *Corneal Surgery*. Essential Techniques. 2013: Springer Berlin. 146.

112. Vogel, A., et al., *Intraocular Photodisruption with Picosecond and Nanosecond Laser-Pulses - Tissue Effects in Cornea, Lens, and Retina.* Investigative Ophthalmology & Visual Science, 1994. **35**(7): p. 3032-3044.
113. Juhasz, T., et al., *Time-resolved observations of shock waves and cavitation bubbles generated by femtosecond laser pulses in corneal tissue and water.* Lasers in Surgery and Medicine, 1996. **19**(1): p. 23-31.
114. Reggiani-Mello, G. and R.R. Krueger, *Comparison of commercially available femtosecond lasers in refractive surgery.* Expert Review of Ophthalmology, 2011. **6**(1): p. 55-65.
115. Komai, Y. and T. Ushiki, *The three-dimensional organization of collagen fibrils in the human cornea and sclera.* Invest Ophthalmol Vis Sci, 1991. **32**(8): p. 2244-58.
116. Kennedy, P.K., et al., *A First-Order Model for Computation of Laser-Induced Breakdown Thresholds in Ocular and Aqueous-Media .2. Comparison to Experiment.* Ieee Journal of Quantum Electronics, 1995. **31**(12): p. 2250-2257.
117. Kennedy, P.K., D.X. Hammer, and B.A. Rockwell, *Laser-induced breakdown in aqueous media.* Progress in Quantum Electronics, 1997. **21**(3): p. 155-248.
118. Noack, J., et al., *Influence of pulse duration on mechanical effects after laser-induced breakdown in water.* Journal of Applied Physics, 1998. **83**(12): p. 7488-7495.
119. Vogel, A., et al., *Femtosecond-laser-induced nanocavitation in water: Implications for optical breakdown threshold and cell surgery.* Physical Review Letters, 2008. **100**(3): p. 038102.
120. Tinne, N., et al., *Interaction Mechanisms of Cavitation Bubbles Induced by Spatially and Temporally Separated fs-Laser Pulses.* PLOS ONE, 2014. **9**(12): p. e114437.
121. Nadine, T., et al., *Effects of cavitation bubble interaction with temporally separated fs-laser pulses.* Journal of Biomedical Optics, 2014. **19**(4): p. 1 -- 12.
122. Agrež, V., T. Požar, and R. Petkovšek, *High-speed photography of shock waves with an adaptive illumination.* Optics Letters, 2020. **45**(6).
123. Mur, J., et al., *Microbubble dynamics and jetting near tissue-phantom biointerfaces.* Biomedical Optics Express, 2022. **13**(2).
124. Graziadei, G.A.M. and P.P.C. Graziadei, *Neurogenesis and Neuron Regeneration in the Olfactory System of Mammals .2. Degeneration and Reconstitution of the Olfactory Sensory Neurons after Axotomy.* Journal of Neurocytology, 1979. **8**(2): p. 197-213.
125. Zimmermann, D.R., et al., *Type VI collagen is a major component of the human cornea.* FEBS Lett, 1986. **197**(1-2): p. 55-8.
126. Meek, K.M. and C. Boote, *The use of X-ray scattering techniques to quantify the orientation and distribution of collagen in the corneal stroma.* Prog Retin Eye Res, 2009. **28**(5): p. 369-92.
127. Meek, K.M., *Corneal collagen-its role in maintaining corneal shape and transparency.* Biophys Rev, 2009. **1**(2): p. 83-93.
128. Daxer, A., et al., *Collagen fibrils in the human corneal stroma: structure and aging.* Invest Ophthalmol Vis Sci, 1998. **39**(3): p. 644-8.
129. Meek, K.M. and C. Boote, *The organization of collagen in the corneal stroma.* Exp Eye Res, 2004. **78**(3): p. 503-12.
130. Meek, K.M., et al., *The organisation of collagen fibrils in the human corneal stroma: a synchrotron X-ray diffraction study.* Curr Eye Res, 1987. **6**(7): p. 841-6.
131. Morishige, N., et al., *Noninvasive corneal stromal collagen imaging using two-photon-generated second-harmonic signals.* J Cataract Refract Surg, 2006. **32**(11): p. 1784-91.
132. Jester, J.V., et al., *Evaluating corneal collagen organization using high-resolution nonlinear optical macroscopy.* Eye Contact Lens, 2010. **36**(5): p. 260-4.
133. Winkler, M., et al., *High resolution macroscopy (HRMac) of the eye using nonlinear optical imaging*. SPIE LASE. Vol. 7589. 2010: SPIE.

134. Winkler, M., et al., *Nonlinear Optical Macroscopic Assessment of 3-D Corneal Collagen Organization and Axial Biomechanics.* Investigative Ophthalmology & Visual Science, 2011. **52**(12): p. 8818-8827.

135. Bergmanson, J.P., et al., *Assessment of the number of lamellae in the central region of the normal human corneal stroma at the resolution of the transmission electron microscope.* Eye Contact Lens, 2005. **31**(6): p. 281-7.

136. Hammond, G.M., et al., *The microanatomy of Bowman`s layer in the cornea of the pig: Changes in collagen fibril architecture at the corneoscleral limbus.* Eur. J. Anat., 2020. **24**: p. 399-406.

137. Boettner, E.A. and J.R. Wolter, *Transmission of the Ocular Media.* Investigative Ophthalmology, 1962. **1**(6): p. 776-783.

138. Ambach, W., et al., *Spectral Transmission of the Optical Media of the Human Eye with Respect to Keratitis and Cataract Formation.* Documenta Ophthalmologica, 1994. **88**(2): p. 165-173.

139. Lord Rayleigh, O.M., *On the pressure developed in a liquid during the collapse of a spherical cavity.* The London, Edinburgh, and Dublin Philosophical Magazine and Journal of Science. **34**(200): p. 94-98.

140. Werner, L. and O. Claus-Dieter, *Cavitation bubble dynamics.* Ultrasonics Sonochemistry, 1997. **4**(2): p. 65-75.

141. Docchio, F., C. Sacchi, and J. Marshall, *Experimental Investigation of Optical Breakdown Thresholds in Ocular Media under Single Pulse Irradiation with Different Pulse Durations.* Lasers in Ophthalmology, 1986. **1**(2): p. 82-93.

142. Maatz, G., et al., *Chemical and physical side effects at application of ultrashort laser pulses for intrastromal refractive surgery.* Journal of Optics a-Pure and Applied Optics, 2000. **2**(1): p. 59-64.

143. Leymarie, N., C.E. Costello, and P.B. O'Connor, *Electron capture dissociation initiates a free radical reaction cascade.* Journal of the American Chemical Society, 2003. **125**(29): p. 8949-8958.

144. Alizadeh, E., et al., *Low-energy electron-induced dissociation in condensed-phase L-cysteine I: Desorption of anions from chemisorbed films.* Journal of Physics: Conference Series, 2015. **635**(1): p. 012001.

145. Murphy, D.B. and M.W. Davidson, *Fundamentals of Light Microscopy and Electronic Imaging, 2nd Edition*. 2012: Wiley-Blackwell. 560.

146. Binder, P.S., et al., *Characterization of submicrojoule femtosecond laser corneal tissue dissection.* J Cataract Refract Surg, 2008. **34**(1): p. 146-52.

147. Knox Cartwright, N.E., J.R. Tyrer, and J. Marshall, *Age-Related Differences in the Elasticity of the Human Cornea.* Investigative Ophthalmology & Visual Science, 2011. **52**(7): p. 4324-4329.

148. Shih, P.-J., et al., *Estimation of the Corneal Young's Modulus In Vivo Based on a Fluid-Filled Spherical-Shell Model with Scheimpflug Imaging.* Journal of Ophthalmology, 2017. **2017**: p. 5410143.

149. Qin, X., et al., *Evaluation of corneal elastic modulus based on Corneal Visualization Scheimpflug Technology.* BioMedical Engineering OnLine, 2019. **18**(1): p. 42.

150. Haut, R.C., *The effects of orientation and location on the strength of dorsal rat skin in high and low speed tensile failure experiments.* J Biomech Eng, 1989. **111**(2): p. 136-40.

151. Salomão, M.Q. and S.E. Wilson, *Femtosecond laser in laser in situ keratomileusis.* Journal of Cataract & Refractive Surgery, 2010. **36**(6).

152. Griffith, A.A. and G.I. Taylor, *VI. The phenomena of rupture and flow in solids.* Philosophical Transactions of the Royal Society of London. Series A, Containing Papers of a Mathematical or Physical Character, 1921. **221**(582-593): p. 163-198.

153. Gordon, J.E., *The Science of Structures and Materials*. Scientific American Library Series. 1988, New York: Freeman. 217.

154. Orowan, E., *Fracture and strength of solids.* Reports on Progress in Physics, 1949. **12**(1): p. 185-232.
155. Irwin, G.R., *Fracture Dynamics, Fracturing of Metals. American Society for Metals, Cleveland.* 1948: p. 147-166.
156. Eshelby, J.D., *Fracture mechanics.* Science Progress (1933-), 1971. **59**(234): p. 161-179.
157. Hull, D., *Micromechanisms of fracture in metals and polymers.* Science Progress (1933-), 1969. **57**(228): p. 495-512.
158. Eshelby, J.D., *The elastic field of a crack extending non-uniformly under general anti-plane loading.* Journal of the Mechanics and Physics of Solids, 1969. **17**(3): p. 177-199.
159. Barenblatt, G.I., *The Mathematical Theory of Equilibrium Cracks in Brittle Fracture*, in *Advances in Applied Mechanics*, H.L. Dryden, et al., Editors. 1962, Elsevier. p. 55-129.
160. Cook, J., et al., *Mechanism for Control of Crack Propagation in All-Brittle Systems.* Proceedings of the Royal Society of London Series a-Mathematical and Physical Sciences, 1964. **282**(1390): p. 508-+.
161. HOLO|OR, *Optical Vortex Phase Plate, Product Catalogue,* https://www.holoor.co.il/application/optical-vortex-phase-plate-application-notes/ 2020.
162. Linz, N., et al., *Experimental and theoretical investigations of the mechanisms of free-electron-mediated modification of biomolecules in nonlinear microscopy. AFOSR Research Interest Biophysics, BAA-AFOSR-2014-0001, Grant FA 9550-15-1-0326, Final Report*. 2018. p. 165.
163. Chinga, G., et al., *Quantification of the 3D microstructure of SC surfaces.* J Microsc, 2007. **227**(Pt 3): p. 254-65.
164. Sarayba, M.A., et al., *Comparative study of stromal bed quality by using mechanical, IntraLase femtosecond laser 15- and 30-kHz microkeratomes.* Cornea, 2007. **26**(4): p. 446-51.
165. Sander, M., et al., *Monitoring the cutting process of the laser-induced optical breakdown (LIOB) during femtosecond-laser in-situ keratomileusis (fs-LASIK).* Medical Laser Application, 2009. **24**(3): p. 158 - 164.
166. Wilhelm, F.W., et al., *Cut edges and surface characteristics produced by different microkeratomes.* J Refract Surg, 2000. **16**(6): p. 690-700.
167. Kunert, K.S., et al., *Surface quality of human corneal lenticules after femtosecond laser surgery for myopia comparing different laser parameters.* Graefes Arch Clin Exp Ophthalmol, 2011. **249**(9): p. 1417-24.
168. Smolek, M.K. and B.E. McCarey, *Interlamellar adhesive strength in human eyebank corneas.* Invest Ophthalmol Vis Sci, 1990. **31**(6): p. 1087-95.
169. Wagner, W. and A. Pruss, *The IAPWS formulation 1995 for the thermodynamic properties of ordinary water substance for general and scientific use.* Journal of Physical and Chemical Reference Data, 2002. **31**(2): p. 387-535.
170. Paltauf, G. and H. Schmidt-Kloiber, *Photoacoustic cavitation in spherical and cylindrical absorbers.* Applied Physics a-Materials Science & Processing, 1999. **68**(5): p. 525-531.
171. Doukas, A.G., D.J. McAuliffe, and T.J. Flotte, *Biological effects of laser-induced shock waves: structural and functional cell damage in vitro.* Ultrasound Med Biol, 1993. **19**(2): p. 137-46.
172. Doukas, A.G. and T.J. Flotte, *Physical characteristics and biological effects of laser-induced stress waves.* Ultrasound in Medicine and Biology, 1996. **22**(2): p. 151-164.
173. Esenaliev, R.O., et al., *Effect on erythrocytes of acoustic waves generated upon absorption of laser radiation.* Lasers in the Life Sciences, 1994. **6**(3): p. 153-161.
174. Duck, F.A., *Physical Properties of Tissue*. 1990: Academic Press: London.
175. Vogel, A., M. Asiyo-Vogel, and R. Birngruber, *Investigations on Intrastromal Refractive Surgery with Picosecond Nd-Yag Laser-Pulses.* Investigative Ophthalmology & Visual Science, 1994. **35**(4): p. 2155-2155.

176. Mohan, R.R., et al., *Apoptosis, necrosis, proliferation, and myofibroblast generation in the stroma following LASIK and PRK.* Experimental Eye Research, 2003. **76**(1): p. 71-87.

177. Lim, J.J. and M.H. Shamos, *Evaluation of kinetic parameters of thermal decomposition of native collagen by thermogravimetric analysis.* Biopolymers, 1974. **13**(9): p. 1791-807.

178. McKenzie, A.L., *A three-zone model of soft-tissue damage by a CO2 laser.* Phys Med Biol, 1986. **31**(9): p. 967-83.

179. Vogel, A. and V. Venugopalan, *Pulsed laser ablation of tissue, pages 551-614 in "Optical-Thermal Response of Laser-Irradiated Tissue", 2nd Edition, AJ Welch and M van Gemert* 2011: Springer, Heidelberg, New York.

180. Liu, C.H., et al., *Opaque bubble layer: incidence, risk factors, and clinical relevance.* J Cataract Refract Surg, 2014. **40**(3): p. 435-40.

181. Harissi-Dagher, M., A. Todani, and S.A. Melki, *Laser in situ keratomileusis buttonhole: classification and management algorithm.* J Cataract Refract Surg, 2008. **34**(11): p. 1892-9.

182. Mastropasqua, L., et al., *Opaque bubble layer incidence in Femtosecond laser-assisted LASIK: comparison among different flap design parameters.* Int Ophthalmol, 2017. **37**(3): p. 635-641.

183. Son, G., et al., *Possible Risk Factors and Clinical Effects of Opaque Bubble Layer in Small Incision Lenticule Extraction (SMILE).* J Refract Surg, 2017. **33**(1): p. 24-29.

184. Li, L., et al., *Risk Factors for Opaque Bubble Layer in Small Incision Lenticule Extraction (SMILE).* J Refract Surg, 2017. **33**(11): p. 759-764.

185. Vogel, A., et al., *Factors determining the refractive effects of intrastromal photorefractive keratectomy with the picosecond laser.* Journal of Cataract and Refractive Surgery, 1997. **23**(9): p. 1301-1310.

186. Trost, A., et al., *A new nanosecond UV laser at 355 nm: early results of corneal flap cutting in a rabbit model.* Invest Ophthalmol Vis Sci, 2013. **54**(13): p. 7854-64.

187. Linz, N., et al., *From nanoeffects to extreme states of matter - energy dependence of plasma formation in transparent dielectrics for a large range of pulse durations and wavelengths.* Physical Review Research, 2022.

188. Arnold, C.L., et al., *Computational model for nonlinear plasma formation in high NA micromachining of transparent materials and biological cells.* Optics Express, 2007. **15**(16): p. 10303-10317.

189. Bulgakova, N.M., et al., *Modification of transparent materials with ultrashort laser pulses: What is energetically and mechanically meaningful?* Journal of Applied Physics, 2015. **118**(23): p. 233108, 10.1063/1.4937896.

190. Jukna, V., et al., *Underwater acoustic wave generation by filamentation of terawatt ultrashort laser pulses.* Physical Review E, 2016. **93**(6): p. 063106, 10.1103/PhysRevE.93.063106.

191. Fedorov, V.Y., et al., *Accessing Extreme Spatiotemporal Localization of High-Power Laser Radiation through Transformation Optics and Scalar Wave Equations.* Physical Review Letters, 2016. **117**(4): p. 043902, 10.1103/PhysRevLett.117.043902.

192. Couairon, A. and A. Mysyrowicz, *Femtosecond filamentation in transparent media.* Physics Reports, 2007. **441**(2-4): p. 47-189.

193. Orzekowsky-Schroeder, R., et al., *Probing the immune and healing response of murine intestinal mucosa by time-lapse 2-photon microscopy of laser-induced lesions with real-time dosimetry.* Biomedical Optics Express, 2014. **5**(10): p. 3521-3540.

194. Genc, S.L., H. Ma, and V. Venugopalan, *Low-density plasma formation in aqueous biological media using sub-nanosecond laser pulses.* Applied Physics Letters, 2014. **105**(6).

195. Paltauf, G. and P.E. Dyer, *Photomechanical processes and effects in ablation.* Chemical Reviews, 2003. **103**(2): p. 487-518.

196. Boudaïffa, B., et al., *Resonant Formation of DNA Strand Breaks by Low-Energy (3 to 20 eV) Electrons.* Science, 2000. **287**(5458): p. 1658-1660.

197. Zubarev, R.A., et al., *Electron Capture Dissociation for Structural Characterization of Multiply Charged Protein Cations.* Analytical Chemistry, 2000. **72**(3): p. 563-573.

198. Zhurov, K.O., et al., *Principles of electron capture and transfer dissociation mass spectrometry applied to peptide and protein structure analysis.* Chemical Society Reviews, 2013. **42**(12): p. 5014-5030.

199. Linz, N., et al., *Laser Micro- and Nanostructuring for Refractive Eye Surgery*, in *Ultrafast Laser Nanostructuring*. 2023. p. 1217-1245.

200. Smith, R.J. and S.F. Cleary, *Investigation of structural bonding forces in bacteriophage T2.* The Journal of the Acoustical Society of America, 1974. **56**(6): p. 1883-1889.

201. Cleary, S.F., *Laser Pulses and the Generation of Acoustic Transients in Biological Material*, in *Laser Applications in Medicine and Biology*, M.L. Wolbarsht, Editor. 1977, Springer. p. 175-219.

202. Burkhartsmeyer, J. and K.S. Wong, *Molecular Dynamics Simulations of Shockwave Affected STMV Virus to Measure the Frequencies of the Oscillatory Response.* Acoustics, 2022. **4**(1): p. 268-275.

203. Kitai, M.S., et al., *The physics of UV laser cornea ablation.* IEEE Journal of Quantum Electronics, 1991. **27**(2): p. 302-307.

204. Lokhandwalla, M. and B. Sturtevant, *Mechanical haemolysis in shock wave lithotripsy (SWL): I. Analysis of cell deformation due to SWL flow-fields.* Physics in Medicine and Biology, 2001. **46**(2): p. 413-437.

205. van de Kraats, J. and D. van Norren, *Optical density of the aging human ocular media in the visible and the UV.* J Opt Soc Am A Opt Image Sci Vis, 2007. **24**(7): p. 1842-57.

206. Lerman, S., *An Experimental and Clinical-Evaluation of Lens Transparency and Aging.* Journals of Gerontology, 1983. **38**(3): p. 293-301.

207. Maher, E.F., *Transmission and absorption coefficients for ocular media of the rhesus monkey*. 1978, Brooks AFB, Texas: USAF School of Aerospace Medicine. p. 1-90.

208. van Norren, D. and T.G.M.F. Gorgels, *The Action Spectrum of Photochemical Damage to the Retina: A Review of Monochromatic Threshold Data.* Photochemistry and Photobiology, 2011. **87**(4): p. 747-753.

209. Hammer, C.M., et al., *Corneal tissue interactions of a new 345 nm ultraviolet femtosecond laser.* Journal of Cataract and Refractive Surgery, 2015. **41**(6): p. 1279-1288.

210. Menzel-Severing, J., et al., *Evaluation of a 345 nm Femtosecond Laser for Corneal Surgery with Respect to Intraocular Radiation Hazard.* Plos One, 2015. **10**(9): p. e0137638.

211. Belanger, P.A. and M. Rioux, *Ring Pattern of a Lens-Axicon Doublet Illuminated by a Gaussian-Beam.* Applied Optics, 1978. **17**(7): p. 1080-1086.

212. Umhofer, U., E. Jäger, and C. Bischoff, *Refractive and diffractive laser beam shaping optics*, in *Laser Journal, 2011 WILEY-VCH Verlag GmbH & Co. KGaA, Weinheim*. 2011.

List of abbreviations

AI	Avalanche ionization
ArF	Argon-fluoride
BPL	Bright plasma luminescence
CB	Conduction band
CCD	Charge-coupled device
CMOS	Complementary metal oxide semiconductor
DNA	Desoxyribonucleic acid
dpt	Diopter
EOS	Equation of state
FLACS	Femtosecond-Laser-Assisted cataract surgery
fs	Femtosecond
FWHM	Full width at half maximum
H&E	Hematoxylin and Eosin
IBA	Inverse Bremsstrahlung absorption
IOL	Intraocular lens
IR	Infrared
LASER	Light amplification by stimulated emission of radiation
LASIK	Laser-Assisted In Situ Keratomileusis
LED	Light-emitting diode
LG	Laguerre-Gaussian
MOPA	Master oscillator power amplifier
MPE	Maximum permissible exposure
MPI	Multi-photon ionization
NA	Numerical aperture
Nd:YAG	Neodymium-doped Yttrium Aluminum Garnet ($Nd:Y_3Al_5O_{12}$)
OCT	Optical coherence tomography
PAA	Polyacrylamide
PRF	Pulse repetition frequency
PSF	Point spread function
SEM	Scanning electron microscopy
SI	Strong-field ionization
SmILE	Small-incision lenticule extraction
UV	Ultraviolet
VB	Valence band
VIS	Visible

Publications

Linz N, **Freidank S**, Liang XX, Vogel A (2025) Laser-induced plasma formation and cavitation in water: from nanoeffects to extreme states of matter. *arXiv preprint* arXiv:2501.11029

Linz N, **Freidank S,** Liang XX, Vogel A (2023) Laser Micro-and Nanostructuring for Refractive Eye Surgery. In: Stoian R, Bonse J (Eds.): *Ultrafast Laser Nanostructuring*, Springer Series in Optical Sciences Vol 239, pp. 1217–1245, https://doi.org/10.1007/978-3-031-14752-4_33

Freidank S, Vogel A, Linz N (2022) Mechanisms of corneal intrastromal laser dissection for refractive surgery: ultra-high-speed photographic investigation at up to 50 million frames per second. *Biomed. Opt. Expr.* **13**(5):3056-3079

Liang XX, Linz N, **Freidank S**, Paltauf G, Vogel A (2022) Comprehensive analysis of spherical bubble oscillations and shock wave emission in laser-induced cavitation. *J. Fluid Mech.*, **940**:A-5, 1-56

Freidank S, Vogel A, Linz N (2020) Optical Vortex beam for gentle and ultraprecise intrastromal corneal dissection in refractive surgery. *Trans. Vis. Sci. Tech.* **9**(10):22, 1-16

Holzhey A, Sonntag S, Rendenbach J, Ernesti JS, Kakkassery V, Grisanti S, Reinholz F, **Freidank S,** Vogel A, Ranjbar M (2020) Development of a Noninvasive, Laser-Assisted Experimental Model of Corneal Endothelial Cell Loss. *J. Vis. Exp.* (158), e60542, doi:10.3791/60542

Freidank S, Vogel A, Anderson R, Birngruber R, Linz N (2019) Correction of hyperopia by intrastromal cutting and liquid filler injection. *J Biomed. Opt*. **24**: 058001, 1-7

Linz N, **Freidank S,** Liang XX, and Vogel A (2016) Wavelength dependence of femtosecond laser-induced breakdown in water, and implications for laser surgery. *Phys. Rev. B* **94:024113**, 1-19

Linz N, **Freidank S,** Liang X.-X., Vogelmann H, Trickl T, and Vogel A (2015) Wavelength dependence of nanosecond IR laser-induced breakdown in water: Evidence for multiphoton initiation via an intermediate state. *Phys. Rev. B* **91:**134114, 1-10

Orzekowsky-Schroeder R, Klinger A, **Freidank S,** Linz N, Schüth A, Eckert S, ,Hüttmann G, Gebert A, Vogel A (2014) Probing the immune and healing response of murine intestinal mucosa by time-lapse 2-photon microscopy of laser-induced lesions with real-time dosimetry. *Biomed Opt Expr* **5**:3521-3540

Vogel A, **Freidank S,** Linz N (2014) Alternativen zur Femtosekundentechnologie: UV Subnanosekundenpulse und Ringfoki für LASIK Flaperzeugung. *Ophthalmologe* **111**:531–538

Trost A, Schrödl F, Strohmaier C, Bogner B, Runge C, Kaser-Eichberger A, Vogel A, Linz N, **Freidank S,** Hilpert A, Zimmermann I, Grabner G, Reitsamer HA (2013) A new nanosecond UV-laser at 355 nm: early results of corneal flap cutting in a rabbit model, *Invest Ophthalmol Vis Sci* **54**:7854-7864

Vogel A, Linz N, **Freidank S,** Paltauf G (2008) Femtosecond laser induced nanocavitation in water: implications for optical breakdown threshold and cell surgery. *Phys Rev Lett.* **100**: 038102, 1-4

Vogel A, Apitz I, **Freidank S,** Dijkink R (2006) Sensitive high-resolution white-light Schlieren technique with a large dynamic range for the investigation of ablation dynamics. *Opt Lett* **31**:1812-1814

Patents

Vogel A, Linz N, **Freidank S**, Verfahren zur Laserbearbeitung transparenter Materialien. DE 10 2007 028 042.6. B3 granted 07.08.2008; EP 2 152 462 B1 granted 24.05.2017.

Vogel A, Linz N, **Freidank S** Method for laser machining transparent materials. US 2010/0163540 A1, granted 08.01.2013.

Vogel A, **Freidank S**, Linz N Vorrichtung zum Laserschneiden innerhalb transparenter Materialien. EP 2 760 622 B1, granted 19.08.2015.

Vogel A, Linz N, **Freidank S**, Device for laser cutting within transparent materials. JP 6005290 B2, granted 12.10.2016; US 9,795,511 B2, granted 24.10.2017; CN 104703563 A, granted 23.01.2018.

Vogel A, Linz N, **Freidank S**, Birngruber R (08/2021) Apparatus for changing the refractive power of the cornea. US 11,076,994 B2, granted 03.08. 2021.

Awards

2012 Nomination for *Berthold Leibinger Innovationspreis* with project group „UV Nanolaser“ consisting of Alfred Vogel, Norbert Linz, Sebastian Freidank, and Rolf Schwind.

2016 *Thomas-Fredenhagen-Preis* 2016 der Universität zu Lübeck und der Kaufmannschaft zu Lübeck für besondere wissenschaftliche Leistungen und Aktivitäten im Bereich des Technologietransfers und der Patente- und Schutzrechtsentwicklung, together with Prof. Alfred Vogel and Dr. Norbert Linz.